Vibration Modeling and Analysis of a Single Conductor With Stockbridge Dampers

by

Oumar Rafiou Barry

A thesis submitted in conformity with the requirements
for the degree of Doctor of Philosophy
Graduate Department of Mechanical and Industrial Engineering
University of Toronto

Abstract

Vibration Modeling and Analysis of a Single Conductor With Stockbridge Dampers

Oumar Rafiou Barry
Doctor of Philosophy
Graduate Department of Mechanical and Industrial Engineering
University of Toronto
2014

The vibration of a single conductor with Stockbridge dampers is examined theoretically and experimentally. Two novel analytical models are presented. In the first model, the conductor is modeled as a beam subjected to an axial load and the Stockbridge damper is reduced to an equivalent discrete mass-spring-mass and viscous damping coefficient. The second model is based on a double-beam concept. The main beam with an axial load is a representation of the conductor and the Stockbridge damper is modeled as an in-span beam with rigid mass at each end. Using Hamilton's principle, the governing equation of motion and boundary conditions are derived. Expressions are presented for the frequency equations, mode shapes, and orthogonality conditions.

Experiments are conducted to determine the equivalent damping coefficient of the Stockbridge damper, the self-damping coefficient of the conductor, the natural frequencies and response of the conductor with and without a Stockbridge damper. The experimental data are used to validate the proposed models.

With respect to the dynamics of the conductor, the results of both analytical models are found to be in a good agreement with those of the experiments. The first model is simpler and easier to implement with little computation, but gives a very poor prediction of the dynamics of the Stockbridge damper. The second model is more complicated, but gives a good prediction of the dynamics of both conductor and Stockbridge damper. Numerical examples of the free vibration analysis show a significant dependency of the natural frequencies on the mass of the counterweights, length of the rigid link, length of the messenger, and flexural rigidity. The first mode is dominated by the conductor characteristics. The roles of the location of the Stockbridge damper on the system natural frequencies are inconclusive.

The forced vibration results indicate that the response of a bare conductor decreases monotonically with increasing vibration frequency. However, for a loaded conductor, the response can increase or decrease with increasing frequency depending on the location of the damper. Optimization is performed to determine the optimal damping arrangement. The results show that asymmetric damping arrangement and the orientation of the heavier counterweight of the Stockbridge damper toward the span ends result in a better damping performance. These findings can be very useful for transmission lines design engineers and structural engineers.

Dedication

To my daugther, Kadija Mandela Barry and son, Kareem Mohamed-Billo Barry. May God bless you and lead you to the right path!

"Education is the most powerful weapon which you can use to change the world." Nelson Mandela

"Leisure is time for doing something useful. This leisure the diligent man will obtain, but the lazy never." Benjamin Franklin

"As far as the laws of Mathematics refer to reality, they are not certain, as far as they are certain, they don't refer to reality." Albert Einstein

Acknowledgements

First of all, I would like to thank GOD for the blessings and gifts he has bestowed upon me. After all, it is because of his love and guidance that I made it so far in my life.

I am deeply grateful to my advisors, Professor Zu and Professor Oguamanam, for their guidance, unwavering support, constant encouragement, and insight throughout my work.

I would like to offer my sincere thanks to the members of my Ph.D. committee, Professor Cleghorn and Professor Behdinan.

I am extremely thankful to Hydro One, especially, Mr. Andy Mand, Dr. Hathout, and Mr. Ng (CK) for their guidance in choosing this thesis topic.

I would also like to extend my sincere thanks to Messrs. Andrew Rizzetto and Dmitry Ladin of Kinectrics Inc., Toronto, for their assistance with the experiments.

My special thanks goes to my parents, Amadou and Kadiatou Bah, for their love and support throughout my studies. Their encouragement convinced and motivated me to pursue graduate studies.

Special gratitude goes to my love, Ry Long, my daughter Kadija, and my son Kareem. Your love and support motivate me to push my limits.

I thank my four sibblings, Aissatou, Ramatoulaye, Thierno Oury, and Thierno Hamidou for their moral support and encouragement.

My special thanks goes to all my colleagues from the VDML lab, my colleagues from Hydro One, and to all my friends.

Contents

List of Tables

List of Figures

Nomenclature

c_{d}	Equivalent viscous damping coefficient of the Stockbridge damper (Ns/m)
C	Linear regression coefficient
D	Conductor diameter (m)
E_{d}	Dissipation energy of the Stockbridge damper (J)
E_{diss}	Dissipation energy of the cable (J)
$E_{\mathrm{k,max}}$	Maximum kinetic energy of the conductor (J)
E_{c}	Young's modulus of the cable (Pa)
E_{m}	Young's modulus of the messenger (Pa)
$E_{\mathrm{c}}I_{\mathrm{c}}$	Flexural rigidity of the conductor (Nm^2)
$E_{\mathrm{m}}I_{\mathrm{m}}$	Flexural rigidity of the messenger (Nm^2)
f	Vibration frequency (Hz)
f_{s}	Strouhal frequency (Hz)
f_{i} or f_{n}	Natural frequency (Hz) for mode i or n
$F(t)$ or F	Excitation force (N)
F_0	Excitation force amplitude (N)
h	Length of the clamp plate (m)
I_{c}	Second moment of area of the conductor (m^4)
I_{m}	Second moment of area of the messenger (m^4)
I_1	Right-end counterweight rotational inertia or mass moment of inertia (kgm^2)
I_2	Left-end counterweight rotational inertia or mass moment of inertia (kgm^2)
L_{c} or L	Span length of the cable (m)
L_{c1} or L_1, L_{c2} or L_2	Location of damper 1 and 2, respectively (m)
l_1 or $L_{\mathrm{m_1}}$	Right-side messenger length (m)
l_2 or $L_{\mathrm{m_2}}$	Left-side messenger length (m)
m_{c} or m	Conductor mass per unit length (kg/m)
m_{m}	Messenger mass per unit length (kg/m)
$m_{\mathrm{m_1}}$	Right-end messenger mass per unit length (kg/m)
$m_{\mathrm{m_2}}$	Left-end messenger mass per unit length (kg/m)
m_1	Right-end counterweight mass (kg)
m_2	Left-end counterweight mass (kg)
n	Mode number
P_{d}	Power dissipated by the damper (W)
q	Generalized coordinate displacement

$\mathbf{r}_{\mathrm{c}}$	Position vector of conductor (m)
$\mathbf{r}_{\mathrm{c}}^{*}$	Position vector of damper clamp (m)
$\mathbf{r}_{\mathrm{m}_1}$	Position vector of right-end counterweight (m)
$\mathbf{r}_{\mathrm{m}_2}$	Position vector of left-end counterweight (m)
$\mathbf{r}_{\mathrm{mm}_1}$	Position vector of right-end messenger (m)
$\mathbf{r}_{\mathrm{mm}_2}$	Position vector of left-end messenger (m)
s	Strouhal number
T	Cable tension (N)
t	Time (s)
$\mathcal{T}$	Conductor kinetic energy (J)
$\mathcal{V}$	Conductor potential energy (J)
V_{c}	Measured velocity at the clamp of the Stockbridge damper (m/s)
v	wind speed (m/s)
$w_{\mathrm{ci}}(x,t)$	Conductor transverse deformation (m)
$w_{\mathrm{mi}}(x,t)$	Stockbridge damper damper transverse deformation (m)
y_{f}	Experimental vibration displacement of the conductor at the location of the shaker (m)
y_0	Experimental vibration displacement of the conductor at an antinode (m)
Y_{ci}	Conductor mode shapes
Y_{mi}	Stockbridge damper mode shapes
α, β, γ	Linear regression parameters
δ	Variational
ζ	Conductor self-damping ratio
θ_{d}	Phase angle between response and excitation force (rad)
λ	Loop length (m)
ϕ_{FV}	Measured phase angle between the force and the velocity (rad)
ω_n	Natural frequency (rad/s)
ω	Forcing frequency (rad/s)

Chapter 1

Background

1.1 Introduction

Overhead transmission lines are continuously exposed to wind forces which make them prone to the development of repetitive cyclic motions that are sources of tremendous damage to power networks. These motions are known as "wind-induced conductor motion" and they take the form of *conductor galloping*, *wake-induced oscillations*, and *aeolian vibration*. These motions are mainly distinguished by their frequencies and amplitudes of vibration.

Conductor galloping is very low frequency and high amplitude vibration. It is common to both single and bundle conductors and it is caused by the steady crosswinds acting upon an asymmetrically iced conductor surface. The thickness of ice that can cause galloping can be smaller than 2 mm. The frequency of vibration varies from 0.08 to 3 Hz and the amplitude can exceed the conductor sag for the span involved (5 to 300 times the conductor diameter) [1]. Conductor galloping can lead to the worst damage in a very short period of time (1 to 48 hours). Galloping cannot break conductor hardware, but it can damage insulators, dampers, suspension hardware, poles, and towers.

Wake-induced oscillation, also caused by a steady wind, is medium amplitude and medium frequency vibration. The vibration amplitude varies from 0.5 to 80 times the conductor diameter and the frequency varies from 0.15 to 10 Hz [1]. This type of conductor motion only pertains to bundle conductors. Unlike conductor galloping, *wake-induced oscillation* can occur at anytime of the year and can damage the conductor strands. It can also damage suspension hardware, spacer dampers, and dampers. These damages can take place within one month to eight years after installation.

The present study focuses on the third type of wind-induced conductor motion, *aeolian vibration*. The word aeolian is borrowed from an ancient Greek legendary figure, Aeolus, which means god of wind. This type of vibration arises from alternating forces caused by vortex shedding. Vortex shedding is associated with the flow of air across a bluff body. *Aeolian vibration* is specific to single conductor and it is characterized by low amplitudes and high frequencies vibration. The work in this thesis is an extension of my master's work [2]. As such part of the content in this chapter is reproduced from [2].

The frequency of *aeolian vibration* ranges from 3 to 150 Hz and the wind speed ranges from 1 to 7 m/s [1, 3]. The amplitude of vibration is usually less than the diameter of the conductor. The conductor diameter ranges from 6 to 50 mm.

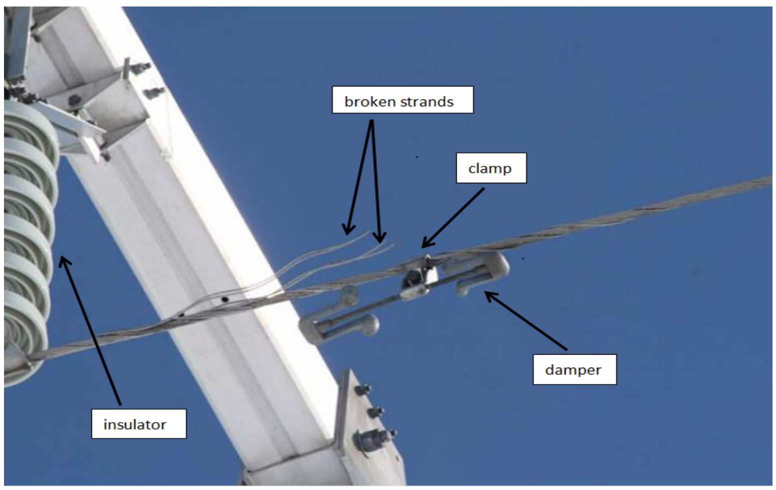

Figure 1.1: Breakage of conductor on Hydro Quebec transmission lines [4].

Field observations indicated that the type of terrain is one of the many factors that contribute to *aeolian vibration*. *Aeolian vibration* is more prone to open fields and bodies of water (such as rivers, lakes, etc.) and usually it occurs in late evenings or early mornings. When *aeolian vibration* of transmission lines is not properly controlled, it can result in serious accidents causing injuries and death, and/or considerable economic loss. Alternating bending stresses and tensile stresses are produced by the vibrations in the vicinity of the clamps. This eventually leads to fatigue damage of the conductor (Fig. 1.1) in the form of broken strands in the outer layers, usually at suspension clamps. Other damages include breakage of hardware such as insulator strings, strain link, strain plates, shackle, and ball clevis. In some cases, these failures may occur within the first year of construction.

Most of transmission lines utility organizations used Stockbridge dampers to control *aeolian vibration*. The role of the damper is to minimize or eliminate the vibration by reducing the vibration amplitude to a safe level. The effectiveness of the damper depends on the conductor characteristics (i.e, mass and tension of the conductor) and the location of the damper. Investigations in [5, 6] show that a damper is most effective when it is designed to cover a wide range of frequencies and when it is appropriately positioned on the conductor. Stockbridge dampers are designed to fit a wide range of conductor diameters. This range can vary between 3 to 10 mm.

1.2 Motivation

Most often generation power plants are located in remote areas, far from cities. As such, high voltage transmission lines are needed to transport power to urban areas. Millions of transmission towers and thousands of kilometers of overhead power lines are used worldwide to supply electricity. In the province of Ontario, the overhead transmission and distribution system stretch over 150,000 km [7]. The design and construction cost of these transmission lines can be very expensive. Some of the cost can be reduced by designing the transmission lines using lower structures. This is usually possible by increasing the tension of the conductor in order to meet the minimum required clearance. However, it has been shown that the conductor is more prone to vibration at higher tension. In other words, raising the conductor tension can cause more vibration and eventually can lead to fatigue failure.

Over the years, special care has been undertaken by transmission lines utility organizations to control *aeolian vibration*. Some organizations limit their design tension to 20% and 25% of the rated tensile strength (RTS) in the summer and winter season, respectively [7, 8]. However, several transmission lines failures continue to occur. In 2005 Hydro One customers in Sarnia experienced a power outage due to transmission lines failure. The breakage of the conductor and damper is shown in Fig. 1.2. Three years later, another transmission lines failure occurred in London, Ontario. Fig. 1.3 shows the broken torsional damper of the transmission line. Investigations showed that the failure of both lines were attributed to *aeolian vibration* [9].

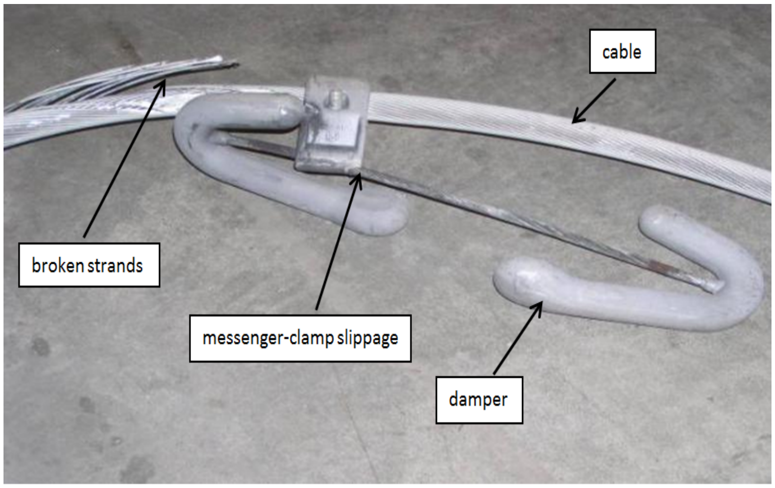

Figure 1.2: Broken conductor strand and slippage of the messenger wire of the Stockbridge damper [9].

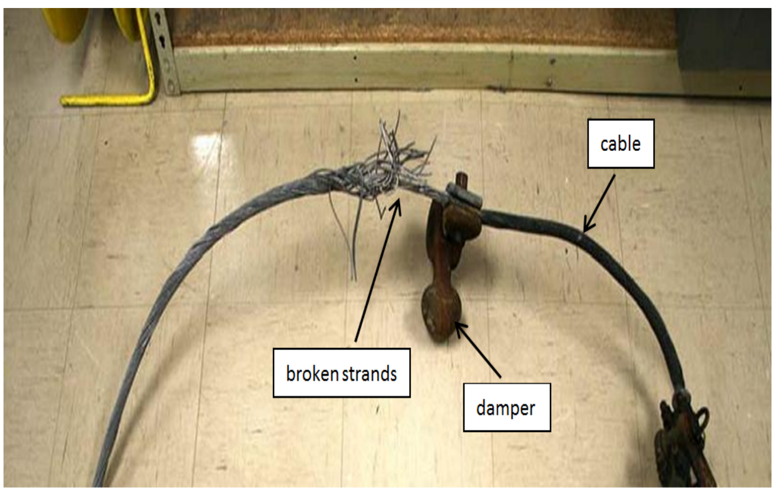

Figure 1.3: Sample of conductor and torsional damper failure on Cowal junction to Longwood TS in London [10].

Other high voltage organizations have also reported transmission lines failure due to vibration. For instance, in 1996 Manitoba Hydro company reported failure of 19 transmission towers which resulted in damage that cost the company about 10 million USD [11]. In 2009, some customers of *Electricité de France* experienced a blackout due to the collapse of 45 towers in the southern part of France. These failures were also attributed to *aeolian vibration* [12].

The aforementioned examples of failures indicate that the control of *aeolian vibration* is still a challenge. As such, it is crucial to further examine the dynamics of conductors and dampers, and thereby assist transmission line design engineers in deciding on the limitation of the design tension of the conductor and optimal selection and location of dampers.

1.3 Literature review

Aeolian vibration of overhead transmission lines is characterized by the interaction of the dynamics of the conductor and Stockbridge damper with fluid dynamics. The fluid dynamics govern the wind force that causes *aeolian vibration*. The dynamics of the conductor and Stockbridge damper capture the motion of the conductor and Stockbridge damper in response to the applied wind force.

1.3.1 Conductor dynamics

Conductors are made of several layers of individual round wires packed tightly together in concentric counter-rotating helices (Figs. 1.4 and 1.5). Aluminum conductor steel reinforced (ACSR) is the most common conductor used in overhead power lines because of its high tensile-strength-to-weight ratio. ACSR conductor consists of aluminum outer strands and steel inner strands. Most of the power is transmitted through the aluminum outer layers. The inner strands of steel are for the strength required to support the weight without stretching the aluminum. The higher strength conductors are usually used for river crossing (longer span) since this requires more resistance. T-2 conductor is another type of conductor used in overhead power lines. It is a two standard round conductors twisted around each other, and it is designed to resist vibrations. Other conductors used in Transmission lines include all aluminum conductors (AAC) and all aluminum alloy conductor (AAAC).

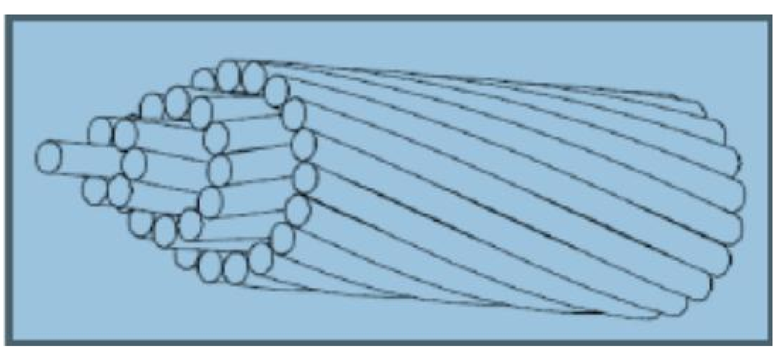

Figure 1.4: Structure of a conductor [1].

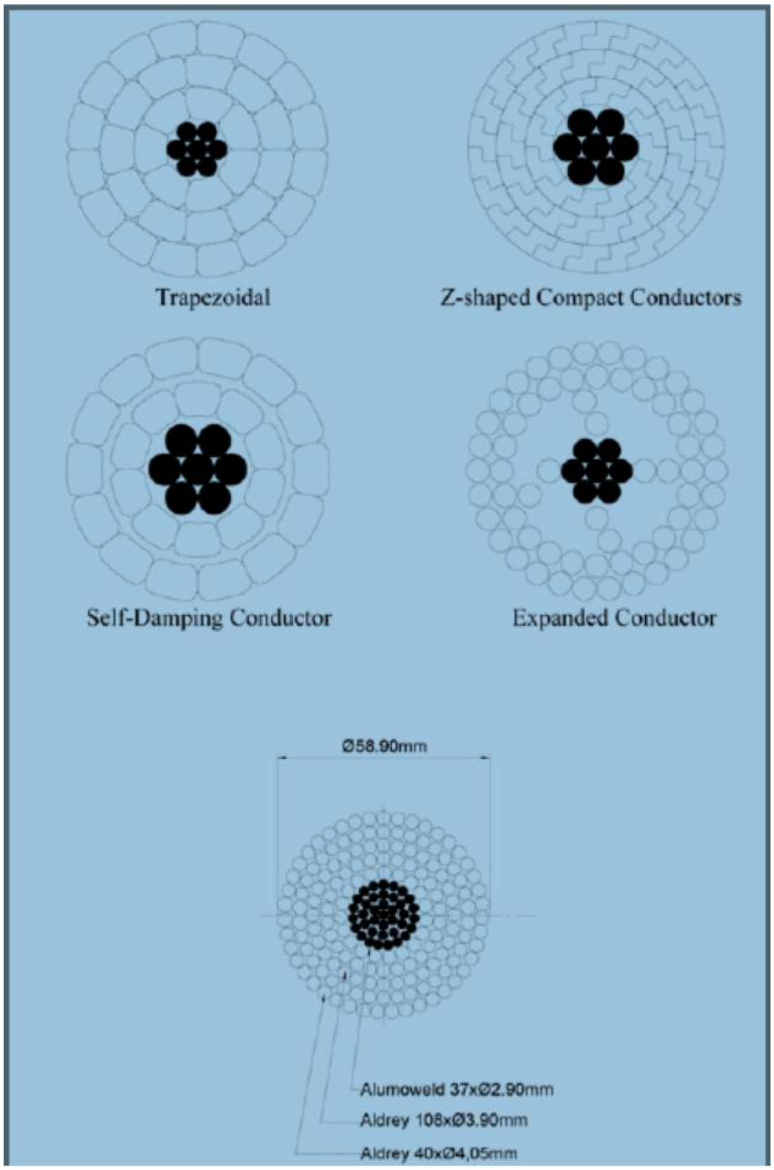

Figure 1.5: Cross section of special conductors [1].

The dynamics of the conductor can be idealized as the vibration of an axially loaded Euler-Bernoulli beam. Claren and Diana [6] were among the earliest investigators to examine *aeolian vibration* of transmission lines. They analytically and experimentally determined the natural frequencies of the conductor without damping. The effect of the conductor flexural rigidity on natural frequencies was investigated by Dhotarad et al. [5]. The differences in the values of natural frequencies observed in the simply-supported end cable (with and without flexural rigidity) were less than 3%. They hypothesized that the location of the dampers had negligible effect on strain for low frequency excitation (i.e., low wind speed). Barbieri et al. [13] performed free vibration analysis of a single conductor without damping using Galerkin method and experimentally validated their results.

For a complete dynamic model of a conductor, many experiments have been conducted to determine the self-damping of the conductor. Past investigations on this topic have resulted in the development of empirical formulae to predict the power dissipation of the conductor. An exponential form that contains constants that depend on the conductor parameters has been suggested [14, 15, 16, 17, 18, 19].

1.3.2 Stockbridge damper Dynamics

Most engineering structures such as airplanes, cables, bridges, ships and many more can experience vibrations which eventually cause fatigue failure. These vibrations can be suppressed by means of dampers. One of the first damping devices for vibration bodies was invented in the early 1900s by Hermann Frahm [20]. The role of the damping device was to annul the resonance vibrations of the main body.

The Stockbridge damper has similar purpose to that of Frahm; that is, it can eliminate or reduce *aeolian vibration* by absorbing the energy from the wind in order to stabilize the motion of the conductor. Dampers control *aeolian vibration* by reducing the strain level at the suspension clamp to a safe strain limit of 200 μm/m [21]. The effectiveness of a damper depends on its response within its frequency band [22, 23]. Based on a rule of thumb, it was thought that dampers' locations will not coincide with a node provided these locations are less than the loop length corresponding to the highest expected vibration frequency.

Stockbridge damper was invented by George H. Stockbridge in 1925. It is a dumbbell-shaped device with a mass at each end of a short flexible cable or rod called the messenger cable. The damping mechanism is observed as vibrations of the conductor that are transferred through the clamp to the messenger cable. The flexuring of the messenger causes slipping between its strands and consequently induces the weights (called counterweights) at their ends to oscillate. By carefully choosing the parameters of the damper (such as the mass of the counterweights, length, and the stiffness of the messenger), the energy imparted on the conductor from the wind can be greatly dissipated by the Stockbridge damper.

George Stockbridge claimed in his patent that a short (i.e., 30 in or 75 cm) and very flexible messenger increases damping effectiveness [23]. Furthermore, the use of concrete or similar material for the weights in lieu of metallic weight was recommended because no charging current is absorbed by concrete material [23]. However, this idea was quickly rejected because of the poor mechanical performance of concrete. The first Stockbridge damper, as patented by George Stockbridge, had a concrete block at each end and it is shown in Fig. 1.6.

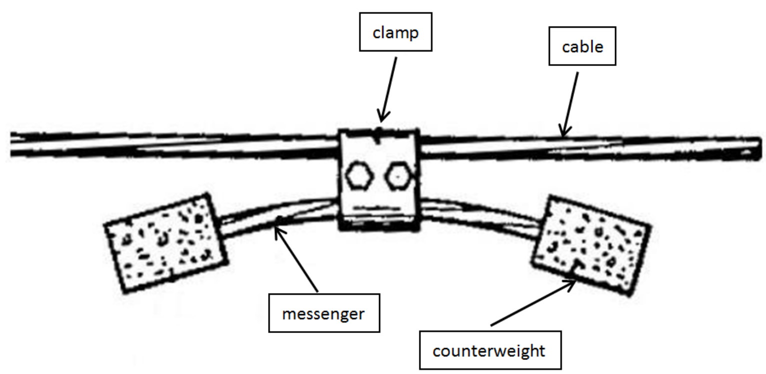

Figure 1.6: Stockbridge's original concrete block design [23].

Modern dampers shown in Fig. 1.7 use metal bell-shaped weights. The bell is hollow and the damper cable is fixed internally to the distal end, which permits relative motion between the cable and damping weights. There are two types of modern Stockbridge dampers, the 2R damper and 4R damper. The former, 2R damper, also known as the symmetric Stockbridge damper, has identical weights and messenger lengths at both ends. Given that this damper consists of two identical weights, the moment exerted by one is neutralized by the other. This 2R damper is characterized to possess two natural modes of vibration when the motion of the clamp is restricted to the vertical plane. The second type, 4R damper, is called the asymmetric Stockbridge damper. It consists of different weights and cable lengths on each side. Consequently, a resultant moment is induced by the unbalanced weights at the ends and this results in four resonant frequencies.

The cable of the Stockbridge damper shown in Fig. 1.8 is called messenger. This messenger is generally made of galvanized steel, but stainless steel is used in more polluted areas. Both materials result in the same damping capacity; however, stainless steel provides better fatigue resistance. The clamp of the damper which is used to hang on to the conductor is made of aluminum alloy. This is to ensure that the weight is small enough to restrict its motion to the vertical plane for higher conductor vibration frequencies. In the past, damper counterweights were made of zinc alloy, but due to the rise in cost of this material, forged steel weights or extruded steel rods are used instead.

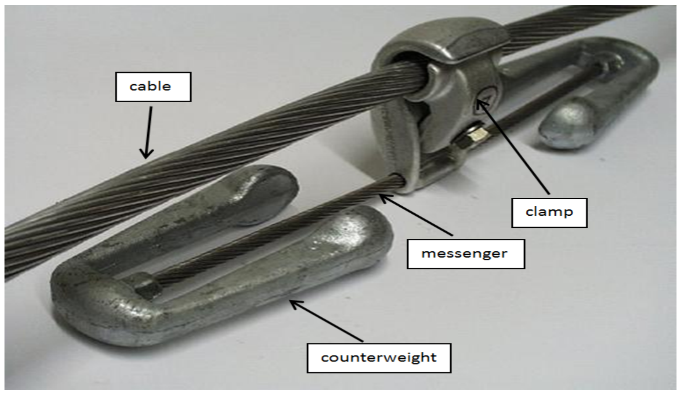

Figure 1.7: Stockbridge damper [1].

Figure 1.8: Stockbridge damper cable [1].

The dynamics of Stockbridge dampers have been examined by numerous authors. The common approach is to experimentally determine its impedance curve [24]. Another approach is to model the Stockbridge damper as a two degree-of-freedom system [25, 26]. The dynamic response of a Stockbridge damper was examined by Wagner et al. [26]. In their analysis, the authors assumed massless messenger and model the clamp as a base motion and the counterweight as a rigid mass. Their proposed model was experimentally validated. Feldmann [27] investigated the effects of Stockbridge dampers using theoretical and experimental approaches. It was found that the Stockbridge damper is remarkably efficient, and the counterweights do not dissipate energy but produce a coupling between the damper and the conductor which makes them good disturbers of *aeolian vibration*.

Markiewicz [28] presented a method and a computational model for the evaluation of the optimum dynamic characteristics of Stockbridge dampers to be mounted near tension insulator assemblies (dead end span). It was suggested that Stockbridge dampers be designed so that their mechanical impedance matches as closely as possible to the determined optimum damper impedance for the cable to be protected. The advantage of a Stockbridge-type vibration damper with low-mass clamp over a conventional Stockbridge vibration damper with bolted clamp was examined by Krispin [29]. Theoretical and experimental analysis were used to show that the conventional Stockbridge damper is not effective for controlling the vibration of smaller size conductor such as optical ground wires (OPGW). He, therefore, recommended the use of *low clamp mass* dampers because they improve power dissipation (damping performance) in the upper range frequencies.

The dynamics of the Stockbridge damper was examined experimentally by Vecchiarelli [30, 31]. His experimental results showed that the energy dissipated by a Stockbridge damper varies highly with the vibration frequency and the displacement amplitude of the damper clamp. His other observation was that the displacement of the damper clamp depends on the location of the damper as such he indicated that the energy dissipated by the damper can be significantly affected by the positioning of the damper on the conductor.

A rule of thumb was developed by EPRI [1] to determine the optimum location of the damper. In order to avoid positioning the damper at a node, it was postulated that the damper should be placed at a distance between 70% and 80% of the loop length corresponding to the highest wind speed of 7 m/s. The location of the damper was also examined by Nigol and Houston [32]. They indicated that dampers should never be placed at any point of symmetry along the conductor (i.e, 1/4, 1/3, 1/2, etc.) because they fail to provide vibration protection at every 4^{th}, 3^{rd}, and 2^{nd} harmonic [32].

1.3.3 Fluid dynamics

The nature of the flow in *aeolian vibration* of conductors is similar to that of an uniform flow of air across a rigid cylinder. This flow depends on the Reynolds number, which is defined as the ratio of inertial forces to viscous forces. With respect to *aeolian vibration*, the Reynolds number varies between 2700 and 14000 [33]. *Aeolian vibration* is caused by alternating vortices. As the vortices are shed from the surface of the conductor normal to the wind, they cause a resultant force that acts in the transverse direction. This force is periodic with a Strouhal frequency f_s, which is proportional to the wind speed and inversely proportional to the diameter of the conductor. The parameter of proportionality is called Strouhal number and it varies from 0.15 to 0.25. In general, the average Strouhal value is taken as 0.2.

Diana and Falco [34] examined the vibration of a rigid cylinder and found that the lift force acting on the cylinder is similar to the vibration response of the cylinder since they are both harmonic at steady state. This finding was verified by Bishop and Hassan [35] and by Bearman and Currie [36]. It was observed that during resonance the lift force leads the displacement by a phase angle ranging from 0-180 degrees. It was experimentally shown by Griffin and Koopmann [37] that this lift coefficient is significantly dependent on the amplitude of vibration of the rigid cylinder.

1.3.4 Current models

The most common method to predict *aeolian vibration* of a single conductor is the energy balance method (EBM). The vibration level of the conductor is evaluated by determining the balance between the energy imparted to the conductor by the wind and the energy dissipated by the conductor (via conductor self-damping) and the added dampers. Oliveira et al. [38] developed a dynamical model of *aeolian vibration* to predict the amplitude of steady-state motion of the conductor based on EBM. They included a method for solving the time-dependent Navier-Stokes equation. Kraus and Hagedorn [16] also employed the EBM to examine vibration magnitudes. Their results were compared to those obtained from a wind tunnel experiment. The optimal position of Stockbridge dampers along the span of the conductor was investigated by Verma and Hagedorn [39]. To avoid locating dampers on nodes for system natural frequencies of less than 50 Hz, they analytically showed that it was sufficient to maintain approximately 1 m maximum distance between adjacent dampers.

The method of impedance is also another method used to evaluate *aeolian vibration* of a single conductor transmission lines. Tompkins et al. [40] examined the interaction of a conductor with a damper using the electrical-mechanical impedance method. This model was reformulated in solely mechanical-impedance terms by Rawlins [41] and then used to analyze conductor vibrations. Further extension of the model was proposed by Nigol and Houston [32] who included the boundary conditions at both ends and considered the arbitrary location of the excitation source. Their model was experimentally verified and it was used to demonstrate optimum damping concepts.

A major drawback of both the impedance and EBM approach is the limitation to only one-way coupling between the conductor and damper. Specifically, the dynamics of the damper influenced that of the conductor but not the converse. Another weakness is that these two methods ignore some crucial parameters of the damper or conductor such as flexural rigidity of the conductor and messenger, and the mass of the damper. An attempt to depart from the above-mentioned conventional methods of modeling a single-conductor transmission line was reported in Refs. [2, 42, 43, 44]. Both conductor and damper were modeled as one unified system in order to account for their two-way coupling. The finite element method was used to determine the system natural frequencies and time responses. While the efficacy of the finite element model was demonstrated, the procedure was very complicated and computationally intensive. Further, the finite element method is an approximate technique.

1.4 Objectives

The aim of the present study is to address shortcomings of the previous methods of modeling a single-conductor transmission line by presenting analytical approaches that yield exact solutions with minimal complications. Hitherto the analytical modelling and analysis of the two-way coupling of the cable-damper system has not been investigated. The objectives of this dissertation are threefold:

1. Conduct experiments to determine the damping characteristics, as well as, natural frequencies and response of a single conductor with and without a Stockbridge damper.

2. Develop novel analytical models of a single conductor with Stockbridge dampers.

3. Design a damping arrangement scheme by optimizing the location of the Stockbridge damper.

1.5 Organization of the thesis

In chapter 2, two sets of experimental analysis are presented to determine the damping coefficient of the conductor and the Stockbridge damper. The generated data were then used to validate the mathematical models in the next chapters. The first set of experiments pertain solely to the Stockbridge damper that was directly mounted on the shaker.

In the second set of experiments, the Stockbridge damper was attached to the span of a conductor and the shaker was placed at mid-span to excite the conductor.

In chapter 3, the Stockbridge damper is reduced to a spring-mass-damper system, hence the conductor-damper system is modeled as a beam with a spring-mass-damper. Chapter 4 presents the analytical model of the conductor-damper system that is modeled as a double beam system. In both chapters 3 and 4, expressions are presented for the characteristic equations, mode shapes, and orthogonality conditions. Parametric studies are conducted to examine the effect of conductor and damper parameters on the natural frequency and response of the system.

Chapter 5 discusses the design of the damping arrangements scheme in order to determine the optimal damper location required to protect the conductor from fatigue failure. Finally, the conclusion and future work are discussed in chapter 6.

Chapter 2

Experimental Analysis

2.1 Introduction

This chapter describes the two sets of experiments that were carried out to determine the equivalent damping coefficient of the Stockbridge damper and the self-damping ratio of the conductor, as well as to validate the models outlined in the next chapters. The first experiment is on the forced-response test of Stockbridge dampers on a shaker and the second experiment pertained to a conductor with and without an attached Stockbridge damper using the forced method as well. All the tests were performed in accordance with IEEE [45] and IEC [46] standards. The equipment and apparatus used to conduct the experiments are discussed in detail. Also, the procedure and results of each set of experiments are outlined.

2.2 Apparatus

The main apparatus used to conduct the testing were: an electro-dynamic shaker, strain gauge load cells, accelerometers, and charger amplifiers. An electro-dynamic shaker is a vibration exciter capable of generating sinusoidal force. The shaker used for this test was able to control the vibration amplitude and frequency to an accuracy of $\pm 2\%$. The disadvantage of the shaker was that frequency lower than 10 Hz could not be measured.

The load cell is a strain-gauge based sensor containing a Wheatstone bridge. When a force is applied, the load cell experiences a change in strain which results in the unbalance of the Wheatstone bridge. Two load cells were used in this experiment. The one depicted in Fig. 2.1 measured the force of the shaker with a capacity of 2225 N. The other, depicted in Fig. 2.2, was used to measure the tension of the conductor and has a capacity of 50

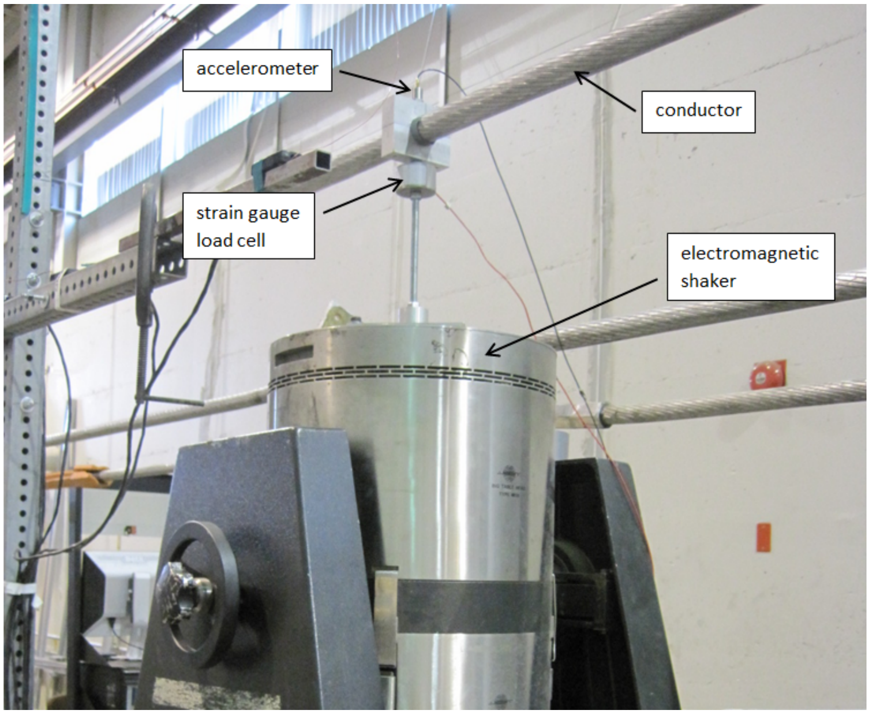

Figure 2.1: Photograph of the conductor, shaker (B&K 4802), load cell, and accelerometer.

kN.

The piezoelectric accelerometer, depicted in Fig. 2.3, is an electromechanical device used to measure acceleration. It consists of two metal beams or microstructures that have capacitance between them. The movement of one structure by an accelerative force results in a change of capacitance. This capacitance is then converted to voltage through some circuitry. The resulting voltage is related to the acceleration.

Charger amplifiers were used to filter electronic noise resulting from component possessing higher frequencies. Both the force and acceleration signals required filtering in order to avoid problems due to aliasing (noise). Two charger amplifiers were used: one for the piezoelectric accelerometer and the other for the load cell.

2.3 Stockbridge damper test

This section discusses the experimental analysis of the Stockbridge damper using the forced response method. Measurements were taken of the force transmitted by the shaker to the damper, the velocity of the damper, and the phase angle between the force and the velocity. These measurements were used to calculate the damping coefficient of the

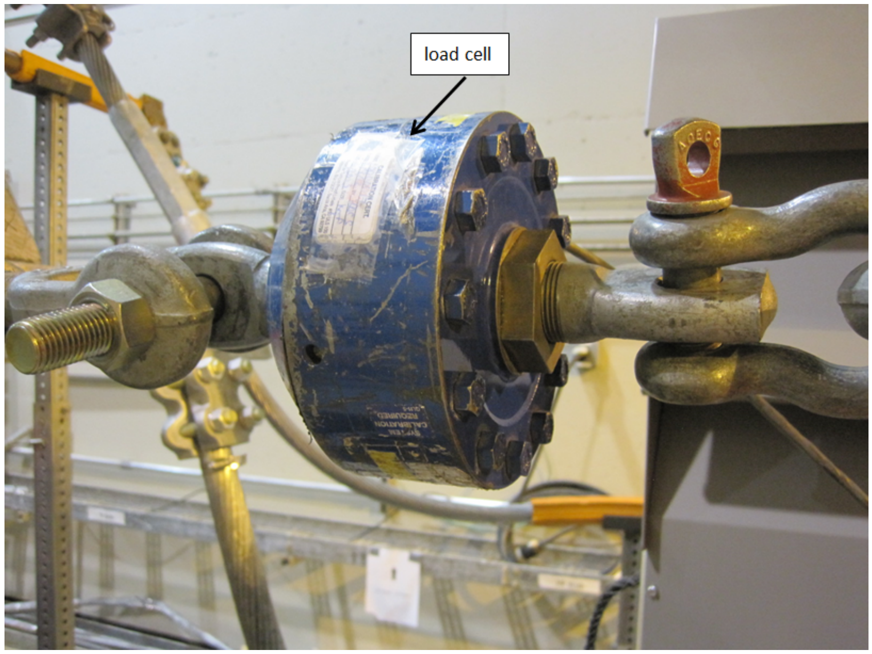

Figure 2.2: Photograph of the Load cell for tension measurement.

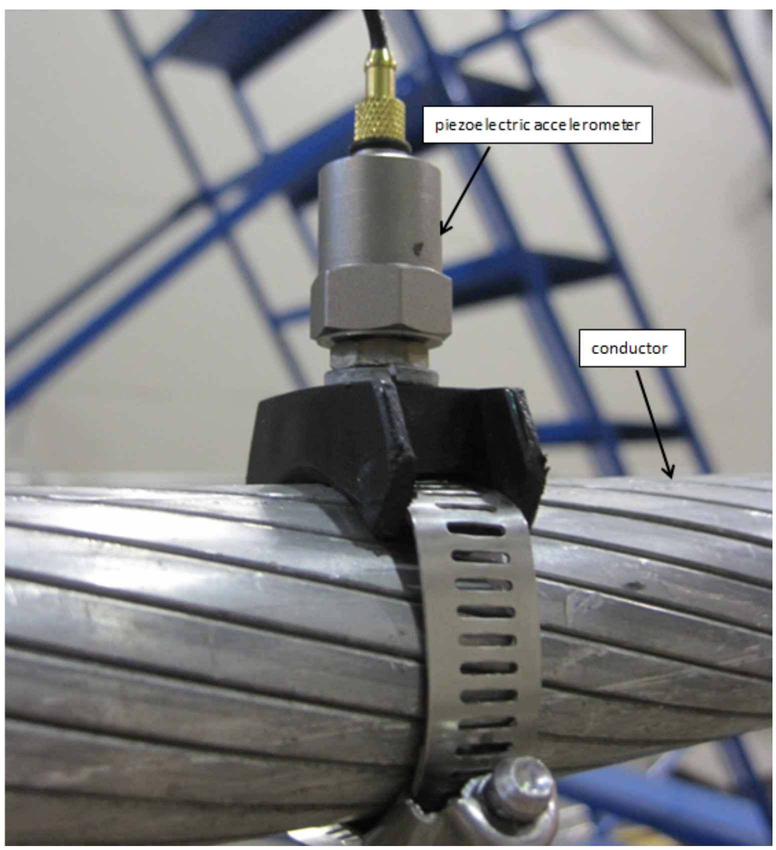

Figure 2.3: Free loop piezoelectric accelerometer.

tested Stockbridge dampers. The resonant frequencies of the damper were then obtained using the damping coefficient curve. In the following subsection, the forced response method, the test set-up, procedure, and results are presented.

2.3.1 Forced response method

In the forced-response method (see IEEE guide [45]), the damper is directly mounted on a shaker and the damper is tested at frequencies within the range of Strouhal frequencies corresponding to wind velocity of 1-7m/s. IEEE guide recommends a constant damper clamp velocity. The power dissipated by the damper is given as

$$P_{\mathrm{d}} = \frac{1}{2} F V_{\mathrm{c}} \cos\phi_{\mathrm{FV}} \tag{2.1}$$

where F is the force transmitted to the shaker by the damper, V_{c} is the measured velocity at the clamp, and ϕ_{FV} is the phase angle between the force and the velocity.

2.3.2 Experimental procedure and results

The main objective of this test is to determine the characteristics of the Stockbridge damper. The Stockbridge damper is often postulated to be dependent on the forcing frequency and the conductor vibration velocity at the location of the damper clamp [31, 32, 47, 48]. This Stockbridge damper can be modeled as an equivalent viscous damping coefficient [49]. Following [31], the equivalent damping coefficient, c_{d}, of the Stockbridge damper can be expressed as:

$$c_{\mathrm{d}} = \frac{E_{\mathrm{d}}\omega}{\pi V_{\mathrm{c}}^2} \tag{2.2}$$

where

$$E_{\mathrm{d}} = \frac{P_{\mathrm{d}}}{f} \tag{2.3}$$

E_{d} and P_{d} are the energy and power dissipated by the damper over a complete cycle, respectively. The excited frequency in Hz is denoted by f.

A schematic of the experimental set-up is shown in Fig. 2.4. The Stockbridge damper was mounted on an electrodynamic shaker. A load cell was installed between the shaker and the fixture to measure the delivered force and an accelerometer was placed at the clamp to measure the velocity of the damper. The characteristics of the tested Stockbridge damper are as follows: the flexural rigidity is $E_{\mathrm{m}}I_{\mathrm{m}} = 31.8$ Nm^2 and mass per unit length is $m_{\mathrm{m}} = 0.25$ kg/m. The mass of the right and left counterweights are respectively

m_1 = 3.4 kg and m_2 = 1.46 kg. The length of the messenger on the right and left are l_1 = 0.22 m and l_2 = 0.3 m, respectively.

The Stockbridge damper was excited in the range of wind-induced vibration (sweep) at a constant velocity of 100 mm/s. The frequency range was confined to frequencies greater than 10 Hz because the shaker was ineffective at frequencies lower than 10 Hz. Both load cell and accelerometer were connected to a dynamic signal analyzer through charge amplifiers. For each tested frequency, values were recorded for the input force from the shaker, velocity at the clamp, and phase angle between the force and the velocity. The recorded frequency, force, and velocity at the clamp are employed in Eq. (2.2) to obtain the equivalent damping coefficient of the Stockbridge damper. A plot of c_d against the recorded frequencies is shown in Fig. 2.5. The frequencies corresponding to the observed peaks are the resonant frequencies of the Stockbridge damper.

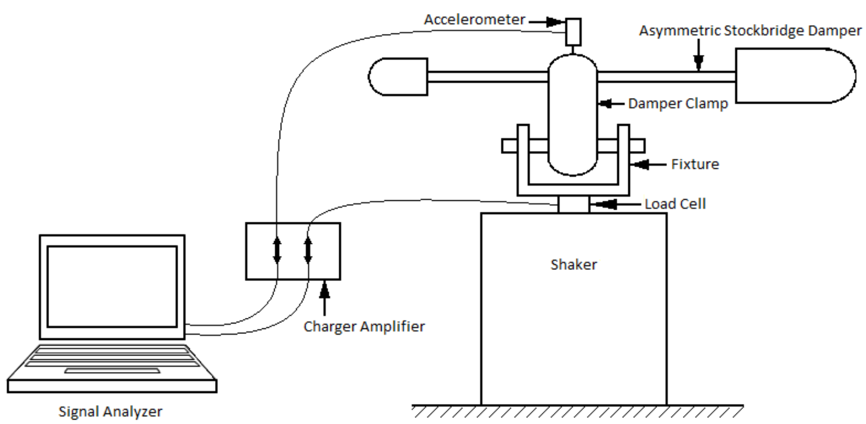

Figure 2.4: Schematic of the Stockbridge damper experimental set-up

2.4 Conductor test

The experimental data of the conductor were also acquired through the forced response method which was described in the previous section. The main objective herein was to determine the conductor self-damping, the natural frequency and response of the conductor-damper system. The conductor, Drake 795 Kcmil, was tested at 20 and 25 %RTS (rated tensile strength). The testing procedure can be described in three steps. The first step was to establish the resonant frequencies. The second was to locate the antinode and the last step was to measure and record the vibration amplitude of this antinode, excitation force, and phase angle between the force and the vibration amplitude.

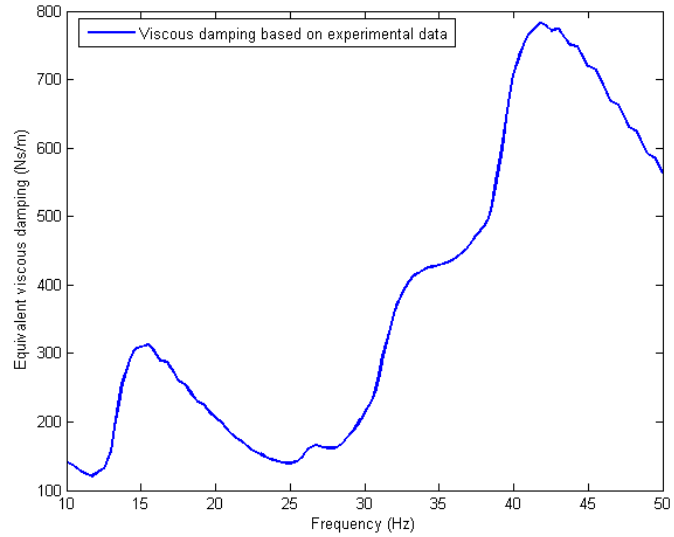

Figure 2.5: Equivalent viscous damping coefficient of the Stockbridge damper

It is noted that after reaching a stationary condition, all the energy imparted to the span by the shaker is equal to that dissipated by the conductor over one vibration cycle; that is, all the energy introduced by the shaker is dissipated by the conductor self-damping. As such, the energy dissipated by the conductor is given as [46]

$$E_{\mathrm{diss}} = \pi F y_{\mathrm{f}} \sin(\theta_{\mathrm{d}}) \tag{2.4}$$

where F is the driving force from the shaker, y_{f} is the displacement of the conductor at the location shaker (0 to peak), θ_{d} is phase angle between displacement and driving force.

The maximum kinetic energy of the cable is given as

$$E_{\mathrm{k,max}} = \frac{1}{4} m_{\mathrm{c}} L_{\mathrm{c}} \omega^2 y_0 \tag{2.5}$$

where m_{c} is the conductor mass per unit length, L_{c} is the span length, y_0 denotes the antinode vibration amplitude and ω is the corresponding resonant circular frequency. The non-dimensional damping ratio is defined as

$$\zeta = \frac{1}{4\pi} \frac{E_{diss}}{E_{k,max}} \tag{2.6}$$

The expression of the damping ratio of the conductor is now obtained by substituting

Eqs. (2.4) and (2.5) into Eq. (2.6)

$$\zeta = \frac{F y_f \sin \theta_d}{m L \omega^2 y_0} \tag{2.7}$$

2.4.1 Experimental procedure

The experimental investigations were carried out on a 27.25 m test span depicted in Fig. 2.6. A schematic of the test set-up is depicted in Fig. 2.7. The conductor was attached to a dead-end clamp on both ends, which were connected to linear bearings mounted on intermediate abutments made of steel reinforced concrete as shown in Fig. 2.8. The conductor was then locked solidly to an insulator clamp at each end. The clamps were suspended on steel reinforced concrete towers as depicted in Fig. 2.9. A hydraulic ram (cylinder) as depicted in Fig. 2.10 was installed at the south-end of the test-span to string the conductor at a desired tension. A cantilever weight (pulley system) shown in Fig. 2.11 was used at the north-end of the test-span to maintain a constant tension throughout the span. A maximum torque of 40 Nm was used to secure the damper on the conductor.

One load cell was placed at the end to monitor the tensile load. The other load cell and an accelerometer were used to measure the input force and velocity from the shaker to the conductor, respectively. The shaker was placed at mid-span. Another accelerometer was placed on an antinode of the corresponding forcing frequency to measure the vibration displacement.

The conductor with and without damper was then vibrated at various frequencies and power levels based on the Alcoa wind power curve derived from wind tunnel tests on flexible cable [15]. The voltage signal from the load cell and accelerometer were sent through charger amplifiers(low-pass filter) by means of coaxial cable and then to a digital data acquisition system for recording.

2.4.2 Experimental results

The parameters of the tested conductor and Stockbridge damper are tabulated in Table 2.1. The damper was attached at a distance of 0.94 m from the last point of contact of the suspension clamp and the conductor.

The frequency response curve of the signal analyzer was used to measure the natural frequencies. That is, the peaks in the amplitude portion of the frequency-response function give the natural frequencies of the conductor. This was observed when the force is at minimum and the velocity is at maximum.

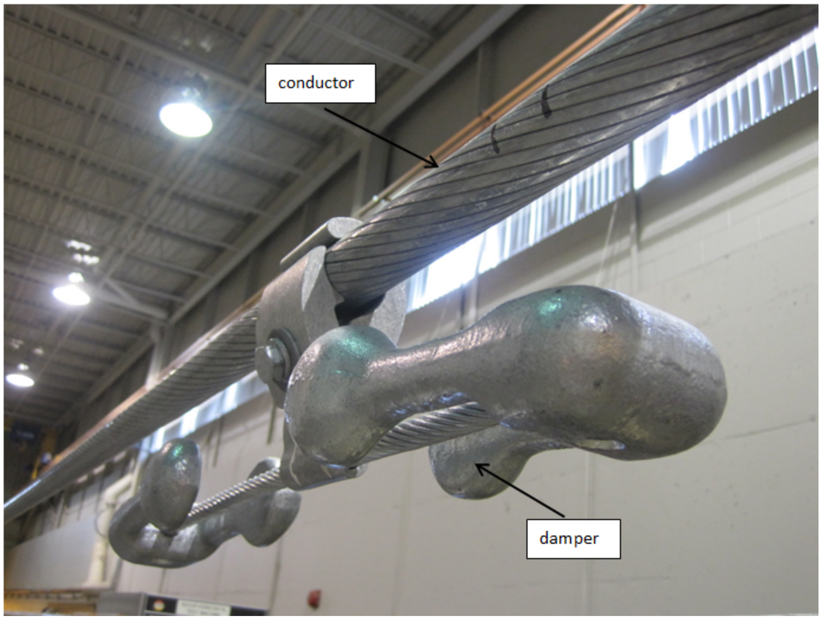

Figure 2.6: Conductor span with a Stockbridge damper.

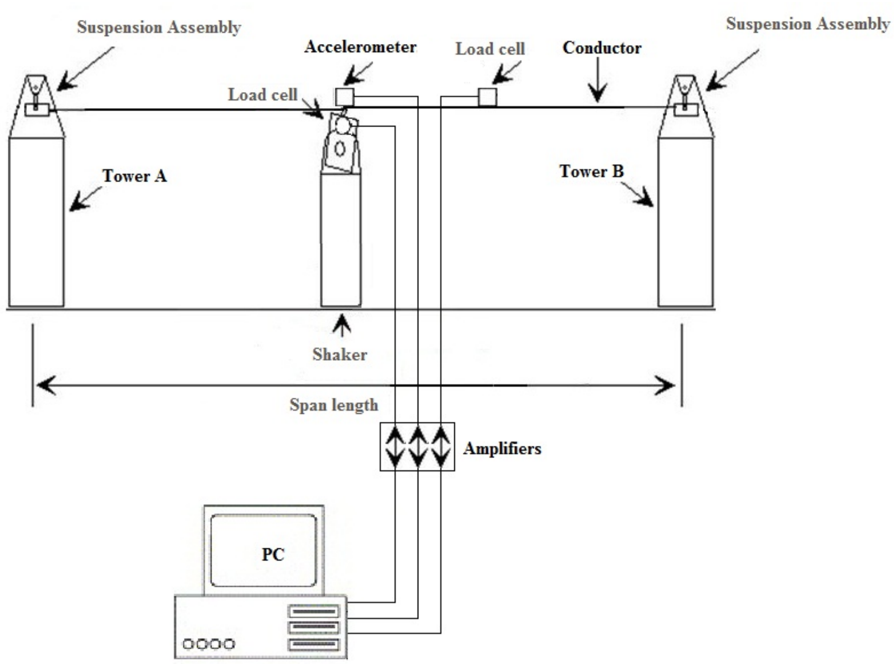

Figure 2.7: Schematic of experimental set-up.

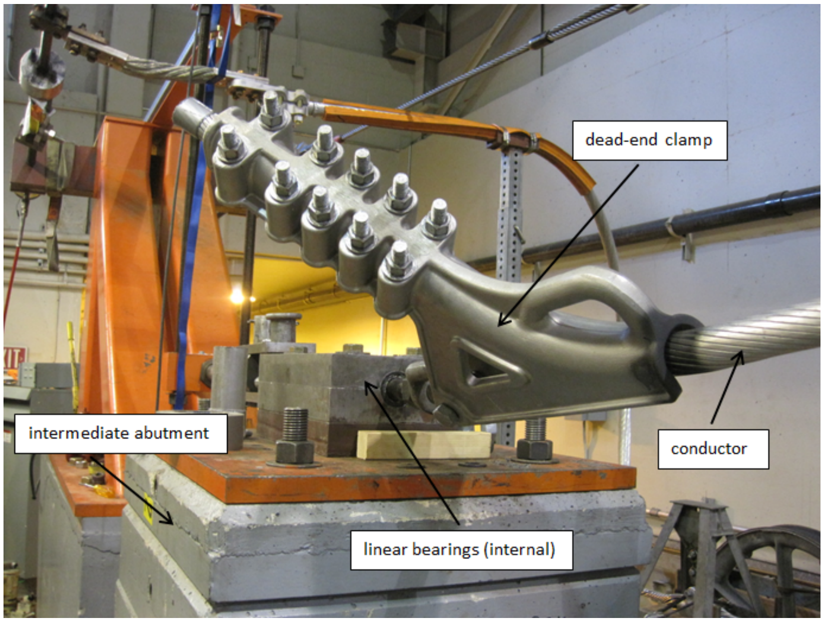

Figure 2.8: Intermediate abutment dead-end clamps.

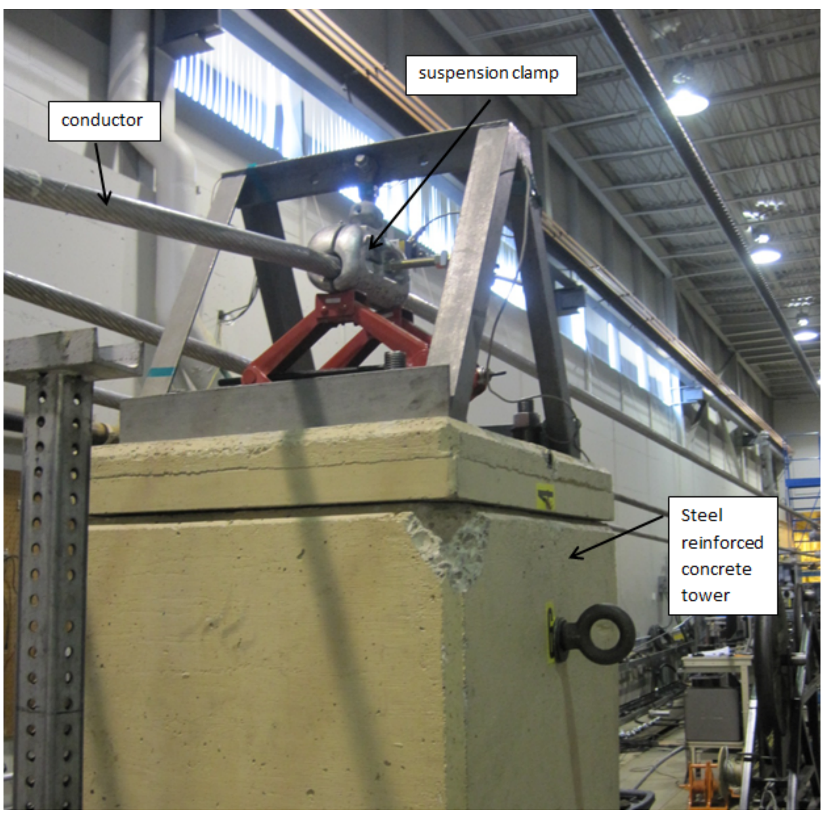

Figure 2.9: Steel reinforced concrete towers and suspension clamp.

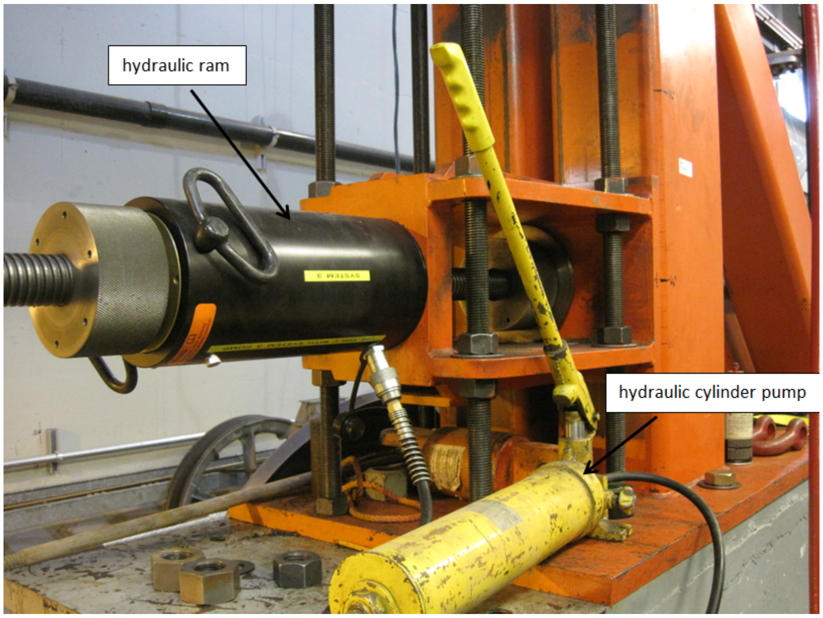

Figure 2.10: Hydraulic cylinder.

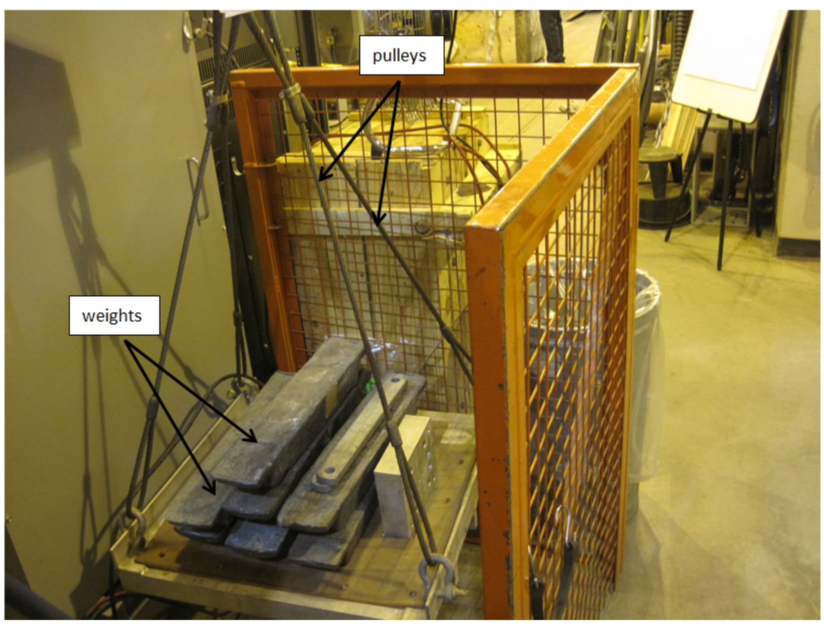

Figure 2.11: Cantilever weight (pulley system).

Table 2.1: Conductor and damper parameter

Parameter	
h	0.05 m
$E_{\mathrm{c}}I_{\mathrm{c}}$	1602 Nm^2
m_{c}	1.628 kg/m
D	28.143mm
RTS	139.2kN
m_1	3.4 kg
m_2	1.46 kg
I_1	0.0175 kgm^2
I_2	0.015 kgm^2
$E_{\mathrm{m}}I_{\mathrm{m}}$	31.8 Nm^2
L_{m_1}	0.3 m
L_{m_2}	0.22 m
m_{m}	0.25 kg/m

The natural frequencies of the conductor with and without a Stockbridge damper are presented in Table 2.2 for 20 and 25% RTS (rated tensile strength). It is observed from Table 2.2 that the natural frequencies of the bare conductor are slightly higher than those of the loaded conductor. The measured vibration amplitudes of the conductor with and without damper are shown in Fig. 2.12. As expected, the vibration amplitude of the conductor with and without damper decreases with increasing frequency. This is because the conductor self-damping increases with the frequency. However, the rate at which the vibration amplitude of the conductor with damper decreases is much higher than that of the conductor without damper. This is an indication that attaching a Stockbridge damper to the conductor significantly reduces the vibration amplitude.

With regard to the conductor self-damping ratio, only the bare conductor was tested (i.e., no damper was attached). The recorded data indicate that the damping ratio is significantly dependent on the excitation frequency, vibration displacement, and the conductor tension. This conclusion is in agreement with [34]. The conductor self-damping ratio can be expressed as

$$\zeta = \frac{C f^{\alpha} Y^{\beta}}{T^{\gamma}} \tag{2.8}$$

where f is the excitation frequency in Hz, Y is non-dimensional peak-to-peak displacement (non-dimensionalized with respect to the conductor diameter),T is the conductor tension, C, α, β, and γ are constants. Using linear regression analysis, the constants in Eq.(2.8) were determined to be $C = 20760$, $\alpha = 1.406$, $\beta = 0.298$, and $\gamma = 1.835$. It should be noted that the linear regression analysis was based on the experimental data

Table 2.2: Experimental natural frequencies (Hz).

Mode	$T = 27.84$ kN		$T = 34.8$ kN	
	Bare conductor	Loaded conductor	Bare conductor	Loaded conductor
1	-	-	-	-
2	-	-	-	-
3	-	-	-	-
4	-	-	-	-
5	-	-	-	-
6	-	-	-	-
7	12.2330	12.0956	13.6720	13.0749
8	15.1490	14.3910	16.6780	15.5104
9	17.2000	16.5942	19.2800	17.5942
10	20.1180	19.1878	21.9522	20.8396
11	22.2010	21.1717	24.9180	22.7073
12	25.1050	23.6302	27.2153	24.5587
13	27.4090	25.3417	30.8245	27.0885
14	31.1070	27.7020	33.6452	27.7641
15	32.9240	29.3096	36.1602	31.4490
16	34.3010	31.4913	38.9175	34.0577
17	36.1900	33.8856	42.2660	36.5584
18	38.9530	36.6252	44.2518	40.0444
19	41.5690	39.3756	47.2281	42.6807
20	44.9530	42.6673	50.0215	45.7943

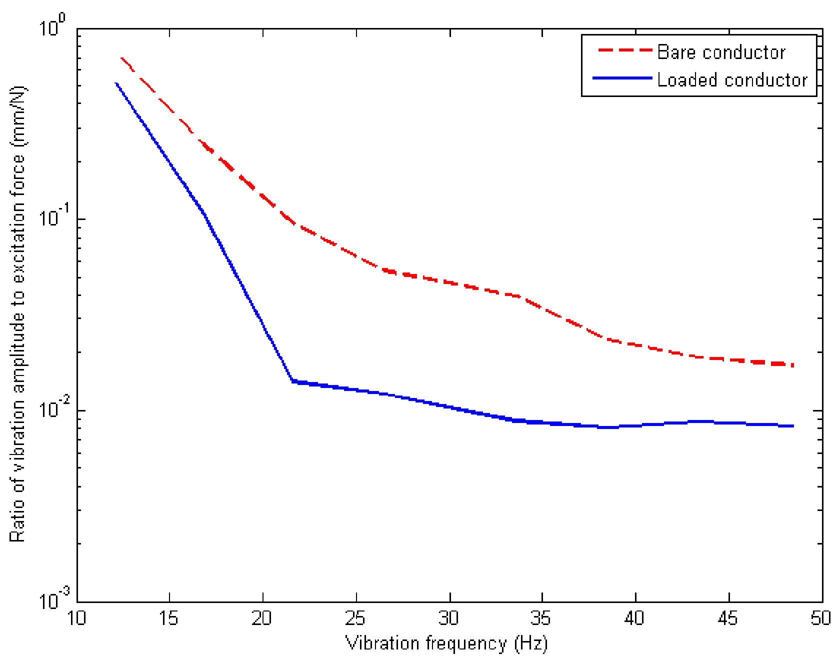

Figure 2.12: Frequency response of conductor with and without damper.

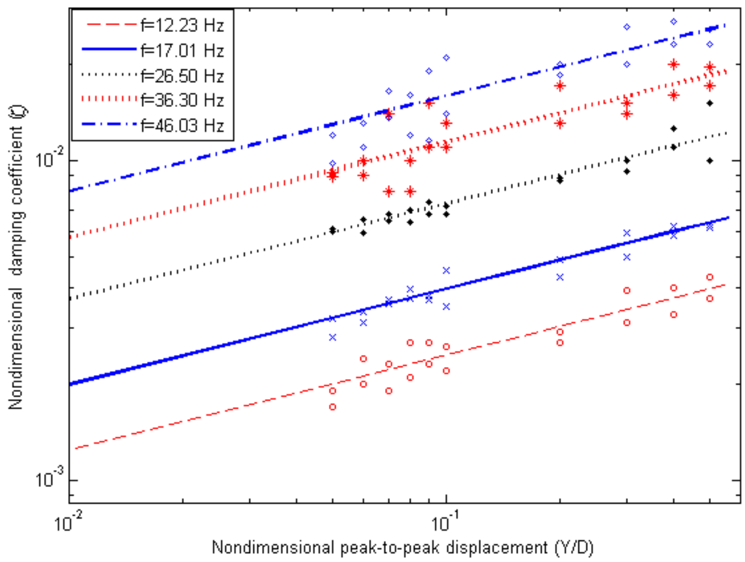

Figure 2.13: Conductor damping constant for fixed frequency for T = 20% RTS.

for T= 10, 20, 25, and 40% RTS. However, because of company confidentiality agreement only the 20 and 25 % RTS data are presented and the results are shown in Figs. 2.13 to 2.16. It should be noted that measurements were repeated twice to minimize the effect of random error.

Figs. 2.13 and 2.14 show plots of the damping ratio against the non-dimensional peak-to-peak amplitude. At every resonant frequency, a line of best fit is plotted. Both figures indicate similar trends in that the damping ratio increases with increasing displacement. However, the damping ratio values in Fig. 2.13 (i.e., for T = 20% RTS) are higher than those in Fig. 2.14 (i.e., for T = 25% RTS). This implies that increasing the tension reduces the self-damping of the conductor.

For given displacement of $Y/D = 0.1$ and $Y/D = 0.3$, plots of damping ratio against resonant frequencies are depicted in Figs. 2.15 and 2.16 for T = 20% RTS and T = 25% RTS, respectively. These plots indicate that the conductor-self damping increase with increasing frequency and the figure with the lower tension (i.e. Fig. 2.15) exhibits higher conductor self-damping.

2.5 Summary

Two sets of experiments were conducted to determine the characteristics of the Stockbridge damper and the conductor. In the first set of experiments the Stockbridge damper

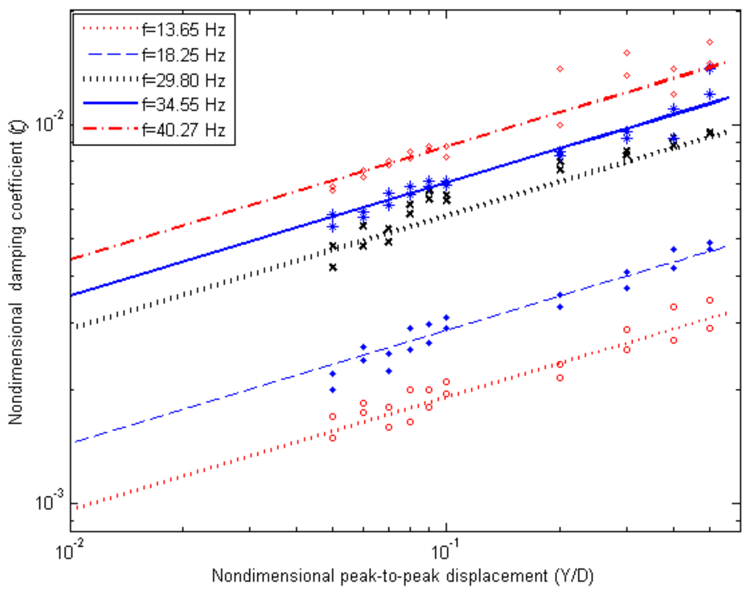

Figure 2.14: Conductor damping constant for fixed frequency for $T = 25\%$ RTS.

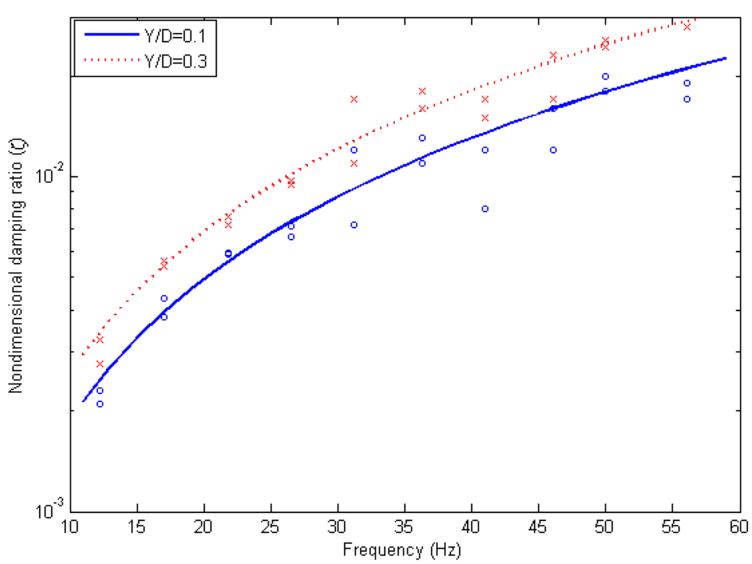

Figure 2.15: Conductor damping constant for a fixed vibration amplitude for $T = 20\%$ RTS.

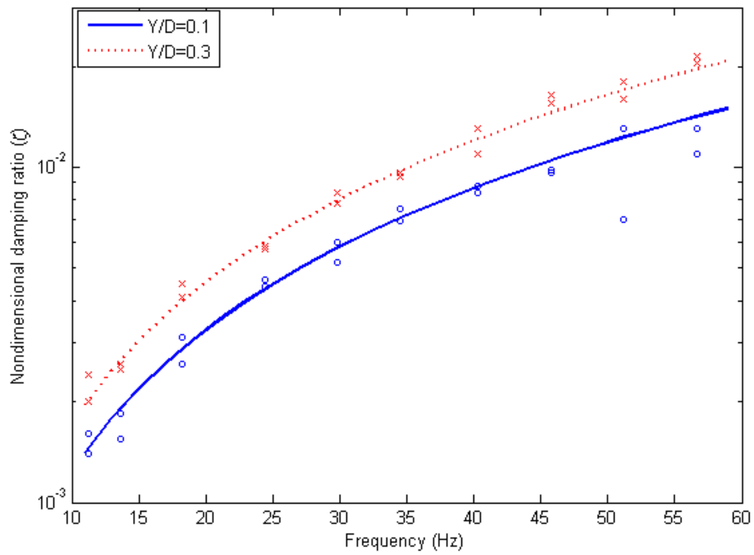

Figure 2.16: Conductor damping constant for fixed vibration amplitude for $T = 25\%$ RTS.

was mounted on the shaker and measurements were recorded for the excitation force, velocity, vibration frequency, and phase angle between the force and the velocity. These recorded data were used to obtain the damping coefficient of the Stockbridge damper. It was demonstrated that this damping coefficient is dependent on the excitation frequency. It was also observed that the tested Stockbridge damper possesses four resonant frequencies which confirm the physical nature of asymmetric Stockbridge damper.

In the second set of experiments, a conductor with and without a damper was strung between the concrete blocks and a shaker was placed at mid-span to excite the system. The natural frequency and the vibration response of the conductor with and without a damper were recorded. Linear regression analysis was used to determine an explicit expression for the damping ratio of the conductor. This damping ratio was found to be significantly dependent on the tension, excitation frequency and vibration amplitude.

Chapter 3

Single Beam/Lump Mass System

3.1 Introduction

This chapter discusses a novel model of a vibrating single-conductor transmission line carrying Stockbridge dampers in which the conductor is modeled as a beam subjected to a tensile load and the damper is reduced to an equivalent discrete mass-spring-mass and viscous damping system. Numerous researchers (see Refs. [50]-[78] and the references mentioned therein) have investigated the vibration of beams with an attached in-span mass and/or spring-mass system. In spite of these interests, there is no investigation where the beam is subjected to an axial load while supporting an in-span mass-spring-mass and viscous damping system.

A schematic of the transmission line system is depicted in Fig. 3.1. The equivalent mass and stiffness of the messenger are determined on the premise that the damper consisted of the two cantilevered beams with a tip mass as depicted in Fig. 3.2. The equivalent viscous damping is obtained through experiments using the forced response method (IEEE guide [45]) as described in the previous chapter.

The equations of motion are derived using Hamilton's principle. Explicit expressions are presented for the characteristic equation and mode shapes. The model is validated using both the numerical and experimental results in the literature. Parametric studies are conducted to investigate the effect of the magnitude and location of the damper on the natural frequency. The role of the Strouhal frequency on the vibration response is also examined. Some of the content in this chapter is published in [76].

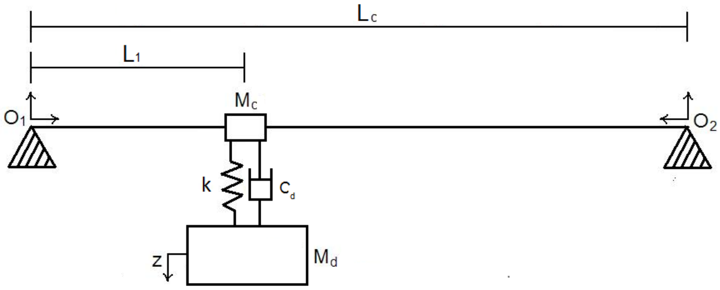

Figure 3.1: Schematic of a simply-supported beam with an in-span mass-spring-mass system.

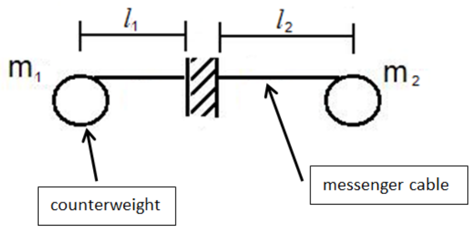

Figure 3.2: Schematic of Stockbridge damper messenger with counterweight.

3.2 Mathematical formulation

Following [30], the Stockbridge damper can be reduced to an equivalent mass-spring-mass and damper system. The equivalent spring stiffness and suspended mass are denoted by k and M_{d}, respectively.

$$k = 2\left(\frac{3E_{\mathrm{m}}I_{\mathrm{m}}}{L_{\mathrm{m}}^3}\right) \tag{3.1}$$

$$M_{\mathrm{d}} = \frac{33m_{\mathrm{m}}L_{\mathrm{m}}}{140} + m_1 + m_2 \tag{3.2}$$

where E_{m}, I_{m}, and m_{m} are the messenger elastic modulus, second moment of area, and mass per unit length, respectively. The masses of the right-hand side and left-hand side ends of the messenger are denoted by m_1 and m_2, respectively. The equivalent stiffness is the parallel combination of the stiffnesses of the two cantilevered beams, each with a tip mass.

The vertical displacements of the mass attached to the conductor M_{c} and the suspended mass M_{d} are denoted by $z_0(t)$ and $z(t)$, respectively. The system kinetic $\mathcal{T}$ and potential $\mathcal{V}$ energy may then be expressed as

$$\mathcal{T} = \sum_{\mathrm{i}=1}^{N} \left(\frac{1}{2} m_{\mathrm{c}} \int\limits_{L_{\mathrm{i}-1}}^{L_{\mathrm{i}}} \dot{w}_{\mathrm{i}}^{2}(x,t)dx + \frac{1}{2} M_{\mathrm{di}} \dot{z}_{\mathrm{i}}{}^{2} + \frac{1}{2} M_{\mathrm{ci}} \dot{z_{0\mathrm{i}}}{}^{2} \right) \tag{3.3}$$

$$\mathcal{V} = \sum_{\mathrm{i}=1}^{N} \left(\frac{1}{2} E_{\mathrm{c}} I_{\mathrm{c}} \int\limits_{L_{\mathrm{i}-1}}^{L_{\mathrm{i}}} w_{\mathrm{i}}''^{2}(x,t)dx + \frac{1}{2} c_{\mathrm{di}} (\dot{z}_{\mathrm{i}} - \dot{z_{0\mathrm{i}}})^{2} \right.$$
$$\left. + \frac{1}{2} k (z_{\mathrm{i}} - z_{0\mathrm{i}})^{2} + \frac{1}{2} T \int\limits_{L_{\mathrm{i}-1}}^{L_{\mathrm{i}}} w_{\mathrm{i}}'^{2}(x,t)dx \right) \tag{3.4}$$

where $z_0(t) = w_1(L_1, t)$, $E_{\mathrm{c}} I_{\mathrm{c}}$ is the conductor flexural rigidity, m_{c} is mass per unit length of the conductor, T denotes the conductor pretension. The overdots and primes denote temporal and spatial derivatives, respectively. The subscript "i" denotes the position of the mass-spring-damper-mass system and "N" is the total number of attached mass-spring-damper-mass systems.

These energies are introduced into the Hamilton's principle to obtain the equations of motion and continuity conditions

$$E_{\mathrm{c}} I_{\mathrm{c}} w_{\mathrm{i}}'''' + m_{\mathrm{c}} \ddot{w}_{\mathrm{i}} - T w_{\mathrm{i}}'' = 0 \tag{3.5}$$
$$M_{\mathrm{di}} \ddot{z} + k_{\mathrm{i}} (z_{\mathrm{i}} - z_{0\mathrm{i}}) + c_{\mathrm{d}} (\dot{z}_{\mathrm{i}} - \dot{z}_{0\mathrm{i}}) = 0 \tag{3.6}$$
$$w_1(0,t) = w_1''(0,t) = w_2(0,t) = w_2''(0,t) = 0 \tag{3.7}$$
$$w_{\mathrm{i}}(L_{\mathrm{i}}, t) = w_{\mathrm{i}+1}(L_{\mathrm{i}}, t) \tag{3.8}$$
$$w_{\mathrm{i}}'(L_{\mathrm{i}}, t) = w_{\mathrm{i}+1}'(L_{\mathrm{i}}, t) \tag{3.9}$$
$$w_{\mathrm{i}}''(L_{\mathrm{i}}, t) = w_{\mathrm{i}+1}''(L_{\mathrm{i}}, t) \tag{3.10}$$
$$-M_{\mathrm{c}} \ddot{z}_{0\mathrm{i}} + E_{\mathrm{c}} I_{\mathrm{c}} w_{\mathrm{i}}'''(L_{\mathrm{i}}, t) - T w_{\mathrm{i}}'(L_{\mathrm{i}}, t) - k(z_{0\mathrm{i}} - z_{\mathrm{i}}) - c_{\mathrm{d}} (\dot{z}_{0\mathrm{i}} - \dot{z}_{\mathrm{i}})$$
$$- E_{\mathrm{c}} I_{\mathrm{c}} w_{\mathrm{i}+1}'''(L_{\mathrm{i}}, t) + T w_{\mathrm{i}+1}'''(L_{\mathrm{i}}, t) = 0 \tag{3.11}$$

3.2.1 Frequency equation and mode shapes

Assuming the system exhibits harmonic vibration such that the deformations $w_{\mathrm{i}}(x_{\mathrm{i}}, t)$ and displacements $z(t)$ are expressed as

$$w_{\mathrm{i}}(x_{\mathrm{i}}, t) = L W_{\mathrm{i}}(\xi_{\mathrm{i}}) \mathrm{e}^{j\omega t} \qquad \text{for i} = 1, 2 \tag{3.12}$$
$$z_{\mathrm{i}}(t) = L A_{\mathrm{i}} \mathrm{e}^{j\omega t} \tag{3.13}$$

where $W_i(\xi_i)$ and A_i are the respective non-dimensional amplitudes of $w_i(x_i, t)$ and $z_i(t)$, and ω is the circular natural frequency of the system. Substituting Eqs. (3.12) and (3.13) into Eqs. (3.5)-(3.11) and ignoring the viscous damping component yield the following non-dimensional system equations

$$W_i''''(\xi_i) - s^2 W_i''(\xi_i) - \Omega^4 W_i \xi_i) = 0 \tag{3.14}$$

$$A_i - K_i W_i(\xi_i) = 0 \tag{3.15}$$

where

$$W_i(\xi_i) = c_{1i} \sin \alpha\xi_i + c_{2i} \cos \alpha\xi_i + c_{3i} \sinh \beta\xi_i + c_{4i} \cosh \beta\xi_i \tag{3.16}$$

Substituting Eqs. (3.12) and (3.13) into Eqs. (3.7)-(3.11) yields

$$W_1(0) = W_1''(0) = W_2(0) = W_2''(0) = 0 \tag{3.17}$$

$$W_i(\xi_i) = W_{i+1}(\xi_i) \tag{3.18}$$

$$W_i'(\xi_i) = W_{i+1}'(\xi_i) \tag{3.19}$$

$$W_i''(\xi_i) = W_{i+1}''(\xi_i) \tag{3.20}$$

$$W_i'''(\xi_i) - W_{i+1}'''(\xi_i) - \eta_i W_i(\xi_i) + \gamma_i A_i = 0 \tag{3.21}$$

where the following nondimensional variables are used

$$A_i = K W_i(\xi_i), \quad K_i = \frac{k_i}{k_i - M_{di}\omega^2}, \quad s^2 = \frac{TL^2}{E_c I_c}, \tag{3.22}$$

$$\Omega^4 = \frac{m_c \omega^2}{E_c I_c} L^4, \quad \eta_i = \frac{k_i - \omega^2 M_{ci}}{E_c I_c} L^3, \quad \gamma_i = \frac{k_i L^3}{E_c I_c} \text{ and } \quad \xi_i = \frac{x_i}{L} \tag{3.23}$$

Substituting Eq. (3.15) into Eq. (3.21) yields

$$W_i'''(\xi_i) - W_{i+1}'''(\xi_i) + W_i(\xi_i)(K_i\gamma_i - \eta_i) = 0 \tag{3.24}$$

The use of the classical boundary conditions at each end, Eqs. (3.17), along with Eqs. (3.18)-(3.20) and Eq. (3.24) yields a set of 4+4N algebraic homogeneous equations (4 equations from the boundary condition at the ends and 4N equations from the continuity relations). These algebraic equations are linear in the unknown coefficients (C's) and they can be presented in matrix format as

$$[\mathcal{F}]_{(4+4N)X(4+4N)} \{C\}_{(4+4N)X(1)} = \{0\}_{(4+4N)X(1)} \tag{3.25}$$

For the sake of simplicity, the following notations are introduced

$$
\begin{aligned}
s_{\alpha} &= \sin\alpha, & c_{\alpha} &= \cos\alpha \\
sh_{\beta} &= \sinh\beta, & ch_{\beta} &= \cosh\beta \\
s_{\alpha i} &= \sin\alpha(\xi_i), & c_{\alpha i} &= \cos\alpha(\xi_i), \\
sh_{\beta i} &= \sinh\beta(\xi_i), & ch_{\beta i} &= \cosh\beta(\xi_i), \\
\epsilon &= K_1\gamma_1 - \eta_1. & &
\end{aligned}
$$

The elements of the matrix $\mathcal{F}$ are expressed as

$$
\begin{aligned}
\mathcal{F}_{(4\mathrm{i}-1,4\mathrm{i}-3)} &= s_{\alpha\mathrm{i}} & \mathcal{F}_{(4\mathrm{i}-1,4\mathrm{i}-2)} &= c_{\alpha\mathrm{i}} \\
\mathcal{F}_{(4\mathrm{i}-1,4\mathrm{i}-1)} &= sh_{\beta\mathrm{i}} & \mathcal{F}_{(4\mathrm{i}-1,4\mathrm{i})} &= ch_{\beta\mathrm{i}} \\
\mathcal{F}_{(4\mathrm{i}-1,4\mathrm{i}+1)} &= -s_{\alpha\mathrm{i}} & \mathcal{F}_{(4\mathrm{i}-1,4\mathrm{i}+2)} &= -c_{\alpha\mathrm{i}} \\
\mathcal{F}_{(4\mathrm{i}-1,4\mathrm{i}+3)} &= -sh_{\beta\mathrm{i}} & \mathcal{F}_{(4\mathrm{i}-1,4\mathrm{i}+4)} &= -ch_{\beta\mathrm{i}}
\end{aligned}
$$

$$
\begin{aligned}
\mathcal{F}_{(4\mathrm{i},4\mathrm{i}-3)} &= \alpha c_{\alpha\mathrm{i}} & \mathcal{F}_{(4\mathrm{i},4\mathrm{i}-2)} &= -\alpha s_{\alpha\mathrm{i}} \\
\mathcal{F}_{(4\mathrm{i},4\mathrm{i}-1)} &= \beta ch_{\beta\mathrm{i}} & \mathcal{F}_{(4\mathrm{i},4\mathrm{i})} &= \beta sh_{\beta\mathrm{i}} \\
\mathcal{F}_{(4\mathrm{i},4\mathrm{i}+1)} &= -\alpha c_{\alpha\mathrm{i}} & \mathcal{F}_{(4\mathrm{i},4\mathrm{i}+2)} &= \alpha s_{\alpha\mathrm{i}} \\
\mathcal{F}_{(4\mathrm{i},4\mathrm{i}+3)} &= -\beta ch_{\beta\mathrm{i}} & \mathcal{F}_{(4\mathrm{i},4\mathrm{i}+4)} &= -\beta sh_{\beta\mathrm{i}}
\end{aligned}
$$

$$
\begin{aligned}
\mathcal{F}_{(4\mathrm{i}+1,4\mathrm{i}-3)} &= \alpha^2 s_{\alpha\mathrm{i}} & \mathcal{F}_{(4\mathrm{i}+1,4\mathrm{i}-2)} &= -\alpha^2 c_{\alpha\mathrm{i}} \\
\mathcal{F}_{(4\mathrm{i}+1,4\mathrm{i}-1)} &= \beta^2 sh_{\beta\mathrm{i}} & \mathcal{F}_{(4\mathrm{i}+1,4\mathrm{i})} &= \beta^2 ch_{\beta\mathrm{i}} \\
\mathcal{F}_{(4\mathrm{i}+1,4\mathrm{i}+1)} &= \alpha^2 s_{\alpha\mathrm{i}} & \mathcal{F}_{(4\mathrm{i}+1,4\mathrm{i}+2)} &= \alpha^2 c_{\alpha\mathrm{i}} \\
\mathcal{F}_{(4\mathrm{i}+1,4\mathrm{i}+3)} &= -\beta^2 sh_{\beta\mathrm{i}} & \mathcal{F}_{(4\mathrm{i}+1,4\mathrm{i}+4)} &= -\beta^2 ch_{\beta\mathrm{i}}
\end{aligned}
$$

$$
\begin{aligned}
\mathcal{F}_{(4\mathrm{i}+2,4\mathrm{i}-3)} &= -\alpha^3 c_{\alpha i} + \epsilon s_{\alpha i} & \mathcal{F}_{(4\mathrm{i}+2,4\mathrm{i}-2)} &= \alpha^3 s_{\alpha i} + \epsilon c_{\alpha i} \\
\mathcal{F}_{(4\mathrm{i}+2,4\mathrm{i}-1)} &= \beta^3 ch_{\beta i} + \epsilon sh_{\beta i} & \mathcal{F}_{(4\mathrm{i}+2,4\mathrm{i})} &= \beta^3 sh_{\beta i} + \epsilon ch_{\beta i} \\
\mathcal{F}_{(4\mathrm{i}+2,4\mathrm{i}+1)} &= \alpha^3 c_{\alpha i} & \mathcal{F}_{(4\mathrm{i}+2,4\mathrm{i}+2)} &= -\alpha^3 s_{\alpha i} \\
\mathcal{F}_{(4\mathrm{i}+2,4\mathrm{i}+3)} &= -\beta^3 ch_{\beta i} & \mathcal{F}_{(4\mathrm{i}+2,4\mathrm{i}+4)} &= -\beta^3 sh_{\beta i}
\end{aligned}
$$

$\mathcal{F}_{(1,1)}, \mathcal{F}_{(1,2)}, \mathcal{F}_{(1,3)}, \mathcal{F}_{(1,4)}, \mathcal{F}_{(2,1)}, \mathcal{F}_{(2,2)}, \mathcal{F}_{(2,3)}, \mathcal{F}_{(2,4)}$ depends on the boundary conditions at the origin $x = 0$. $\mathcal{F}_{(\mathrm{q}-1,\mathrm{p}+1)}, \mathcal{F}_{(\mathrm{q}-1,\mathrm{p}+2)}, \mathcal{F}_{(\mathrm{q}-1,\mathrm{p}+3)}, \mathcal{F}_{(\mathrm{q}-1,\mathrm{p}+4)}, \mathcal{F}_{(\mathrm{q},\mathrm{p}+1)}, \mathcal{F}_{(\mathrm{q},\mathrm{p}+2)}, \mathcal{F}_{(\mathrm{q},\mathrm{p}+3)}, \mathcal{F}_{(\mathrm{q},\mathrm{p}+4)}$

are obtained from the boundary conditions at $x = \mathrm{L}$, where $q = 4N + 4$ and $p = 4N$.

A non-trivial solution is obtained when matrix $\mathcal{F}$ is singular. Hence, the characteristic or frequency equation is obtained as

$$det([\mathcal{F}]_{(4+4\mathrm{N})\mathrm{X}(4+4\mathrm{N})}) = 0 \tag{3.26}$$

For a single conductor with one damper the frequency equation is expressed as

$$\begin{aligned}
&(k - \omega^2 M_{\mathrm{d}})(-\beta\eta\alpha^2 c_{\alpha\theta} sh_\beta + \alpha\eta\beta^2 s_\alpha ch_\beta \\
&- \alpha\eta\beta^2 s_\alpha ch_{\beta\theta} - \alpha\beta^2\gamma K s_\alpha ch_\beta + \alpha\beta^2\gamma K s_\alpha ch_{\beta\theta} \\
&+ \beta\eta\alpha^2 c_\alpha sh_\beta - \beta\gamma K\alpha^2 c_\alpha sh_\beta - \alpha^3\gamma K s_\alpha ch_\beta \\
&+ \alpha^3\gamma K s_\alpha ch_{\beta\theta} - \beta^3\gamma K c_\alpha sh_\beta + \beta^3\eta c_\alpha sh_\beta \\
&- 2\alpha\beta^5 s_\alpha sh_\beta - 2\alpha^5\beta s_\alpha sh_\beta - \beta^3\eta c_{\alpha\theta} sh_\beta \\
&- 4\alpha^3\beta^3 s_\alpha sh_\beta + \alpha^3\eta s_\alpha ch_\beta - \alpha^3\eta s_\alpha ch_{\beta\theta} \\
&+ \beta\gamma K\alpha^2 c_{\alpha\theta} sh_\beta + \beta^3\gamma K c_{\alpha\theta} sh_\beta) = 0
\end{aligned} \tag{3.27}$$

where

$$\begin{aligned}
\phi &= c_{\alpha 1}\alpha^3 + s_1(\eta - \gamma K) \\
\epsilon &= -ch_{\beta 1}\beta^3 + sh_{\beta 1}(\eta - \gamma K) \\
\kappa &= c_{\alpha 2}\alpha^3 \\
\chi &= -ch_{\beta 2}\beta^3 \\
c_{\alpha\theta} &= \cos(\alpha\{\xi_1 - \xi_2\}) \\
ch_{\beta\alpha} &= \cosh(\beta\{\xi_1 - \xi_2\})
\end{aligned}$$

The characteristic equation is multiplicatively decomposed into a component that yielded the natural frequency of the suspended simple discrete spring-mass system and another that provided the frequency of the more complex system.

The mode shapes associated with each beam segment is obtained by substituting the integration constants from Eq. (3.25) into Eq. (3.16). For a single conductor with one damper, the shape functions can be written as

$$W_1(\xi_1) = c_{11} \sin \alpha \xi_1 \tag{3.28}$$

$$W_2(\xi_2) = c_{11} \frac{s_1}{s_2} \sin \alpha \xi_2 \tag{3.29}$$

3.2.2 Orthogonality relations

The solution of the equations of motion, Eqs. (3.5) and (3.6), can be expressed as

$$w_{\mathrm{i}}(x,t) = Y_{\mathrm{i}}(x)^{(r)} e^{j\omega t} \tag{3.30}$$

$$z_{\mathrm{i}}(t) = Z_{\mathrm{i}}^{(r)} e^{j\omega t} \tag{3.31}$$

where

$$Y_{\mathrm{i}}(x) = LW_{\mathrm{i}}(\xi_{\mathrm{i}}) \tag{3.32}$$

$$Z_{\mathrm{i}}(t) = LA_{\mathrm{i}} \tag{3.33}$$

Substituting Eqs. (3.30) and (3.31) into Eq. (3.6) and multiplying the resulting equation by $\mathrm{Z}^{(s)}$ yields

$$-kZ_{\mathrm{i}}^{(r)}Z_{\mathrm{i}}^{(s)} + M_{\mathrm{d}}\omega_{\mathrm{r}}^2 Z_{\mathrm{i}}^{(r)}Z_{\mathrm{i}}^{(s)} - j\omega_{\mathrm{r}}c_{\mathrm{d}}Z_{\mathrm{i}}^{(r)}Z_{\mathrm{i}}^{(s)} = -Y_{\mathrm{i}}^{*(r)}Z_{\mathrm{i}}^{(s)}\left(k + j\omega_{\mathrm{r}}c_{\mathrm{d}}\right) \tag{3.34}$$

Interchanging "r" and "s" in Eq. (3.34) and subtracting the resulting equation from Eq. (3.34) yields

$$\begin{aligned}\left(\omega_{\mathrm{r}}^2 - \omega_{\mathrm{s}}^2\right) M_{\mathrm{d}} Z_{\mathrm{i}}^{(r)}Z_{\mathrm{i}}^{(s)} - jc_{\mathrm{d}}(\omega_{\mathrm{r}} - \omega_{\mathrm{s}})Z_{\mathrm{i}}^{(r)}Z_{\mathrm{i}}^{(s)} &= -k\left(Y_{\mathrm{i}}^{*(r)}Z_{\mathrm{i}}^{(s)} - Y_{\mathrm{i}}^{*(s)}Z_{\mathrm{i}}^{(r)}\right) \\ &\quad jc_{\mathrm{d}}\left(\omega_{\mathrm{r}}Y_{\mathrm{i}}^{*(r)}Z_{\mathrm{i}}^{(s)} - \omega_{\mathrm{s}}Y_{\mathrm{i}}^{*(s)}Z_{\mathrm{i}}^{(r)}\right)\end{aligned} \tag{3.35}$$

With reference to the equations of motion of the beam, substituting Eqs. (3.30) and (3.31) into Eq. (3.5), then multiplying the resulting equation by $\mathrm{Y}^{(s)}$ and integrating over the entire length of the beam, as well as applying the continuity conditions, Eqs. (3.18)-

(3.21), with any classical boundary conditions except those for free ends yields

$$\omega_{\mathrm{r}}^{2}\sum_{i=1}^{N}\left(m_{\mathrm{c}}\int_{0}^{L_{\mathrm{i}}}Y_{\mathrm{i}}^{(r)}Y_{\mathrm{i}}^{(s)}dx+M_{\mathrm{c}}Y_{\mathrm{i}}^{*(r)}Y_{\mathrm{i}}^{*(s)}\right)-jc_{\mathrm{d}}\omega_{\mathrm{r}}\sum_{i=1}^{N}Y_{\mathrm{i}}^{*(r)}Y_{\mathrm{i}}^{*(s)}$$
$$=\sum_{i=1}^{N}\Bigg(E_{\mathrm{c}}I_{\mathrm{c}}\int_{0}^{L_{\mathrm{i}}}Y_{\mathrm{i}}''^{(r)}Y_{\mathrm{i}}''^{(s)}dx+T\int_{0}^{L_{\mathrm{i}}}Y_{\mathrm{i}}'^{(r)}Y_{\mathrm{i}}'^{(s)}dx+kY_{\mathrm{i}}^{*(r)}Y_{\mathrm{i}}^{*(s)}-$$
$$kZ_{\mathrm{i}}^{(r)}Y_{\mathrm{i}}^{*(s)}-jc_{\mathrm{d}}\omega_{\mathrm{r}}Z_{\mathrm{i}}^{(r)}Y_{\mathrm{i}}^{*(s)}\Bigg) \tag{3.36}$$

Re-writing Eq. (3.36) and interchanging "r" and "s" yields

$$\omega_{\mathrm{s}}^{2}\sum_{i=1}^{N}\left(m_{\mathrm{c}}\int_{0}^{L_{\mathrm{i}}}Y_{\mathrm{i}}^{(s)}Y_{\mathrm{i}}^{(r)}dx+M_{\mathrm{c}}Y_{\mathrm{i}}^{*(s)}Y_{\mathrm{i}}^{*(r)}\right)-jc_{\mathrm{d}}\omega_{\mathrm{s}}\sum_{i=1}^{N}Y_{\mathrm{i}}^{*(s)}Y_{\mathrm{i}}^{*(r)}$$
$$=\sum_{i=1}^{N}\Bigg(E_{\mathrm{c}}I_{\mathrm{c}}\int_{0}^{L_{\mathrm{i}}}Y_{\mathrm{i}}''^{(s)}Y_{\mathrm{i}}''^{(r)}dx+T\int_{0}^{L_{\mathrm{i}}}Y_{\mathrm{i}}'^{(s)}Y_{\mathrm{i}}'^{(r)}dx+kY_{\mathrm{i}}^{*(r)}Y_{\mathrm{i}}^{*(s)}-$$
$$kZ_{\mathrm{i}}^{(s)}Y_{\mathrm{i}}^{*(r)}-jc_{\mathrm{d}}\omega_{\mathrm{s}}Z_{\mathrm{i}}^{(s)}Y_{\mathrm{i}}^{*(r)}\Bigg) \tag{3.37}$$

Subtracting Eq. (3.37) from Eq. (3.36) and substituting Eq. (3.35) into the resulting equation yields

$$\left(\omega_{\mathrm{r}}^{2}-\omega_{\mathrm{s}}^{2}\right)\sum_{i=1}^{N}\left(m_{\mathrm{c}}\int_{0}^{L_{\mathrm{i}}}Y_{\mathrm{i}}^{(r)}Y_{\mathrm{i}}^{(s)}dx+M_{\mathrm{c}}Y_{\mathrm{i}}^{*(r)}Y_{\mathrm{i}}^{*(s)}+M_{\mathrm{d}}Z_{\mathrm{i}}^{(r)}Z_{\mathrm{i}}^{(s)}\right)$$
$$-jc_{\mathrm{d}}\left(\omega_{\mathrm{r}}-\omega_{\mathrm{s}}\right)\left(Y_{\mathrm{i}}^{*(r)}Y_{\mathrm{i}}^{*(s)}+Z_{\mathrm{i}}^{(r)}Z_{\mathrm{i}}^{(s)}\right)=0 \tag{3.38}$$

From Eq. (3.38), the first set of orthogonality relation is obtained as

$$\sum_{i=1}^{N}\left(m_{\mathrm{c}}\int_{0}^{L_{\mathrm{i}}}Y_{\mathrm{i}}^{(r)}Y_{\mathrm{i}}^{(s)}dx+M_{\mathrm{c}}Y_{\mathrm{i}}^{*(r)}Y_{\mathrm{i}}^{*(s)}+M_{\mathrm{d}}Z_{\mathrm{i}}^{(r)}Z_{\mathrm{i}}^{(s)}\right)=\delta_{\mathrm{rs}} \tag{3.39}$$

where δ_{rs} is the Kronecker delta. The second set of orthogonality relation is expressed as

$$\sum_{i=1}^{N}\left(Y_{\mathrm{i}}^{*(r)}Y_{\mathrm{i}}^{*(s)}+Z_{\mathrm{i}}^{(r)}Z_{\mathrm{i}}^{(s)}\right)=\delta_{\mathrm{rs}} \tag{3.40}$$

The use of Eqs. (3.34) and (3.37) with the aid of some algebraic manipulation yields the third and fourth set of orthogonality relation. This may be written as

$$\sum_{i=1}^{N} E_c I_c \int_0^{L_i} Y_i''^{(r)} Y_i''^{(s)} dx + T \int_0^{L_i} Y_i'^{(r)} Y_i'^{(s)} dx \\ + k\left(Y_i^{*(r)} Y_i^{*(s)} - Z_i^{(s)} Y_i^{*(r)} - Z_i^{(r)} Y_i^{*(s)} + Z_i^{(r)} Z_i^{(s)}\right) = \delta_{rs} \tag{3.41}$$

$$\sum_{i=1}^{N} \left(Y_i^{*(r)} Z_i^{*(s)} + Z_i^{(r)} Y_i^{(s)}\right) = \delta_{rs} \tag{3.42}$$

3.2.3 Forced vibration formulation

Given that the validation of the forced response was based on the experiment reported in Ref. [32], the excitation force was from the mid-span located electrodynamic shaker. This force can be expressed as $F(x,t) = f(t)\delta(x - L_c/2)$, and the forced-vibration equations may be written as

$$m_c \ddot{w}_i + E_c I_c w''''_i - T w''_i = F(x,t)\delta\left(x - 0.5\right) \tag{3.43}$$

$$M_{di} \ddot{z}_i + k_i \left(z_i - w_i(L_i)\right) + c_{di}\left(\dot{z}_i - \dot{w}_i(L_i)\right) = 0 \tag{3.44}$$

Using the assumed mode method, the transverse displacement of the beam and the displacement of vibration absorber may be expressed as

$$w_i = \sum_{r=1}^{N_r} q_r(t) Y_i^{(r)}(x) \tag{3.45}$$

$$z_i = \sum_{r=1}^{N_r} q_r(t) Z_i^{(r)}(x) \tag{3.46}$$

where N_r is the number of retained modes, $Y_i^{(r)}(x)$ is the mode shape corresponding to the r^{th} mode, $Z_i^{(r)}$ is the displacement amplitude of the absorber, and $q_r(t)$ is the r^{th} generalized coordinate. Substituting Eqs. (3.45) and (3.46) into Eqs. (3.43) and (3.44), respectively yield

$$m_c \sum_{r=1}^{N_r} \ddot{q}_r Y_i^{(r)} + E_c I_c \sum_{r=1}^{N_r} q_r Y_i''''^{(r)} - T \sum_{r=1}^{N_r} q_r Y_i''^{(r)} = F(t)\delta\left(x - 0.5\right) \tag{3.47}$$

$$M_{di} \sum_{r=1}^{N_r} \ddot{q}_r Y_{mi}^{(r)} + k_i \sum_{r=1}^{N_r} q_r \left(Z_i^{(r)} - Y_{ci}^{(r)}(L_i)\right) + c_{di} \sum_{r=1}^{N_r} \dot{q}_r \left(Z_i^{(r)} - Y_{ci}^{(r)}(L_i)\right) = 0 \tag{3.48}$$

Multiplying Eqs. (3.47) and (3.48) by $Y_{\mathrm{i}}^{(s)}$ and $Z_{\mathrm{i}}^{(s)}$, respectively, adding the two resulting equations, integrating over the entire length of the beam, and applying the continuity conditions, Eqs. (3.18)-(3.21), with any classical boundary condition (except for free ends) yield

$$\begin{aligned}
&\sum_{r=1}^{N_r} \ddot{q}_{\mathrm{r}} \left\{ m_{\mathrm{c}} \int_0^{L_{\mathrm{i}}} Y_{\mathrm{i}}^{(r)} Y_{\mathrm{i}}^{(s)} dx + M_{\mathrm{ci}} Y_{\mathrm{i}}^{*(r)} Y_{\mathrm{i}}^{*(s)} + M_{\mathrm{di}} Z_{\mathrm{i}}^{(r)} Z_{\mathrm{i}}^{(s)} \right\} \\
&\quad + c_{\mathrm{di}} \sum_{r=1}^{N_r} \dot{q}_{\mathrm{r}} \left\{ Y_{\mathrm{i}}^{*(r)} Y_{\mathrm{i}}^{*(s)} - Z_{\mathrm{i}}^{(s)} Y_{\mathrm{i}}^{*(r)} - Z_{\mathrm{i}}^{(r)} Y_{\mathrm{i}}^{*(s)} + Z_{\mathrm{i}}^{(r)} Z_{\mathrm{i}}^{(s)} \right\} \\
&\quad + \sum_{r=1}^{N_r} q_{\mathrm{r}} \left\{ \int_0^{L_{\mathrm{i}}} \left(E_{\mathrm{c}} I_{\mathrm{c}}\ Y_{\mathrm{i}}''^{(r)} Y_{\mathrm{i}}''^{(s)} + T\ Y_{\mathrm{i}}'^{(r)} Y_{\mathrm{i}}'^{(s)} \right) dx \right. \\
&\quad \left. + k_{\mathrm{i}} \left(Y_{\mathrm{i}}^{*(r)} Y_{\mathrm{i}}^{*(s)} - Z_{\mathrm{i}}^{(s)} Y_{\mathrm{i}}^{*(r)} - Z_{\mathrm{i}}^{(r)} Y_{\mathrm{i}}^{*(s)} + Z_{\mathrm{i}}^{(r)} Z_{\mathrm{i}}^{(s)} \right) \right\} \\
&\quad = F(x,t) Y_{\mathrm{i}}^{(s)}(0.5) \qquad (3.49)
\end{aligned}$$

Use of the orthogonality relations, Eqs. (3.39)-(3.42), yields the following uncoupled differential equation

$$[M_{\mathrm{rr}}]\{\ddot{q}_{\mathrm{r}}\} + [C_{\mathrm{rr}}]\{\dot{q}_{\mathrm{r}}\} + [K_{\mathrm{rr}}]\{q_{\mathrm{r}}\} = \{F_{\mathrm{r}}\} \qquad (3.50)$$

where the matrices M_{rr}, C_{r}, and K_{rr} are expressed as

$$M_{\mathrm{rr}} = \sum_{i=1}^{N} \left(m_{\mathrm{c}} \int_0^{L_{\mathrm{i}}} Y_{\mathrm{i}}^{(r)^2} dx + M_{\mathrm{ci}} Y_{\mathrm{i}}^{*(r)^2} + M_{\mathrm{di}} Z_{\mathrm{i}}^{(r)^2} \right) \qquad (3.51)$$

$$C_{\mathrm{rr}} = \sum_{i=1}^{N} c_{\mathrm{di}} \left(Y_{\mathrm{i}}^{*(r)} - Z_{\mathrm{i}}^{(r)} \right)^2 \qquad (3.52)$$

$$\begin{aligned}
K_{\mathrm{r}} &= \sum_{i=1}^{N} \left\{ \int_0^{L_{\mathrm{i}}} \left(E_{\mathrm{c}} I_{\mathrm{c}}\ Y_{\mathrm{i}}''^{(r)^2} + T\ Y_{\mathrm{i}}'^{(r)^2} \right) dx \right. \qquad (3.53) \\
&\quad \left. + k_{\mathrm{i}} \left(Y_{\mathrm{i}}^{*(r)} - Z_{\mathrm{i}}^{(r)} \right)^2 \right\}
\end{aligned}$$

$$F_{\mathrm{r}} = F(x,t) Y_{\mathrm{i}}^{(r)}(0.5) \qquad (3.54)$$

The amplitude of the damper can be readily expressed as

$$Z_{\mathrm{i}}^{(r)} = \kappa_{\mathrm{i}} Y_{\mathrm{i}}^{*(r)} \qquad (3.55)$$

where

$$\kappa_{\mathrm{i}} = \left(\frac{1 + (2\varsigma_{\mathrm{i}} r_{\mathrm{i}})^2}{(1 - r_{\mathrm{i}}^2)^2 + (2\varsigma_{\mathrm{i}} r_{\mathrm{i}})^2} \right)^{1/2}, \qquad \varsigma_{\mathrm{i}} = \frac{c_{\mathrm{di}}}{2M_{\mathrm{di}}\omega_{\mathrm{si}}},$$

$$r_{\mathrm{i}} = \frac{\Omega}{\omega_{\mathrm{si}}}, \qquad \omega_{\mathrm{si}} = \sqrt{\frac{k_{\mathrm{i}}}{M_{\mathrm{di}}}}.$$

3.3 Discussion

3.3.1 Free vibration analysis

The free vibration analyses are based on a 795-KCMIL-DRAKE-ACSR conductor with the following parameters: conductor diameter $d = 28.1$ mm, flexural rigidity $E_{\mathrm{c}}I_{\mathrm{c}} = 1602$ N/m, mass per unit length $m_{\mathrm{c}} = 1.6286$ kg/m, and the tension $T = 27840$ N. The characteristics of the Stockbridge damper are as follows: the flexural rigidity is $E_{\mathrm{m}}I_{\mathrm{m}} = 31.8$ Nm^2 and mass per unit length is $m_{\mathrm{m}} = 0.25$ kg/m. The mass of the right and left counterweights are $m_1 = 3.4$ kg and $m_2 = 1.46$ kg. The length of the messenger on the right and left are $l_1 = 0.3$ m and $l_2 = 0.22$ m. The parameters of the equivalent reduced model are: suspended mass $M_{\mathrm{d}} = 4.83$ kg, clamp mass $M_{\mathrm{c}} = 0.2$ kg and equivalent spring stiffness $k = 1356.96$ N/m.

The first ten natural frequencies are tabulated in Table 3.1. The results in the second column are obtained using Eq. (3.27), the frequency equation. The entries in the third column are the results obtained via a finite element (FE) implementation of the conductor and mass-spring-mass model. A good agreement is observed between the values of the exact solution and the FE method. This observation is true for the results by Barry et al. [2] and [42], which are presented in the fourth column. The second natural frequency is not captured in Refs. [2] and [42]. This frequency, 16.5798 rad/s, is in close proximity to that of the suspended spring-mass system (i.e., $\omega = \sqrt{\frac{k}{M_{\mathrm{d}}}} \approx 16.7603$ rad/s), and its absence may be explained by their formulation method. The damper employed in Refs. [2] and [42] is modelled as a system comprising two independent beams that are cantilevered to a rigid link which is connected to the conductor. Each cantilevered beam models a segment of the messenger and carries a tip mass which representes the counterweight.

A plot of the mode shapes corresponding to the lowest five mode shapes of the system is depicted in Fig. 3.3. Except for the second mode shape, these mode shapes can be related to the mode shapes of the bare beam. As observed earlier, the second mode frequency is in the proximity of the natural frequency of the suspended spring-mass

Table 3.1: The first ten natural frequencies obtained using various methods for conductor in-span mass $M_c = 0.2$ kg, $L = 27.25$ m and damper location $\xi_1 = 0.05$.

Mode	Natural frequency (rad/s)			
	Present	FEM (Beam-mass-spring-damper)	FEM (Double- beam) Ref.[2]	Bare beam
1	14.9825	14.9825	15.0679	15.0866
2	16.5774	16.5798	-	30.2077
3	30.2624	30.2624	30.0462	45.3978
4	45.4512	45.4512	44.7763	60.6911
5	60.7353	60.7354	58.9636	76.1214
6	76.1411	76.1412	72.3839	91.7220
7	91.6983	91.6986	85.6873	107.5255
8	107.4380	107.4389	99.9189	123.5638
9	123.3925	123.3948	115.1862	139.8682
10	139.5951	139.6002	131.1940	156.4688

system. It is conjectured that the inertia/mass of the damper effectively divides the conductor into two segments.

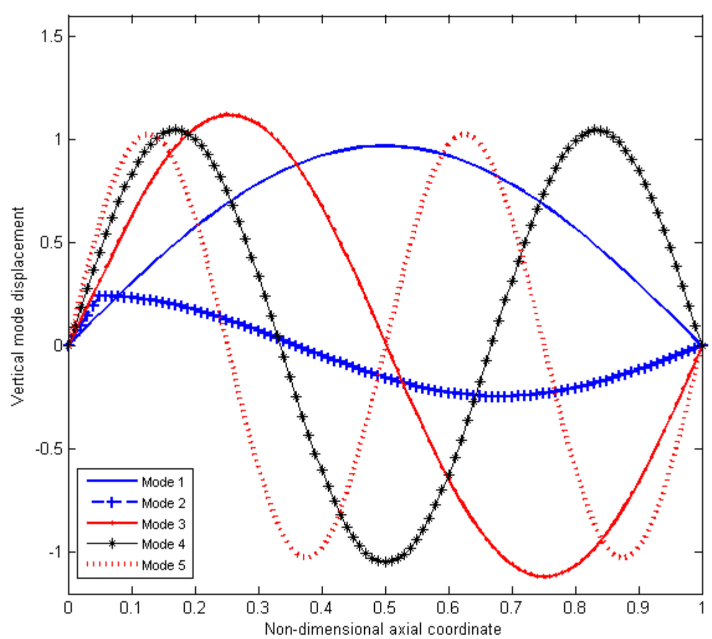

Figure 3.3: The mode shapes corresponding to the lowest five natural frequency of the conductor with mass-spring-mass system.

The influences of the relative magnitudes of the in-span mass M_c and the suspended mass M_d on the system natural frequencies are examined by maintaining their total sum constant — in the reported simulation $M_c + M_d = 5$ kg. The results are tabulated in Table 3.2. Using the scenario where the two masses are equal as a reference, it is observed that increasing the in-span mass M_c (and simultaneously decreasing the suspended mass M_d in order to maintain the constant total mass condition) increases the system natural frequencies of all five modes. This is plausible because increasing the in-span mass effectively increases the system stiffness (via the segmentation).

Table 3.2: The lowest five natural frequencies when the span length $L = 200$ m, in-span mass-spring-mass system is located at $\xi_1 = 0.0333$, and the magnitudes of the in-span mass M_c and suspended mass M_d are selected such that their sum $M_c + M_d = 5$ kg.

Mass (kg)	Natural frequency (rad/s)				
M_c, M_d	ω_1	ω_2	ω_3	ω_4	ω_5
$0, 5$	2.0544	4.1067	6.1537	8.1899	10.2016
$1, 4$	2.0544	4.1067	6.1543	8.1930	10.2153
$2, 3$	2.0544	4.1068	6.1547	8.1953	10.2239
$2.5, 2.5$	2.0544	4.1068	6.1549	8.1961	10.2268
$3, 2$	2.0544	4.1068	6.1551	8.1967	10.2290
$4, 1$	2.0544	4.1068	6.1552	8.1975	10.2317
$5, 0$	2.0544	4.1068	6.1553	8.1978	10.2325

To further examine the effects of the in-span and suspended masses on the system natural frequencies, both masses are varied from 0 to 5 kg. The first five natural frequencies are respectively depicted in Figs. 3.4 to 3.8. For a given in-span mass, the natural frequency decreases with increasing suspended mass. An identical, but less pronounced, effect is observed when the suspended mass is fixed while increasing in-span mass.

Fig. 3.9 shows the effect of the damper location on the system natural frequencies. The frequency at each damper location is normalized with respect to the frequency corresponding to the damper location $\xi_1 = 0.004$. The normalizing frequencies are 2.0548, 4.1096, 6.1645, 8.2195 and 10.2746 rad/s, corresponding to modes 1 through 5, respectively. One half of the conductor length is plotted because of symmetry. The first mode decreases monotonically with decreasing distance of the damper from the conductor midpoint. This is because the effective stiffness of the system decreases as the damper location approaches the centre of the conductor. The other four modes are not uniquely affected in that they all decrease and increase depending on whether they are approaching a node or an antinode. The rate of change is more pronounced in the fifth frequency.

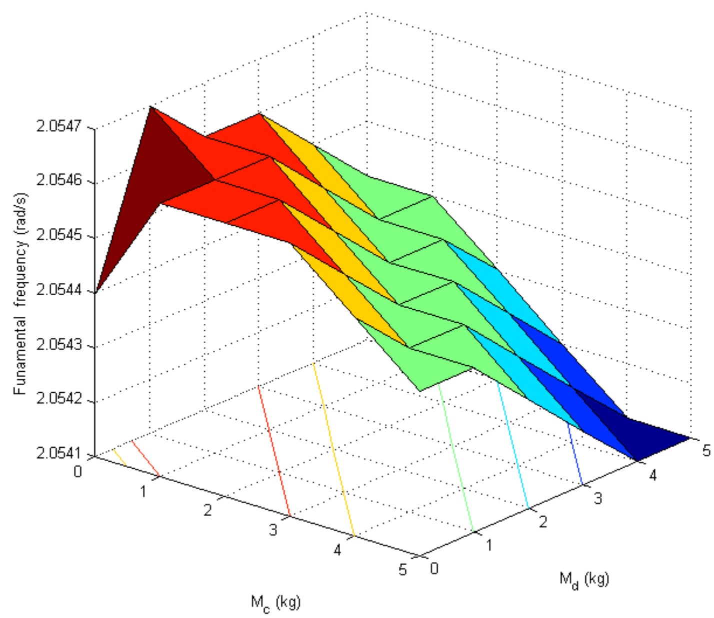

Figure 3.4: Effect of the mass M_{d} and M_{c} on the fundamental frequency.

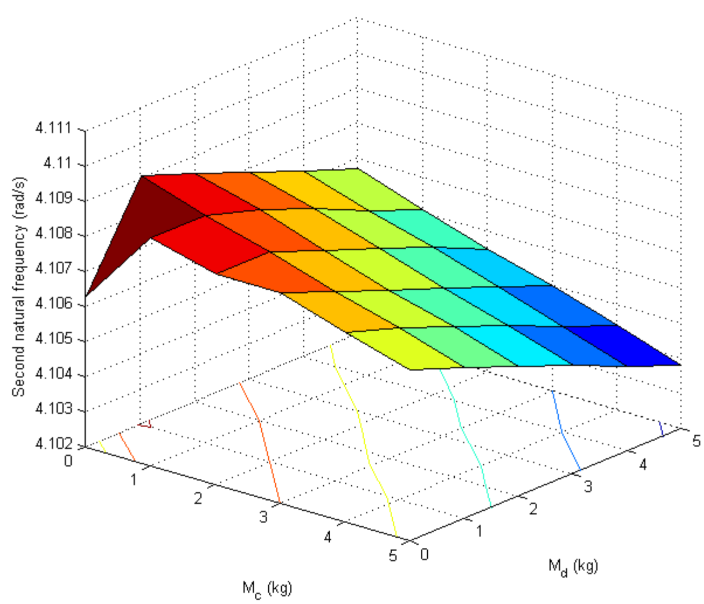

Figure 3.5: Effect of the mass M_{d} and M_{c} on the second natural frequency.

3.3.2 Forced vibration analysis

With regard to forced vibration analysis, the validation of the present model is examined in two-fold: the first employes the indoor experimental data reported in Ref. [32] and the

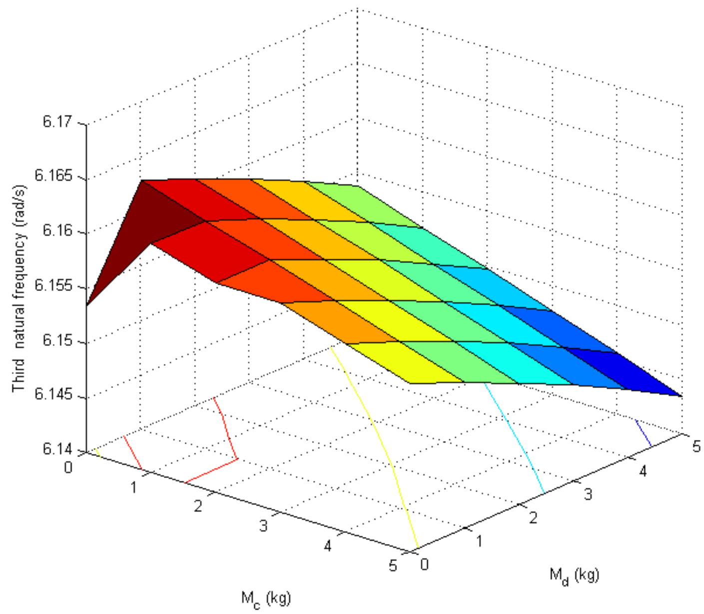

Figure 3.6: Effect of the mass M_d and M_c on the third natural frequency.

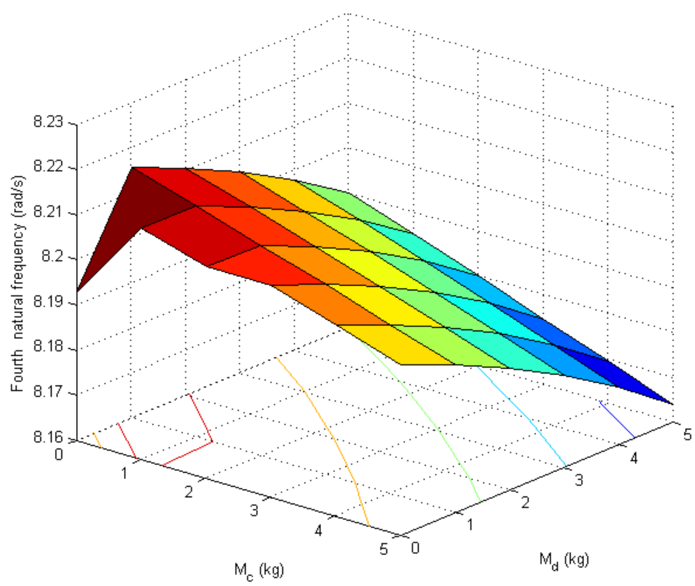

Figure 3.7: Effect of the mass M_d and M_c on the fourth natural frequency.

second relies on the finite element model of Ref. [2]. In the case of the indoor experiment, a 585 Kcmil (26/7) ASCR conductor was strung between two rigid terminals that were 23.5 m apart. Two identical dampers were attached at a distance of 1.73 m from each end and a shaker was mounted at mid-span. The shaker force and the mid-span velocity

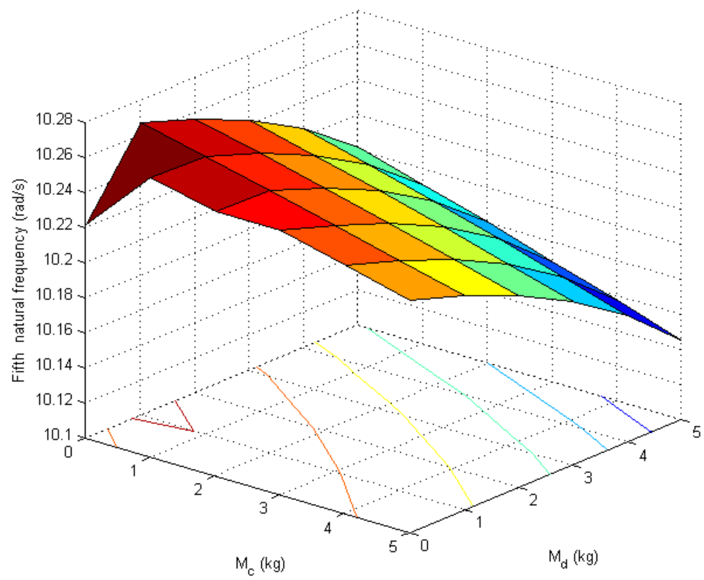

Figure 3.8: Effect of the mass M_{d} and M_{c} on the fifth natural frequency.

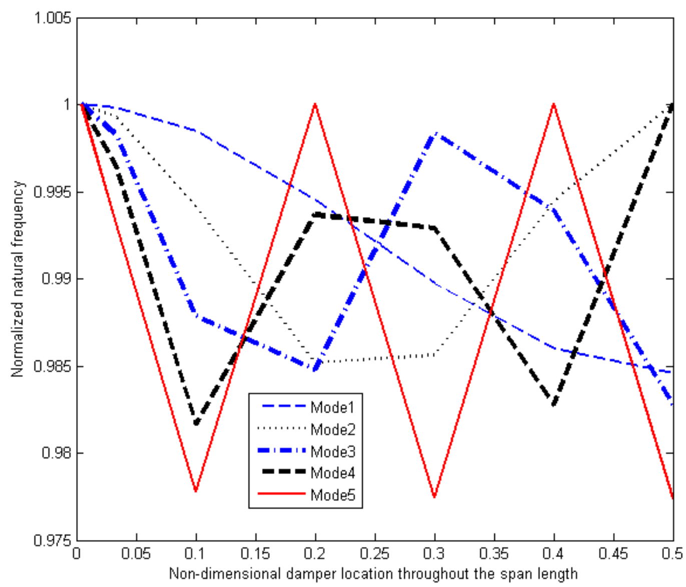

Figure 3.9: The effect of the damper location on natural frequencies for span length $L =$ 200 m. The frequencies are nondimensionalized as $\dfrac{\omega_i}{\omega_{\xi=0.004}}$.

of the conductor were measured for various resonant frequencies. The tested conductor had the following characteristics: diameter $D = 24.1$ m, mass per unit length $m = 1.19$ kg/m, rated tensile strength (RTS) of 105 kN. The tested damper was a single degree-of-freedom damper and it comprised a mass $M_{\mathrm{d}} = 3.19$ kg, spring stiffness $k = 3800$ N/m, and an equivalent viscous damping $c_{\mathrm{d}} = 177$ Ns/m. A conductor tension of 25% RTS was considered. The experimental results were based on the optimum curve depicted in Fig. 11 of Ref. [32]. The mass of the clamp is ignored in order to properly represent the tested damper. The comparison of the experimental data and the computed results from the proposed model are presented in Fig. 3.10. They show very good agreement.

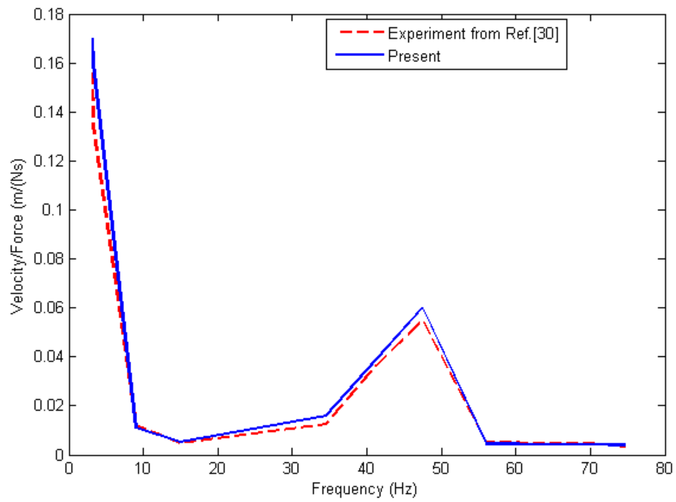

Figure 3.10: Validation of the proposed model via experiment from Ref.[32].

The second part of the validation and the remaining numerical analyses are based on the 795 Kcmil ASCR conductor and the Stockbridge damper data provided in the free vibration analysis section. The system is subjected to a concentrated harmonic force $f(t) = 100\sin(\Omega_{\mathrm{f}}t)$ N. The span length is $L = 200$ m and the damper is attached at a distance $L_1 = 3.333$ m. The equivalent viscous damping is obtained from Fig. 2.5 for each excitation frequency. Fig. 3.11 depicts plots of the conductor non-dimensional maximum vibration amplitude for various Strouhal frequencies which are obtained using both the proposed model and that in Ref. [2].

With reference to the conductor vibrational response, the results obtained using the present model are in good agreement with those obtained using Ref. [2]. The normalized mid-span vibration amplitude of the conductor (relative to the conductor diameter, D), decreases with increasing forcing frequency. The results for the damper show poor agreement with those obtained using the finite element method (see Ref. [2]). This poor agreement between the proposed simple model and the complete, but complicated, model of Ref. [2] indicates that the former cannot be used to predict the response of the counterweights. It is possible to reduce the discrepancy by tuning the relative magnitudes of the in-span and suspended masses, but this is ad hoc at best.

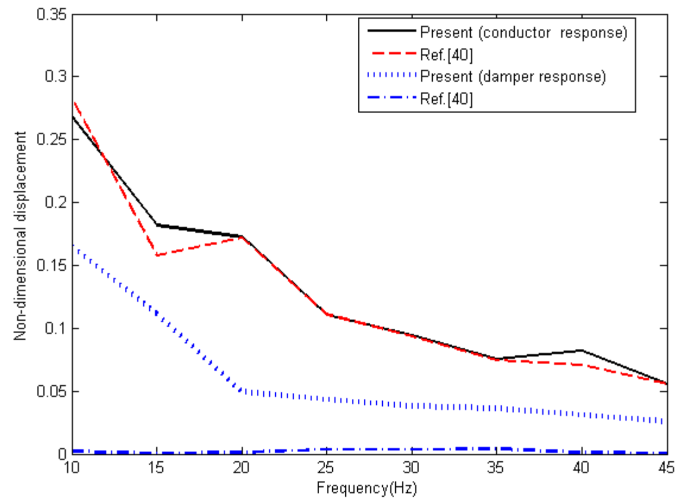

Figure 3.11: Validation of the proposed model via finite element from Ref.[2].

The effect of attaching one or two dampers on the conductor is demonstrated in Fig. 3.12. Three plots of the non-dimensionalized mid-span vibration amplitude are depicted. The first plot is that of the bare conductor, the second is for one damper at $L_1 = 3.33$ m, and the third is for two dampers at 3.33 m from each end. The results indicate that using one damper reduces the vibration of the conductor, and the reduction was most pronounced between 10 and 25 Hz. With two dampers, the vibration of the conductor is drastically reduced throughout the whole range of Strouhal frequency. To further illustrate the role of attaching two dampers, Fig. 3.13 depicts plots of vibration response of the bare and loaded conductor for a given Strouhal frequency of 20 Hz. The response of the bare conductor displays a resonance phenomenon as expected because the Strouhal frequency is closer to one of the system natural frequencies. This resonance is completely eliminated in the system with two dampers.

3.4 Summary

The conductor was modeled as a beam with a tensile load and the Stockbridge damper was reduced to an equivalent mass-spring-mass and viscous damping system. Expressions were presented for the frequency equation, mode shapes, and orthogonality conditions. Both free and forced vibration analyses were examined and the results were validated using the numerical and experimental results. In the free vibration analysis, it was demonstrated that the mass and the location of the damper have a significant impact on

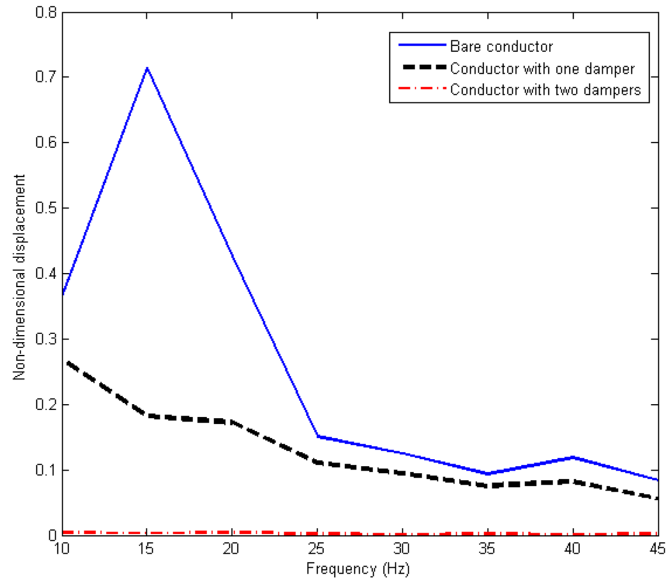

Figure 3.12: The effect of attaching dampers.

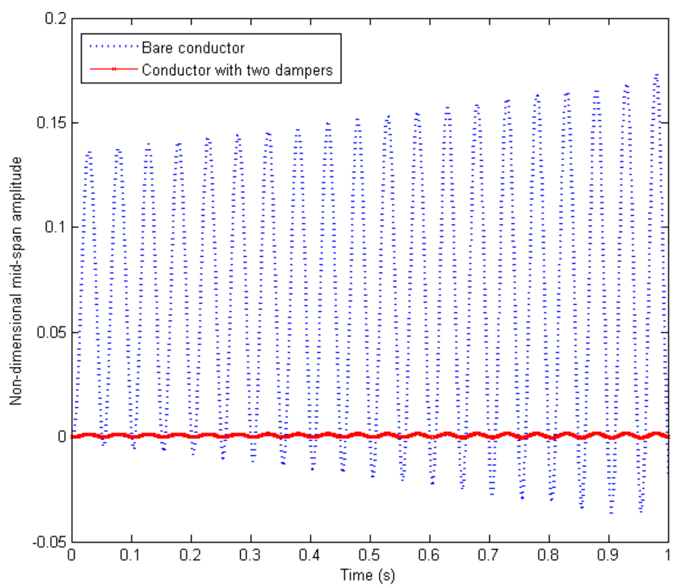

Figure 3.13: The bare and loaded conductor non-dimensional vibration amplitude at 20 Hz resonance forcing frequency.

the natural frequencies. The results in the forced vibration analysis indicated that the number of dampers and their locations are significant factors in controlling the vibration of the conductor. Overall, the model was found to be a good predictor of the response of the conductor, but a poor predictor of the response of the damper. It is believed that the simplicity of the damper model smears the damper dynamics. A more detail model is examinded in the next chapter to better capture the system dynamics.

Chapter 4

Double-Beam System

4.1 Introduction

Unlike in the previous chapter where the model was based on a beam with a mass-spring-damper system, the model presented in this chapter is based on double-beam concepts. The conductor is modeled as an axially loaded Euler-Bernoulli beam and the Stockbridge damper is modeled as an Euler-Bernoulli beam with rigid tip masses. This Stockbridge damper is arbitrary located along the span of the conductor. Numerous studies on the vibration of double-beam/string systems abound in the literature (see Refs. [79]-[86]). However, these investigations are either limited to cases where both beams are continuously connected by viscous elastic layers or where one of the beams is attached to the tip of the other.

In spite of these interests, there are no investigations where the primary beam is axially loaded and/or supporting in-span beam with tip mass. The use of this concept to analytically model a single-conductor transmission line with a Stockbridge damper was examined in this thesis for the first time. The equations of motion are derived using Hamilton's principle. The expressions for the characteristic equation, mode shapes, and orthogonality relations are presented. The analytical results are experimentally validated. Parametric studies are then used to examine the effect of the damper characteristics and location on the system natural frequencies and response. Part of the content in this chapter is published in [87, 88].

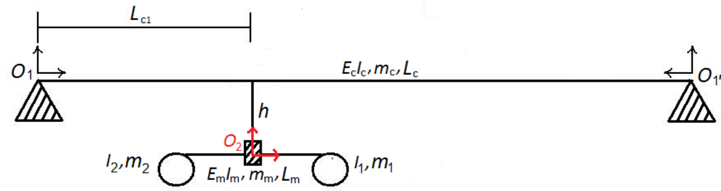

Figure 4.1: Schematic of a single conductor with a Stockbridge damper.

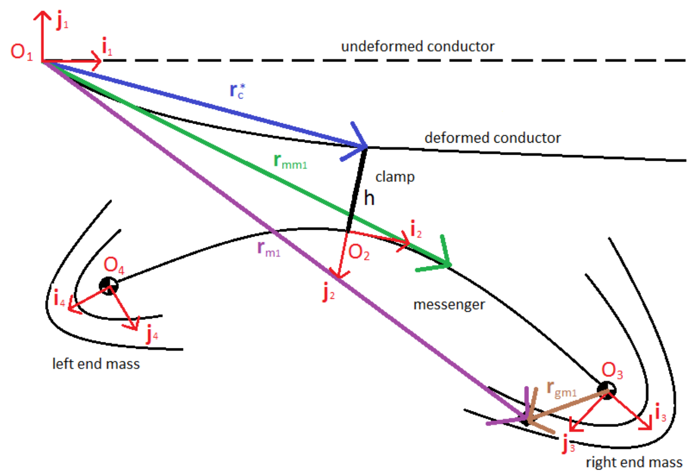

Figure 4.2: Close-up of damper.

4.2 Mathematical formulation

A schematic of a single conductor with a Stockbridge damper is depicted in Fig. 4.1. The conductor is represented as a pinned-pinned beam to delineate suspension spans. The Stockbridge damper is attached at a distance L_{c_1} and consists of a messenger (or damper cable), a mass (or counterweight) at each end of the messenger, and a clamp. This clamp is a rigid, massless link with length h (this is the distance separating the conductor and the messenger). The messenger is modeled as two cantilevered-beams with a tip mass at each end.

Two reference frames are attached at the ends of the conductor as shown in Fig. 4.1. A third reference frame is attached at the point of contact between the clamp and the messenger. The damper is attached at a distance L_{c_1} from the left-hand side reference frame; it divides the conductor into two segments. The transverse displacement of each segment is measured relative to the appropriate reference frame, and it is denoted by $w_{\mathrm{ci}}(x,t)$ for $i = 1, 2$. The messenger is also divided into two segments and the transverse displacement is denoted by $w_{\mathrm{mi}}(x_{\mathrm{m}}, t)$.

A close-up view of the conductor and damper deformation is depicted in Fig. 4.2. The position vector of a deformed differential element of the conductor is written as

$$\mathbf{r}_{\mathrm{c}}(x,t) = x\mathbf{i}_1 + w_{\mathrm{c}}(x,t)\mathbf{j}_1 \tag{4.1}$$

At the point of attachment of the damper $x = L_{c_1}$, the position is given as

$$\mathbf{r}_{\mathrm{c}}^{*} \equiv \mathbf{r}_{\mathrm{c}}(x = L_{c_1}, t) = L_{c_1}\mathbf{i}_1 + w_{\mathrm{c}}(L_{c_1}, t)\mathbf{j}_1 \tag{4.2}$$

The position vector of the messenger cable on the right and left segments are respectively given as

$$\mathbf{r}_{\mathrm{mm}_1} = h\mathbf{j}_2 + L_{\mathrm{m}_1}\mathbf{i_2} + w_{\mathrm{m}_1}\mathbf{j_2} + \mathbf{r}_{\mathrm{c}}^{*} \tag{4.3}$$

$$\mathbf{r}_{\mathrm{mm}_2} = h\mathbf{j}_2 - L_{\mathrm{m}_2}\mathbf{i_2} + w_{\mathrm{m}_2}\mathbf{j_2} + \mathbf{r}_{\mathrm{c}}^{*} \tag{4.4}$$

The position vector of the right- and left-end counterweights can be written as

$$\mathbf{r}_{\mathrm{m}_1} = h\mathbf{j}_2 + L_{\mathrm{m}_1}\mathbf{i_2} + w_{\mathrm{m}_1}^{*}\mathbf{j_2} + \mathbf{r}_{\mathrm{gm}_1} + \mathbf{r}_{\mathrm{c}}^{*} \tag{4.5}$$

$$\mathbf{r}_{\mathrm{m}_2} = h\mathbf{j}_2 - L_{\mathrm{m}_2}\mathbf{i_2} + w_{\mathrm{m}_2}^{*}\mathbf{j_2} + \mathbf{r}_{\mathrm{gm}_2} + \mathbf{r}_{\mathrm{c}}^{*} \tag{4.6}$$

where $w_{\mathrm{m}_1}^{*}$ ($w_{\mathrm{m}_2}^{*}$) is the transverse displacement of the right-end (left-end) counterweight.

Equations Eqs. (4.1)-(4.6) are used to derive the system kinetic $\mathcal{T}$ and potential $\mathcal{V}$ energy which, when higher-order terms (i.e., $O(3)$) are ignored, can be expressed as

$$\begin{aligned}
\mathcal{T} = \frac{1}{2}\sum_{i=1}^{2}\Bigg\{ & m_{\mathrm{c}}\int_0^{L_{\mathrm{ci}}} \dot{w}_{\mathrm{ci}}^2 dx + m_{\mathrm{i}}\left\{\dot{w}_{\mathrm{c}_1}^{*2} + 2\dot{w}_{\mathrm{c}_1}^{*}\left((-1)^{(\mathrm{i}+1)}\dot{w}_{\mathrm{c}_1}^{\prime *}L_{\mathrm{mi}} + \dot{w}_{\mathrm{mi}}^{*}\right)\right. \\
& \left. + \dot{w}_{\mathrm{c}_1}^{\prime *2}\left(h^2 + L_{\mathrm{mi}}^2\right) + (-1)^{(\mathrm{i}+1)}2L_{\mathrm{mi}}\dot{w}_{\mathrm{mi}}^{*}\dot{w}_{\mathrm{c}_1}^{\prime *} + \dot{w}_{\mathrm{mi}}^{*2}\right\} \\
& + I_{\mathrm{i}}\left(\dot{w}_{\mathrm{c}_1}^{\prime *} + (-1)^{(\mathrm{i}+1)}\dot{w}_{\mathrm{mi}}^{\prime *}\right)^2 + m_{\mathrm{mi}}\left(\dot{w}_{\mathrm{c}_1}^{*2} + \left(\dot{w}_{\mathrm{c}_1}^{\prime *}h\right)^2\right) \\
& + m_{\mathrm{m}}\int_0^{L_{\mathrm{mi}}}\left\{2\dot{w}_{\mathrm{c}_1}^{*}\dot{w}_{\mathrm{mi}} + (-1)^{(\mathrm{i}+1)}2x_{\mathrm{m}}\dot{w}_{\mathrm{c}_1}^{\prime *}\dot{w}_{\mathrm{mi}} + \dot{w}_{\mathrm{mi}}^2\right\}dx_{\mathrm{m}} \\
& + m_{\mathrm{m}}\left((-1)^{(\mathrm{i}+1)}\dot{w}_{\mathrm{c}_1}^{*}\dot{w}_{\mathrm{c}_1}^{\prime *}L_{\mathrm{mi}}^2 + \frac{1}{3}\dot{w}_{\mathrm{c}_1}^{\prime *2}L_{\mathrm{mi}}^3\right)\Bigg\}
\end{aligned} \tag{4.7}$$

$$\mathcal{V} = \frac{1}{2}\sum_{i=1}^{2}\left(E_{\mathrm{c}}I_{\mathrm{c}}\int_{0}^{L_{\mathrm{ci}}} w''^{2}_{\mathrm{ci}}dx + T\int_{0}^{L_{\mathrm{ci}}} w'^{\,2}_{\mathrm{ci}}dx + E_{\mathrm{m}}I_{\mathrm{m}}\int_{0}^{L_{\mathrm{mi}}} w_{\mathrm{mi}}''^{2}dx_{\mathrm{m}}\right) \tag{4.8}$$

where m_1 (m_2) is the tip mass on the right-hand (left-hand) side; L_{m_1} (L_{m_2}) is the length of the messenger on the right-hand (left-hand) side; m_{c} (m_{m}) is the mass per unit length of the conductor (messenger); m_{m1} (m_{m2}) is the mass of the messenger on the right-hand (left-hand) side; T denotes the conductor tension; $E_{\mathrm{c}}I_{\mathrm{c}}$ ($E_{\mathrm{m}}I_{\mathrm{m}}$) is the flexural rigidity of the conductor (messenger); and T is the tension in the conductor. The overdots and primes denote temporal and spatial derivation, respectively.

The equations of motion, Eqs. (4.9) and (4.10), are obtained by substituting the energy expressions in the Hamilton's principle and taking the variations of the field variables (δw_{c_1}, δw_{c_2}, δw_{m_1}, and δw_{m_2}).

$$m_{\mathrm{c}}\ddot{w}_{\mathrm{ci}} + E_{\mathrm{c}}I_{\mathrm{c}}w''''{}_{\mathrm{ci}} - Tw''{}_{\mathrm{ci}} = 0 \tag{4.9}$$

$$m_{\mathrm{m}}\left(\ddot{w}^{*}_{\mathrm{c}_1} + (-1)^{(\mathrm{i}+1)}\ddot{w}'^{*}_{\mathrm{c}_1}L_{\mathrm{mi}} + \ddot{w}_{\mathrm{mi}}\right) + E_{\mathrm{m}}I_{\mathrm{m}}w''''{}_{\mathrm{mi}} = 0 \tag{4.10}$$

Note that the subscript 'i' $\in [1,2]$ identifies the right-hand and left-hand segments of both the conductor and messenger. The continuity conditions of the displacement at the attachment point of the damper to the conductor, L_{c_1}, yield

$$w_{\mathrm{c}_1}\left(L_{\mathrm{c}_1}, t\right) = w_{\mathrm{c}_2}\left(L_{\mathrm{c}_2}, t\right) \tag{4.11}$$

$$w_{\mathrm{c}_1}{}'\left(L_{\mathrm{c}_1}, t\right) = -w_{\mathrm{c}_2}{}'\left(L_{\mathrm{c}_2}, t\right) \tag{4.12}$$

From the variation of the conductor displacement, δw_{c_1}, the obtained shear force boundary condition at the location of the damper may be written as

$$\begin{aligned}\sum_{i=1}^{2}\Bigg\{ & m_{\mathrm{i}}\left(\ddot{w}^{*}_{\mathrm{c}_1} + (-1)^{(\mathrm{i}+1)}\ddot{w}'^{*}_{\mathrm{c}_1}L_{\mathrm{mi}} + \ddot{w}^{*}_{\mathrm{mi}}\right) + \ddot{w}^{*}_{\mathrm{c}_1}m_{\mathrm{mi}} \\ & + m_{\mathrm{m}}\int_{0}^{L_{\mathrm{mi}}}\ddot{w}_{\mathrm{mi}}dx_{\mathrm{m}} + \frac{1}{2}m_{\mathrm{m}}\ddot{w}'^{*}_{\mathrm{c}_1}(-1)^{(\mathrm{i}+1)}L^{2}_{\mathrm{mi}}\Bigg\} \\ & - E_{\mathrm{c}}I_{\mathrm{c}}\left(w_{\mathrm{c}_1}{}'''^{*} + w_{\mathrm{c}_2}{}'''^{*}\right) + T\left(w'^{*}_{\mathrm{c}_1} + w'^{*}_{\mathrm{c}_2}\right) = 0\end{aligned} \tag{4.13}$$

The contributions from the tension vanish because of Eq. (4.12). The bending moment boundary condition at the attachment of the messenger may be expressed as

$$\begin{aligned}
&\sum_{i=1}^{2}\Big\{m_\mathrm{i}\left[(-1)^{(\mathrm{i}+1)}\ddot{w}^*_{\mathrm{c}_1}L_\mathrm{mi}+w'^*_\mathrm{c}\left(h^2+L^2_\mathrm{mi}\right)+(-1)^{(\mathrm{i}+1)}L_\mathrm{mi}\ddot{w}^*_\mathrm{mi}\right]\\
&\quad+I_\mathrm{i}\left(\ddot{w}'^*_{\mathrm{c}_1}+(-1)^{(\mathrm{i}+1)}\ddot{w}'^*_\mathrm{mi}\right)+\ddot{w}'^*_{\mathrm{c}_1}h^2m_\mathrm{mi}\\
&\quad+m_\mathrm{m}\int_0^{L_\mathrm{mi}}(-1)^{(\mathrm{i}+1)}x_\mathrm{m}\ddot{w}_\mathrm{mi}dx_\mathrm{m}\\
&\quad+\frac{1}{2}m_\mathrm{m}\left((-1)^{(\mathrm{i}+1)}\ddot{w}^*_{\mathrm{c}_1}L^2_\mathrm{mi}+\frac{2}{3}\ddot{w}'^*_{\mathrm{c}_1}L^3_\mathrm{mi}\right)\Big\}\\
&\quad+E_\mathrm{c}I_\mathrm{c}\left({w_{\mathrm{c}_1}}''^*-{w_{\mathrm{c}_2}}''^*\right)=0
\end{aligned}\tag{4.14}$$

The last set of boundary conditions for the conductor are obtained by enforcing no displacement and bending moment conditions at both ends of each segment:

$$w_\mathrm{ci}(0,t)=0 \tag{4.15}$$

$${w_\mathrm{ci}}''(0,t)=0 \tag{4.16}$$

With respect to the messenger, the shear force boundary conditions at each end, L_{m_1} and L_{m_2}, can be expressed as

$$m_\mathrm{i}\left(\ddot{w}^*_\mathrm{mi}+\ddot{w}^*_{\mathrm{c}_1}+(-1)^{(\mathrm{i}+1)}L_\mathrm{mi}\ddot{w}'^*_{\mathrm{c}_1}\right)-E_\mathrm{m}I_\mathrm{m}{w_\mathrm{mi}}'''^*=0 \tag{4.17}$$

and the bending moment boundary condition at each end is

$$I_\mathrm{i}\left(\ddot{w}'^*_\mathrm{mi}+(-1)^{(\mathrm{i}+1)}\ddot{w}'^*_{\mathrm{c}_1}\right)+E_\mathrm{m}I_\mathrm{m}{w_\mathrm{mi}}''^*=0 \tag{4.18}$$

The Stockbrigde damper behaves as a cantilevered beam at the junction of the clamp and the messenger $x_\mathrm{m}=0$. Hence, the displacement and rotation of both right and left-side messenger are zero:

$$w_\mathrm{mi}(0,t)=0 \tag{4.19}$$

$${w_\mathrm{mi}}'(0,t)=0 \tag{4.20}$$

4.2.1 Frequency equation and mode shapes

The transverse vibration displacement for each segment of the conductor and messenger can be expressed as

$$w_{\mathrm{ci}}(x,t) = Y_{\mathrm{ci}}(x)e^{i\omega t} \tag{4.21}$$

$$w_{\mathrm{mi}}(x_{\mathrm{m}},t) = Y_{\mathrm{mi}}(x)e^{i\omega t} \tag{4.22}$$

Substituting the above equations, Eqs. (4.21) and (4.22), into the equations of motion, Eqs. (4.9) and (4.10), yields

$$Y_{\mathrm{ci}}'''' - S^2 Y_{\mathrm{ci}}'' - \Omega_{\mathrm{c}}^4 Y_{\mathrm{ci}} = 0 \tag{4.23}$$

$$Y_{\mathrm{mi}}'''' - \Omega_{\mathrm{m}}^4 Y_{\mathrm{mi}} = \Omega_{\mathrm{m}}^4 \left(Y_{\mathrm{c_1}}^* + (-1)^{(\mathrm{i}+1)} Y_{\mathrm{c_1}}'^* x_{\mathrm{m}}\right) \tag{4.24}$$

where $\Omega_{\mathrm{c}} = \left(\dfrac{\omega^2 m_{\mathrm{c}}}{E_{\mathrm{c}} I_{\mathrm{c}}}\right)^{\frac{1}{4}}$, $\Omega_{\mathrm{m}} = \left(\dfrac{\omega^2 m_{\mathrm{m}}}{E_{\mathrm{m}} I_{\mathrm{m}}}\right)^{\frac{1}{4}}$ and $S = \sqrt{\dfrac{T}{E_{\mathrm{c}} I_{\mathrm{c}}}}$.

The solutions of the above differential equations can be expressed as

$$Y_{\mathrm{ci}}(x) = A_{1\mathrm{i}} \sin \alpha x + A_{2\mathrm{i}} \cos \alpha x + A_{3\mathrm{i}} \sinh \beta x + A_{4\mathrm{i}} \cosh \beta x \tag{4.25}$$

$$\begin{aligned} Y_{\mathrm{mi}}(x_{\mathrm{m}}) &= B_{1\mathrm{i}} \sin \Omega_{\mathrm{m}} x_{\mathrm{m}} + B_{2\mathrm{i}} \cos \Omega_{\mathrm{m}} x_{\mathrm{m}} + B_{3\mathrm{i}} \sinh \Omega_{\mathrm{m}} x_{\mathrm{m}} \\ &\quad + B_{4\mathrm{i}} \cosh \Omega_{\mathrm{m}} x_{\mathrm{m}} - (Y_{\mathrm{c_1}}^* + (-1)^{(\mathrm{i}+1)} x_{\mathrm{m}} Y_{\mathrm{c_1}}'^*) \end{aligned} \tag{4.26}$$

where $\alpha = \sqrt{-\dfrac{S^2}{2} + \sqrt{\dfrac{S^4}{4} + \Omega_{\mathrm{c}}^4}}$ and $\beta = \sqrt{\dfrac{S^2}{2} + \sqrt{\dfrac{S^4}{4} + \Omega_{\mathrm{c}}^4}}$.

By applying boundary conditions at each end of the conductor, the coefficients A_{21}, A_{41}, A_{22}, and A_{42} vanishes and Eq. (4.25) reduces to

$$Y_{\mathrm{ci}}(x) = A_{1\mathrm{i}} \sin \alpha x + A_{3\mathrm{i}} \sinh \beta x \tag{4.27}$$

Substituting Eq. (4.21) in Eqs. (4.11) and (4.12) yields

$$Y_{\mathrm{c_1}}(L_{\mathrm{c_1}}) = Y_{\mathrm{c_2}}(L_{\mathrm{c_2}}) \tag{4.28}$$

$$Y_{\mathrm{c_1}}'(L_{\mathrm{c_1}}) = -Y_{\mathrm{c_2}}'(L_{\mathrm{c_2}}) \tag{4.29}$$

Eqs. (4.21) and (4.22) are substituted in the shear forces boundary condition, Eq. (4.13) at $x = L_{\mathrm{c}_1}$, and after some algebraic manipulation yields

$$
\begin{aligned}
\omega^2 \sum_{i=1}^{2} \Big\{ & m_{\mathrm{i}} \left(Y^*_{\mathrm{c}_1} + (-1)^{(\mathrm{i}+1)} Y'^*_{\mathrm{c}_1} L_{\mathrm{mi}} + Y^*_{\mathrm{mi}} \right) + m_{\mathrm{mi}} Y^*_{\mathrm{c}_1} \\
& + m_{\mathrm{m}} \int_0^{L_{\mathrm{mi}}} Y_{\mathrm{mi}} dx_{\mathrm{m}} + (-1)^{(\mathrm{i}+1)} \frac{1}{2} m_{\mathrm{m}} Y'^*_{\mathrm{c}_1} L^2_{\mathrm{mi}} \Big\} \\
& + E_{\mathrm{c}} I_{\mathrm{c}} \left(Y'''^*_{\mathrm{c}_1} + Y'''^*_{\mathrm{c}_2} \right) = 0
\end{aligned}
\tag{4.30}
$$

Similarly, the bending moment boundary condition at $x = L_{\mathrm{c}_1}$ (i.e., Eq. (4.14)) yields

$$
\begin{aligned}
\omega^2 \sum_{i=1}^{2} \Big\{ & m_{\mathrm{i}} \left[(-1)^{(\mathrm{i}+1)} Y^*_{\mathrm{c}_1} L_{\mathrm{mi}} + Y'^*_{\mathrm{c}_1} \left(L^2_{\mathrm{mi}} + h^2 \right) + (-1)^{(\mathrm{i}+1)} L_{\mathrm{mi}} Y^*_{\mathrm{mi}} \right] \\
& + I_{\mathrm{i}} \left(Y'^*_{\mathrm{c}_1} + (-1)^{(\mathrm{i}+1)} Y'^*_{\mathrm{mi}} \right) + m_{\mathrm{mi}} h^2 Y'^*_{\mathrm{c}_1} \\
& + m_{\mathrm{m}} \int_0^{L_{\mathrm{mi}}} (-1)^{(\mathrm{i}+1)} x_{\mathrm{m}} w_{\mathrm{mi}} dx_{\mathrm{m}} \\
& + \frac{1}{2} m_{\mathrm{m}} \left((-1)^{(\mathrm{i}+1)} Y^*_{\mathrm{c}_1} L^2_{\mathrm{mi}} + \frac{2}{3} Y'^*_{\mathrm{c}_1} L^3_{\mathrm{mi}} \right) \Big\} \\
& - E_{\mathrm{c}} I_{\mathrm{c}} \left(Y''^*_{\mathrm{c}_1} - Y''^*_{\mathrm{c}_2} \right) = 0
\end{aligned}
\tag{4.31}
$$

For the messenger cable, Eqs. (4.21) and (4.22) are substituted into Eqs. (4.17) and (4.18) to obtain the following:

$$
Y^*_{\mathrm{c}_1} + (-1)^{(\mathrm{i}+1)} L_{\mathrm{mi}} {Y_{\mathrm{c}_1}}' + Y^*_{\mathrm{mi}} + \lambda_{\mathrm{mi}} Y'''^*_{\mathrm{mi}} = 0 \tag{4.32}
$$

$$
(-1)^{(\mathrm{i}+1)} Y'^*_{\mathrm{c}_1} + Y'^*_{\mathrm{mi}} - \kappa_{\mathrm{mi}} Y''^*_{\mathrm{mi}} = 0 \tag{4.33}
$$

where $\lambda_{\mathrm{mi}} = \dfrac{E_{\mathrm{m}} I_{\mathrm{m}}}{m_{\mathrm{i}} \omega^2}$, $\kappa_{\mathrm{mi}} = \dfrac{E_{\mathrm{m}} I_{\mathrm{m}}}{I_{\mathrm{i}} \omega^2}$.

Eqs. (4.19) and (4.20) naturally reduce to

$$
Y_{\mathrm{mi}}(0) = 0 \tag{4.34}
$$

$$
{Y_{\mathrm{mi}}}'(0) = 0 \tag{4.35}
$$

For the sake of simplicity, the following notations are used

$$
\begin{aligned}
s_{\mathrm{i}} &= \sin \alpha L_{\mathrm{c_i}}, & sh_{\mathrm{i}} &= \sinh \beta L_{\mathrm{c_i}}, \\
c_{\mathrm{i}} &= \cos \alpha L_{\mathrm{c_i}}, & ch_{\mathrm{i}} &= \cosh \beta L_{\mathrm{c_i}}, \\
s_{\Omega i} &= \sin \Omega_{\mathrm{m}} L_{\mathrm{m_i}}, & sh_{\Omega i} &= \sinh \Omega_{\mathrm{m}} L_{\mathrm{m_i}}, \\
c_{\Omega i} &= \cos \Omega_{\mathrm{m}} L_{\mathrm{m_i}}, & ch_{\Omega i} &= \sinh \Omega_{\mathrm{m}} L_{\mathrm{m_i}}
\end{aligned}
$$

A set of 12 algebraic homogeneous equations (four are from the conductor and eight from the messenger) are obtained by substituting Eqs. (4.26) and (4.27) into Eqs. (4.28) to (4.35). These algebraic equations are linear in the unknown coefficients (A's and B's) and can be written in matrix format as

$$
[\mathcal{F}]_{12\mathrm{X}12} \{q\}_{12\mathrm{X}12} = \{0\}_{12\mathrm{X}12} \tag{4.36}
$$

where
$q = [A_{11}, A_{31}, A_{12}, A_{32}, B_{11}, B_{21}, B_{31}, B_{41}, B_{12}, B_{22}, B_{32}, B_{42}]^T$, with the supercript T denoting transposition. A non-trivial solution to the equation is possible when matrix $\mathcal{F}$ is singular. Hence, the characteristic or frequency equation is obtained as

$$
det([\mathcal{F}]_{12\mathrm{X}12}) = 0 \tag{4.37}
$$

It should be noted that matrix $[\mathcal{F}_{\mathrm{i,j}}]$ comprises 144 elements in which the 64 non-zero entries are given as

$$
\begin{aligned}
&\mathcal{F}_{1,1} = s_1, \quad \mathcal{F}_{1,2} = sh_1, \quad \mathcal{F}_{1,3} = -s_2, \quad \mathcal{F}_{1,1} = -sh_2 \\
&\mathcal{F}_{2,1} = \alpha c_1, \quad \mathcal{F}_{2,2} = \beta ch_1, \quad \mathcal{F}_{2,3} = \alpha c_2, \quad \mathcal{F}_{2,4} = \beta ch_2
\end{aligned}
$$

$$
\begin{aligned}
\mathcal{F}_{3,1} &= \alpha c_1 h^2 (m_1 + m_2 + m_{\mathrm{m}_1} + m_{\mathrm{m}_2}) + \frac{\alpha^2}{\omega^2} E_{\mathrm{c}} I_{\mathrm{c}} s_1 \\
\mathcal{F}_{3,2} &= \beta ch_1 h^2 (m_1 + m_2 + m_{\mathrm{m}_1} + m_{\mathrm{m}_2}) - \frac{\beta^2}{\omega^2} E_{\mathrm{c}} I_{\mathrm{c}} sh_1 \\
\mathcal{F}_{3,3} &= -\frac{\alpha^2}{\omega^2} s_2 E_{\mathrm{c}} I_{\mathrm{c}}, \qquad \mathcal{F}_{3,4} = \frac{\beta^2}{\omega^2} sh_2 E_{\mathrm{c}} I_{\mathrm{c}}
\end{aligned}
$$

$$\mathcal{F}_{3,5} = m_1 L_{\mathrm{m}_1} s_{\Omega 1} + \Omega_{\mathrm{m}} c_{\Omega 1} I_1 + m_{\mathrm{m}} \left(-\frac{L_{\mathrm{m}_1} c_{\Omega 1}}{\Omega_{\mathrm{m}}} + \frac{1}{\Omega_{\mathrm{m}}^2} s_{\Omega 1} \right)$$
$$\mathcal{F}_{3,6} = m_1 L_{\mathrm{m}_1} c_{\Omega 1} - \Omega_{\mathrm{m}} s_{\Omega 1} I_1 + m_{\mathrm{m}} \left(\frac{L_{\mathrm{m}_1} s_{\Omega 1}}{\Omega_{\mathrm{m}}} + \frac{1}{\Omega_{\mathrm{m}}^2} (c_{\Omega 1} - 1) \right)$$
$$\mathcal{F}_{3,7} = m_1 L_{\mathrm{m}_1} sh_{\Omega 1} + \Omega_{\mathrm{m}} ch_{\Omega 1} I_1 + m_{\mathrm{m}} \left(\frac{L_{\mathrm{m}_1} ch_{\Omega 1}}{\Omega_{\mathrm{m}}} - \frac{1}{\Omega_{\mathrm{m}}^2} sh_{\Omega 1} \right)$$
$$\mathcal{F}_{3,8} = m_1 L_{\mathrm{m}_1} ch_{\Omega 1} + \Omega_{\mathrm{m}} sh_{\Omega 1} I_1 + m_{\mathrm{m}} \left(\frac{L_{\mathrm{m}_1} sh_{\Omega 1}}{\Omega_{\mathrm{m}}} - \frac{1}{\Omega_{\mathrm{m}}^2} (ch_{\Omega 1} - 1) \right)$$
$$\mathcal{F}_{3,9} = -m_2 L_{\mathrm{m}_2} s_{\Omega 2} - \Omega_{\mathrm{m}} c_{\Omega 2} I_2 - m_{\mathrm{m}} \left(-\frac{L_{\mathrm{m}_2} c_{\Omega 2}}{\Omega_{\mathrm{m}}} + \frac{1}{\Omega_{\mathrm{m}}^2} s_{\Omega 2} \right)$$
$$\mathcal{F}_{3,10} = -m_2 L_{\mathrm{m}_2} c_{\Omega 2} + \Omega_{\mathrm{m}} s_{\Omega 2} I_2 - m_{\mathrm{m}} \left(\frac{L_{\mathrm{m}_2} s_{\Omega 2}}{\Omega_{\mathrm{m}}} + \frac{1}{\Omega_{\mathrm{m}}^2} (c_{\Omega 2} - 1) \right)$$
$$\mathcal{F}_{3,11} = -m_2 L_{\mathrm{m}_2} sh_{\Omega 2} - \Omega_{\mathrm{m}} ch_{\Omega 2} I_2 - m_{\mathrm{m}} \left(\frac{L_{\mathrm{m}_2} ch_{\Omega 2}}{\Omega_{\mathrm{m}}} - \frac{1}{\Omega_{\mathrm{m}}^2} sh_{\Omega 2} \right)$$
$$\mathcal{F}_{3,12} = -m_2 L_{\mathrm{m}_2} ch_{\Omega 2} - \Omega_{\mathrm{m}} sh_{\Omega 2} I_2 - m_{\mathrm{m}} \left(\frac{L_{\mathrm{m}_2} sh_{\Omega 2}}{\Omega_{\mathrm{m}}} - \frac{1}{\Omega_{\mathrm{m}}^2} (ch_{\Omega 2} - 1) \right)$$

$$\mathcal{F}_{4,1} = \frac{-\alpha^3}{\omega^2} c_1 E_{\mathrm{c}} I_{\mathrm{c}}, \qquad \mathcal{F}_{4,2} = \frac{\beta^3}{\omega^2} ch_1 E_{\mathrm{c}} I_{\mathrm{c}}$$
$$\mathcal{F}_{4,3} = \frac{-\alpha^3}{\omega^2} c_2 E_{\mathrm{c}} I_{\mathrm{c}}, \qquad \mathcal{F}_{4,4} = \frac{\beta^3}{\omega^2} ch_2 E_{\mathrm{c}} I_{\mathrm{c}}$$

$$\mathcal{F}_{4,5} = m_1 s_{\Omega 1} - \frac{m_{\mathrm{m}}}{\Omega_{\mathrm{m}}} (c_{\Omega 1} - 1), \qquad \mathcal{F}_{4,6} = m_1 c_{\Omega 1} + \frac{m_{\mathrm{m}}}{\Omega_{\mathrm{m}}} s_{\Omega 1}$$
$$\mathcal{F}_{4,7} = m_1 sh_{\Omega 1} + \frac{m_{\mathrm{m}}}{\Omega_{\mathrm{m}}} (ch_{\Omega 1} - 1), \qquad \mathcal{F}_{4,8} = m_1 ch_{\Omega 1} + \frac{m_{\mathrm{m}}}{\Omega_{\mathrm{m}}} sh_{\Omega 1}$$
$$\mathcal{F}_{4,9} = m_2 s_{\Omega 2} - \frac{m_{\mathrm{m}}}{\Omega_{\mathrm{m}}} (c_{\Omega 2} - 1), \qquad \mathcal{F}_{4,10} = m_2 c_{\Omega 2} + \frac{m_{\mathrm{m}}}{\Omega_{\mathrm{m}}} s_{\Omega 2}$$
$$\mathcal{F}_{4,11} = m_2 sh_{\Omega 2} + \frac{m_{\mathrm{m}}}{\Omega_{\mathrm{m}}} (ch_{\Omega 2} - 1), \qquad \mathcal{F}_{4,12} = m_2 ch_{\Omega 2} + \frac{m_{\mathrm{m}}}{\Omega_{\mathrm{m}}} sh_{\Omega 2}$$

$$\mathcal{F}_{5,5} = s_{\Omega 1} - \lambda_{\mathrm{m}_1} \Omega_{\mathrm{m}}^3 c_{\Omega 1}, \qquad \mathcal{F}_{5,6} = c_{\Omega 1} + \lambda_{\mathrm{m}_1} \Omega_{\mathrm{m}}^3 s_{\Omega 1}$$
$$\mathcal{F}_{5,7} = sh_{\Omega 1} + \lambda_{\mathrm{m}_1} \Omega_{\mathrm{m}}^3 ch_{\Omega 1}, \qquad \mathcal{F}_{5,8} = ch_{\Omega 1} + \lambda_{\mathrm{m}_1} \Omega_{\mathrm{m}}^3 sh_{\Omega 1}$$

$$\mathcal{F}_{6,9} = s_{\Omega 2} - \lambda_{\mathrm{m}_2} \Omega_{\mathrm{m}}^3 c_{\Omega 2}, \qquad \mathcal{F}_{6,10} = c_{\Omega 2} + \lambda_{\mathrm{m}_2} \Omega_{\mathrm{m}}^3 s_{\Omega 2}$$
$$\mathcal{F}_{6,11} = sh_{\Omega 2} + \lambda_{\mathrm{m}_2} \Omega_{\mathrm{m}}^3 ch_{\Omega 2}, \qquad \mathcal{F}_{6,12} = ch_{\Omega 2} + \lambda_{\mathrm{m}_2} \Omega_{\mathrm{m}}^3 sh_{\Omega 2}$$

$$\mathcal{F}_{7,5} = c_{\Omega 1} + \kappa_{\mathrm{m}_1} \Omega_{\mathrm{m}} s_{\Omega 1}, \qquad \mathcal{F}_{7,6} = -s_{\Omega 1} + \kappa_{\mathrm{m}_1} \Omega_{\mathrm{m}} c_{\Omega 1}$$
$$\mathcal{F}_{7,7} = ch_{\Omega 1} - \kappa_{\mathrm{m}_1} \Omega_{\mathrm{m}} sh_{\Omega 1}, \qquad \mathcal{F}_{7,8} = sh_{\Omega 1} - \kappa_{\mathrm{m}_1} \Omega_{\mathrm{m}} ch_{\Omega 1}$$

$$\mathcal{F}_{8,9} = c_{\Omega 2} + \kappa_{\mathrm{m}_2}\Omega_{\mathrm{m}} s_{\Omega 2}, \qquad \mathcal{F}_{8,10} = -s_{\Omega 2} + \kappa_{\mathrm{m}_2}\Omega_{\mathrm{m}} c_{\Omega 2}$$
$$\mathcal{F}_{8,11} = ch_{\Omega 2} - \kappa_{\mathrm{m}_2}\Omega_{\mathrm{m}} sh_{\Omega 2}, \quad \mathcal{F}_{8,12} = sh_{\Omega 2} - \kappa_{\mathrm{m}_2}\Omega_{\mathrm{m}} ch_{\Omega 2}$$

$$\mathcal{F}_{9,1} = \mathcal{F}_{10,1} = -s_1, \qquad \mathcal{F}_{9,2} = \mathcal{F}_{10,2} = -sh_1$$
$$\mathcal{F}_{9,6} = \mathcal{F}_{9,8} = \mathcal{F}_{10,10} = \mathcal{F}_{10,12} = 1$$
$$\mathcal{F}_{11,1} = \frac{-\alpha c_1}{\Omega_{\mathrm{m}}}, \qquad \mathcal{F}_{11,2} = \frac{-\beta ch_1}{\Omega_{\mathrm{m}}}$$
$$\mathcal{F}_{12,1} = -\mathcal{F}_{11,1}, \qquad \mathcal{F}_{12,2} = -\mathcal{F}_{11,2}$$

The mode shapes of the conductor are deduced by using Eq. (4.28) while ignoring the hyberbolic function terms since the tension and the span length in transmission lines are usually very high. Assuming that $A_{11} = 1$, the conductor mode shapes for each segment can be expressed as

$$Y_{\mathrm{c}_1}(x) = \sin \alpha x_1 \tag{4.38}$$
$$Y_{\mathrm{c}_2}(x) = \frac{s_1}{s_2} \sin \alpha x_2 \tag{4.39}$$

The mode shapes of the messenger are derived by using the shear and moment conditions at each end of the messenger, Eqs. (4.32) and (4.33), and the displacement and slope at the clamp, Eqs. (4.34) and (4.35). With reference to Eq. (4.26), the coefficients of the mode shapes of the messenger are

$$\begin{aligned} B_{1\mathrm{i}} = \frac{1}{\lambda_{\mathrm{i}}} \Big\{ & \mathcal{F}_{11,1}\mathcal{F}_{(\mathrm{i}+4),7}\mathcal{F}_{(\mathrm{i}+6),8} - \mathcal{F}_{11,1}\mathcal{F}_{(\mathrm{i}+4),7}\mathcal{F}_{(\mathrm{i}+6),6} + \mathcal{F}_{1,1}\mathcal{F}_{(\mathrm{i}+4),6}\mathcal{F}_{(\mathrm{i}+6),8} \\ & -\mathcal{F}_{1,1}\mathcal{F}_{(\mathrm{i}+4),8}\mathcal{F}_{(\mathrm{i}+6),6} - \mathcal{F}_{11,1}\mathcal{F}_{(\mathrm{i}+4),8}\mathcal{F}_{(\mathrm{i}+6),7} + \mathcal{F}_{11,1}\mathcal{F}_{(\mathrm{i}+4),6}\mathcal{F}_{(\mathrm{i}+6),7} \Big\} \end{aligned} \tag{4.40}$$

$$\begin{aligned} B_{2\mathrm{i}} = -\frac{1}{\lambda_{\mathrm{i}}} \Big\{ & -\mathcal{F}_{1,1}\mathcal{F}_{(\mathrm{i}+6),8}\mathcal{F}_{(\mathrm{i}+4),7} + \mathcal{F}_{1,1}\mathcal{F}_{(\mathrm{i}+6),8}\mathcal{F}_{(\mathrm{i}+4),5} + \mathcal{F}_{1,1}\mathcal{F}_{(\mathrm{i}+6),7}\mathcal{F}_{(\mathrm{i}+4),8} \\ & -\mathcal{F}_{1,1}\mathcal{F}_{(\mathrm{i}+6),5}\mathcal{F}_{(\mathrm{i}+4),8} - \mathcal{F}_{11,1}\mathcal{F}_{(\mathrm{i}+6),5}\mathcal{F}_{(\mathrm{i}+4),7} + \mathcal{F}_{11,1}\mathcal{F}_{(\mathrm{i}+6),7}\mathcal{F}_{(\mathrm{i}+4),5} \Big\} \end{aligned} \tag{4.41}$$

$$\begin{aligned} B_{3\mathrm{i}} = -\frac{1}{\lambda_{\mathrm{i}}} \Big\{ & \mathcal{F}_{11,1}\mathcal{F}_{(\mathrm{i}+6),8}\mathcal{F}_{(\mathrm{i}+4),5} - \mathcal{F}_{11,1}\mathcal{F}_{(\mathrm{i}+6),6}\mathcal{F}_{(\mathrm{i}+4),5} + \mathcal{F}_{1,1}\mathcal{F}_{(\mathrm{i}+4),6}\mathcal{F}_{(\mathrm{i}+6),8} \\ & -\mathcal{F}_{1,1}\mathcal{F}_{(\mathrm{i}+4),8}\mathcal{F}_{(\mathrm{i}+6),6} - \mathcal{F}_{11,1}\mathcal{F}_{(\mathrm{i}+6),5}\mathcal{F}_{(\mathrm{i}+4),8} + \mathcal{F}_{11,1}\mathcal{F}_{(\mathrm{i}+6),5}\mathcal{F}_{(\mathrm{i}+4),6} \Big\} \end{aligned} \tag{4.42}$$

$$B_{4\mathrm{i}} = \frac{1}{\lambda_\mathrm{i}} \Big\{ -\mathcal{F}_{11,1}\mathcal{F}_{(\mathrm{i}+6),5}\mathcal{F}_{(\mathrm{i}+4),7} - \mathcal{F}_{1,1}\mathcal{F}_{(\mathrm{i}+6),6}\mathcal{F}_{(\mathrm{i}+4),7} + \mathcal{F}_{1,1}\mathcal{F}_{(\mathrm{i}+6),6}\mathcal{F}_{(\mathrm{i}+4),5} + \mathcal{F}_{11,1}\mathcal{F}_{(\mathrm{i}+6),7}\mathcal{F}_{(\mathrm{i}+4),5} + \mathcal{F}_{1,1}\mathcal{F}_{(\mathrm{i}+6),7}\mathcal{F}_{(\mathrm{i}+4),6} - \mathcal{F}_{1,1}\mathcal{F}_{(\mathrm{i}+6),5}\mathcal{F}_{(\mathrm{i}+4),6} \Big\} \tag{4.43}$$

where

$$\lambda_\mathrm{i} = \mathcal{F}_{(\mathrm{i}+6),8}\mathcal{F}_{(\mathrm{i}+4),7} - \mathcal{F}_{(\mathrm{i}+6),8}\mathcal{F}_{(\mathrm{i}+4),5} - \mathcal{F}_{(\mathrm{i}+6),6}\mathcal{F}_{(\mathrm{i}+4),7} + \mathcal{F}_{(\mathrm{i}+6),8}\mathcal{F}_{(\mathrm{i}+4),5} - \mathcal{F}_{(\mathrm{i}+6),7}\mathcal{F}_{(\mathrm{i}+4),8} + \mathcal{F}_{(\mathrm{i}+6),7}\mathcal{F}_{(\mathrm{i}+4),6} + \mathcal{F}_{(\mathrm{i}+6),5}\mathcal{F}_{(\mathrm{i}+4),8} - \mathcal{F}_{(\mathrm{i}+6),5}\mathcal{F}_{(\mathrm{i}+4),6}$$

The expression of the natural frequency of the bare conductor are obtained in Ref. [2] and is given as

$$f_\mathrm{n} = \frac{n}{2L_\mathrm{c}} \sqrt{\frac{T}{m_\mathrm{c}} + \left(\frac{n\pi}{L_\mathrm{c}}\right)^2 \frac{E_\mathrm{c} I_\mathrm{c}}{m_\mathrm{c}}} \tag{4.44}$$

where f_n is natural frequency in Hz and n is the mode number.

4.2.2 Orthogonality condition

Since Eqs. (4.23) and (4.24) are valid for all modes, they can be rewritten as

$$Y_\mathrm{ci}^{(r)^{IV}} - S^2 Y_\mathrm{ci}^{(r)''} = \Omega_\mathrm{c}^{(r)^4} Y_\mathrm{ci}^{(r)} \tag{4.45}$$

$$Y_\mathrm{mi}^{(r)^{IV}} - \Omega_m^{(r)^4}\left(Y_{\mathrm{c}_1}^{(r)^*} + (-1)^{(\mathrm{i}+1)} Y_{\mathrm{c}_1}^{(r)^{*'}} x_\mathrm{m}\right) = \Omega_\mathrm{m}^{(r)^4} Y_\mathrm{mi}^{(r)} \tag{4.46}$$

Multiplying Eq. (4.45) by $Y_\mathrm{ci}^{(s)}$ and integrating from 0 to L_ci yield

$$\Omega_\mathrm{c}^{(r)^4} \int_0^{L_\mathrm{ci}} Y_\mathrm{ci}^{(r)} Y_\mathrm{ci}^{(s)} dx = \int_0^{L_\mathrm{ci}} Y_\mathrm{ci}^{(r)^{IV}} Y_\mathrm{ci}^{(s)} dx - S^2 \int_0^{L_\mathrm{ci}} Y_\mathrm{ci}^{(r)''} Y_\mathrm{ci}^{(s)} \tag{4.47}$$

Applying integration by parts to Eq.(4.47) and using boundary and matching conditions Eqs. (4.28) to (4.31) yield

$$
\begin{aligned}
\Omega_{\mathrm{c}}^{(r)^4} \sum_{i=1}^{2} \int_{0}^{L_{\mathrm{ci}}} Y_{\mathrm{ci}}^{(r)} Y_{\mathrm{ci}}^{(s)} dx = \frac{\Omega_{\mathrm{c}}^{(r)^4}}{m_{\mathrm{c}}} \Bigg\{ & -Y_{\mathrm{c_1}}^{(s)^*} \sum_{i=1}^{2} \Bigg[m_{\mathrm{i}} \left(Y_{\mathrm{c_1}}^{(r)^*} + (-1)^{(\mathrm{i}+1)} Y_{\mathrm{c_1}}^{(r)^{*'}} L_{\mathrm{mi}} + Y_{\mathrm{mi}}^{(r)^*} \right) \\
& + Y_{\mathrm{c_1}}^{(r)^*} m_{\mathrm{m}} L_{\mathrm{mi}} + m_{\mathrm{m}} \int_{0}^{L_{\mathrm{mi}}} Y_{\mathrm{mi}}^{(r)} dx_{\mathrm{m}} + (-1)^{(\mathrm{i}+1)} \frac{1}{2} m_{\mathrm{m}} Y_{\mathrm{c_1}}^{(r)^{*'}} L_{\mathrm{mi}}^2 \Bigg] \\
& + Y_{\mathrm{c_1}}^{(s)^{*'}} \sum_{i=1}^{2} \Bigg[m_{\mathrm{i}} \Big((-1)^{(\mathrm{i}+1)} Y_{\mathrm{c_1}}^{(r)^*} L_{\mathrm{mi}} + Y_{\mathrm{c_1}}^{(r)^{*'}} \left(L_{\mathrm{mi}}^2 + h^2 \right) \\
& + (-1)^{(\mathrm{i}+1)} L_{\mathrm{mi}} Y_{\mathrm{mi}}^{(r)^*} \Big) + I_{\mathrm{i}} \left(Y_{\mathrm{c_1}}^{(r)^{*'}} + (-1)^{(\mathrm{i}+1)} Y_{\mathrm{mi}}^{(r)^{*'}} \right) \\
& + Y_{\mathrm{c_1}}^{(r)^{*'}} h^2 m_{\mathrm{m}} L_{\mathrm{mi}} + m_{\mathrm{m}} \Bigg((-1)^{(\mathrm{i}+1)} \int_{0}^{L_{\mathrm{mi}}} x_{\mathrm{m}} Y_{\mathrm{mi}}^{(r)} dx_{\mathrm{m}} \\
& + (-1)^{(\mathrm{i}+1)} \frac{1}{2} Y_{\mathrm{c_1}}^{(r)^*} L_{\mathrm{mi}}^2 + \frac{1}{3} Y_{\mathrm{c_1}}^{(r)^{*'}} L_{\mathrm{mi}}^3 \Bigg) \Bigg] \\
& + \sum_{i=1}^{2} \left[\int_{0}^{L_{\mathrm{ci}}} Y_{\mathrm{ci}}^{(r)''} Y_{\mathrm{ci}}^{(s)''} dx - S^2 \int_{0}^{L_{\mathrm{ci}}} Y_{\mathrm{ci}}^{(r)'} Y_{\mathrm{ci}}^{(s)'} dx \right]
\end{aligned}
\tag{4.48}
$$

Similary, Eq. (4.46) can be manipulated by using the boundary and continuity conditions Eqs. (4.32) - (4.35) to obtain the following:

$$
\begin{aligned}
\Omega_{\mathrm{m}}^{(r)^4} \sum_{i=1}^{2} \int_{0}^{L_{\mathrm{mi}}} Y_{\mathrm{mi}}^{(r)} Y_{\mathrm{mi}}^{(s)} dx = -\frac{\Omega_{\mathrm{m}}^{(r)^4}}{m_{\mathrm{m}}} \sum_{i=1}^{2} \Bigg[& m_{\mathrm{i}} Y_{\mathrm{mi}}^{(s)^*} \left(Y_{\mathrm{c_1}}^{(r)^*} + (-1)^{(\mathrm{i}+1)} Y_{\mathrm{c_1}}^{(r)^{*'}} L_{\mathrm{mi}} + Y_{\mathrm{mi}}^{(r)^*} \right) \\
& + I_{\mathrm{i}} Y_{\mathrm{mi}}^{(s)^{*'}} \left(Y_{\mathrm{mi}}^{(r)^{*'}} + (-1)^{(\mathrm{i}+1)} Y_{\mathrm{ci}}^{(r)^{*'}} \right) \\
& - m_{\mathrm{m}} \int_{0}^{L_{\mathrm{mi}}} Y_{\mathrm{mi}}^{(s)} \left(Y_{\mathrm{c_1}}^{(r)^*} + (-1)^{(\mathrm{i}+1)} x_{\mathrm{m}} Y_{\mathrm{c_1}}^{(r)^*} \right) dx_{\mathrm{m}} \Bigg] \\
& + \sum_{i=1}^{2} \left[\int_{0}^{L_{\mathrm{mi}}} Y_{\mathrm{mi}}^{(r)''} Y_{\mathrm{mi}}^{(s)''} dx_{\mathrm{m}} \right]
\end{aligned}
\tag{4.49}
$$

By multiplying Eq. (4.49) by $\dfrac{m_{\mathrm{m}} \Omega_{\mathrm{c}}^{r}}{m_{\mathrm{m}} \Omega_{\mathrm{c}}^{r}}$ and adding the resulting equation to Eq. (4.48) yields

$$
\begin{aligned}
\Omega_{\mathrm{c}}^{(r)^4} \sum_{i=1}^{2} \left(\int_0^{L_{\mathrm{ci}}} Y_{\mathrm{ci}}^{(r)} Y_{\mathrm{ci}}^{(s)} dx + \frac{m_{\mathrm{m}}}{m_{\mathrm{c}}} \int_0^{L_{\mathrm{mi}}} Y_{\mathrm{mi}}^{(r)} Y_{\mathrm{mi}}^{(s)} dx_{\mathrm{m}} \right) = \sum_{i=1}^{2} \Bigg(\int_0^{L_{\mathrm{ci}}} Y_{\mathrm{ci}}^{(r)''} Y_{\mathrm{ci}}^{(s)''} dx \\
- S^2 \int_0^{L_{\mathrm{ci}}} Y_{\mathrm{ci}}^{(r)'} Y_{\mathrm{ci}}^{(s)'} dx + \frac{E_{\mathrm{m}} I_{\mathrm{m}}}{E_{\mathrm{c}} I_{\mathrm{c}}} \int_0^{L_{\mathrm{mi}}} Y_{\mathrm{mi}}^{(r)''} Y_{\mathrm{mi}}^{(s)''} dx \Bigg) \\
- \frac{\Omega_{\mathrm{c}}^{(r)^4}}{m_{\mathrm{c}}} \sum_{i=1}^{2} \Bigg\{ Y_{\mathrm{c_1}}^{(s)^*} \Bigg[m_{\mathrm{i}} \left(Y_{\mathrm{c_1}}^{(r)^*} + (-1)^{(\mathrm{i}+1)} Y_{\mathrm{c_1}}^{(r)^{*'}} L_{\mathrm{mi}} + Y_{\mathrm{mi}}^{(r)^*} \right) \\
+ Y_{\mathrm{c_1}}^{(r)^*} m_{\mathrm{m}} L_{\mathrm{mi}} + m_{\mathrm{m}} \int_0^{L_{\mathrm{mi}}} Y_{\mathrm{mi}}^{(r)} dx_{\mathrm{m}} + (-1)^{(\mathrm{i}+1)} \frac{1}{2} m_{\mathrm{m}} Y_{\mathrm{c_1}}^{(r)^{*'}} L_{\mathrm{mi}}^2 \Bigg] \\
+ Y_{\mathrm{c_1}}^{(s)^{*'}} \Bigg[m_{\mathrm{i}} \Big((-1)^{(\mathrm{i}+1)} Y_{\mathrm{c_1}}^{(r)^*} L_{\mathrm{mi}} + Y_{\mathrm{c_1}}^{(r)^{*'}} \left(L_{\mathrm{mi}}^2 + h^2 \right) \\
+ (-1)^{(\mathrm{i}+1)} L_{\mathrm{mi}} Y_{\mathrm{mi}}^{(r)^*} \Big) + I_{\mathrm{i}} \left(Y_{\mathrm{c_1}}^{(r)^{*'}} + (-1)^{(\mathrm{i}+1)} Y_{\mathrm{mi}}^{(r)^{*'}} \right) \\
+ Y_{\mathrm{c_1}}^{(r)^{*'}} h^2 m_{\mathrm{m}} L_{\mathrm{mi}} + m_{\mathrm{m}} \Bigg((-1)^{(\mathrm{i}+1)} \int_0^{L_{\mathrm{mi}}} x_{\mathrm{m}} Y_{\mathrm{mi}}^{(r)} dx_{\mathrm{m}} \\
+ (-1)^{(\mathrm{i}+1)} \frac{1}{2} Y_{\mathrm{c_1}}^{(r)^*} L_{\mathrm{mi}}^2 + \frac{1}{3} Y_{\mathrm{c_1}}^{(r)^{*'}} L_{\mathrm{mi}}^3 \Bigg) \Bigg] \\
+ m_{\mathrm{i}} Y_{\mathrm{mi}}^{(s)^*} \left(Y_{\mathrm{c_1}}^{(r)^*} + (-1)^{(\mathrm{i}+1)} Y_{\mathrm{c_1}}^{(r)^{*'}} L_{\mathrm{mi}} + Y_{\mathrm{mi}}^{(r)^*} \right) \\
+ I_{\mathrm{i}} Y_{\mathrm{mi}}^{(s)^{*'}} \left(Y_{\mathrm{mi}}^{(r)^{*'}} + (-1)^{(\mathrm{i}+1)} Y_{\mathrm{ci}}^{(r)^{*'}} \right) \\
- m_{\mathrm{m}} \int_0^{L_{\mathrm{mi}}} Y_{\mathrm{mi}}^{(s)} \left(Y_{\mathrm{c_1}}^{(r)^*} + (-1)^{(\mathrm{i}+1)} x_{\mathrm{m}} Y_{\mathrm{c_1}}^{(r)^*} \right) dx_{\mathrm{m}} \Bigg\}
\end{aligned}
\tag{4.50}
$$

Exchanging the subscripts "s" and "r" in Eq. (4.50) and substracting the resulting equation from Eq. (4.50) yields

$$
\begin{aligned}
&\left(\Omega_{\mathrm{c}}^{(r)^4} - \Omega_{\mathrm{c}}^{(s)^4}\right) \sum_{i=1}^{2} \Bigg\{ m_{\mathrm{c}} \int_0^{L_{\mathrm{ci}}} Y_{\mathrm{ci}}^{(r)} Y_{\mathrm{ci}}^{(s)} dx + m_{\mathrm{m}} \int_0^{L_{\mathrm{mi}}} Y_{\mathrm{mi}}^{(r)} Y_{\mathrm{mi}}^{(s)} dx_{\mathrm{m}} \\
&+ Y_{\mathrm{c_1}}^{(r)^*} Y_{\mathrm{c_1}}^{(s)^*} \left(m_{\mathrm{i}} + m_{\mathrm{m}} L_{\mathrm{mi}}\right) + Y_{\mathrm{c_1}}^{(r)^{*'}} Y_{\mathrm{c_1}}^{(s)^{*'}} \left[m_{\mathrm{i}} \left(L_{\mathrm{mi}}^2 + h^2\right) + I_{\mathrm{i}} + h^2 m_{\mathrm{m}} L_{\mathrm{mi}} + \frac{1}{3} L_{\mathrm{mi}}^3\right] \\
&+ Y_{\mathrm{mi}}^{(r)^*} Y_{\mathrm{mi}}^{(s)^*} m_{\mathrm{mi}} + Y_{\mathrm{mi}}^{(r)^{*'}} Y_{\mathrm{mi}}^{(s)^{*'}} I_{\mathrm{i}} + (-1)^{(\mathrm{i}+1)} m_{\mathrm{i}} L_{\mathrm{mi}} \left(Y_{\mathrm{c_1}}^{(r)^{*'}} Y_{\mathrm{c_1}}^{(s)^*} + Y_{\mathrm{c_1}}^{(r)^*} Y_{\mathrm{c_1}}^{(s)^{*'}}\right) \\
&+ m_{\mathrm{mi}} \left(Y_{\mathrm{c_1}}^{(r)^*} Y_{\mathrm{mi}}^{(s)^*} + Y_{\mathrm{c_1}}^{(s)^*} Y_{\mathrm{mi}}^{(r)^*}\right) + m_{\mathrm{m}} \int_0^{L_{\mathrm{mi}}} \left(Y_{\mathrm{c_1}}^{(r)^*} Y_{\mathrm{mi}}^{(s)^*} + Y_{\mathrm{c_1}}^{(s)^*} Y_{\mathrm{mi}}^{(r)^*}\right) dx_{\mathrm{m}} \\
&+ (-1)^{(\mathrm{i}+1)} \frac{1}{2} m_{\mathrm{m}} L_{\mathrm{mi}}^2 \left(Y_{\mathrm{c_1}}^{(r)^*} Y_{\mathrm{c_1}}^{(s)^{*'}} + Y_{\mathrm{c_1}}^{(s)^*} Y_{\mathrm{c_1}}^{(r)^{*'}}\right) + (-1)^{(\mathrm{i}+1)} m_{\mathrm{i}} L_{\mathrm{mi}} \Big(Y_{\mathrm{c_1}}^{(r)^{*'}} Y_{\mathrm{mi}}^{(s)^*} \\
&+ Y_{\mathrm{c_1}}^{(s)^{*'}} Y_{\mathrm{mi}}^{(r)^*}\Big) + (-1)^{(\mathrm{i}+1)} I_{\mathrm{i}} \left(Y_{\mathrm{c_1}}^{(r)^{*'}} Y_{\mathrm{mi}}^{(s)^{*'}} + Y_{\mathrm{c_1}}^{(s)^{*'}} Y_{\mathrm{mi}}^{(r)^{*'}}\right) \\
&+ (-1)^{(\mathrm{i}+1)} m_{\mathrm{m}} \int_0^{L_{\mathrm{mi}}} x_{\mathrm{m}} \left(Y_{\mathrm{c_1}}^{(r)^{*'}} Y_{\mathrm{mi}}^{(s)} + Y_{\mathrm{c_1}}^{(s)^{*'}} Y_{\mathrm{mi}}^{(r)}\right) dx_{\mathrm{m}} \Bigg\} = 0
\end{aligned}
\tag{4.51}
$$

The first orthogonality relation can now be expressed as

$$
\begin{aligned}
&\sum_{i=1}^{2} \Bigg\{ m_{\mathrm{c}} \int_0^{L_{\mathrm{ci}}} Y_{\mathrm{ci}}^{(r)} Y_{\mathrm{ci}}^{(s)} dx + m_{\mathrm{m}} \int_0^{L_{\mathrm{mi}}} Y_{\mathrm{mi}}^{(r)} Y_{\mathrm{mi}}^{(s)} dx_{\mathrm{m}} + Y_{\mathrm{c_1}}^{(r)^*} Y_{\mathrm{c_1}}^{(s)^*} \left(m_{\mathrm{i}} + m_{\mathrm{m}} L_{\mathrm{mi}}\right) \\
&+ Y_{\mathrm{c_1}}^{(r)^{*'}} Y_{\mathrm{c_1}}^{(s)^{*'}} \left[m_{\mathrm{i}} \left(L_{\mathrm{mi}}^2 + h^2\right) + I_{\mathrm{i}} + h^2 m_{\mathrm{m}} L_{\mathrm{mi}} + \frac{1}{3} L_{\mathrm{mi}}^3\right] + Y_{\mathrm{mi}}^{(r)^*} Y_{\mathrm{mi}}^{(s)^*} m_{\mathrm{mi}} \\
&+ Y_{\mathrm{mi}}^{(r)^{*'}} Y_{\mathrm{mi}}^{(s)^{*'}} I_{\mathrm{i}} + (-1)^{(\mathrm{i}+1)} m_{\mathrm{i}} L_{\mathrm{mi}} \left(Y_{\mathrm{c_1}}^{(r)^{*'}} Y_{\mathrm{c_1}}^{(s)^*} + Y_{\mathrm{c_1}}^{(r)^*} Y_{\mathrm{c_1}}^{(s)^{*'}}\right) \\
&+ m_{\mathrm{mi}} \left(Y_{\mathrm{c_1}}^{(r)^*} Y_{\mathrm{mi}}^{(s)^*} + Y_{\mathrm{c_1}}^{(s)^*} Y_{\mathrm{mi}}^{(r)^*}\right) + m_{\mathrm{m}} \int_0^{L_{\mathrm{mi}}} \Big(Y_{\mathrm{c_1}}^{(r)^*} Y_{\mathrm{mi}}^{(s)^*} \\
&+ Y_{\mathrm{c_1}}^{(s)^*} Y_{\mathrm{mi}}^{(r)^*}\Big) dx_{\mathrm{m}} + (-1)^{(\mathrm{i}+1)} \frac{1}{2} m_{\mathrm{m}} L_{\mathrm{mi}}^2 \left(Y_{\mathrm{c_1}}^{(r)^*} Y_{\mathrm{c_1}}^{(s)^{*'}} + Y_{\mathrm{c_1}}^{(s)^*} Y_{\mathrm{c_1}}^{(r)^{*'}}\right) \\
&+ (-1)^{(\mathrm{i}+1)} m_{\mathrm{i}} L_{\mathrm{mi}} \left(Y_{\mathrm{c_1}}^{(r)^{*'}} Y_{\mathrm{mi}}^{(s)^*} + Y_{\mathrm{c_1}}^{(s)^{*'}} Y_{\mathrm{mi}}^{(r)^*}\right) + (-1)^{(\mathrm{i}+1)} I_{\mathrm{i}} \Big(Y_{\mathrm{c_1}}^{(r)^{*'}} Y_{\mathrm{mi}}^{(s)^{*'}} \\
&+ Y_{\mathrm{c_1}}^{(s)^{*'}} Y_{\mathrm{mi}}^{(r)^{*'}}\Big) + (-1)^{(\mathrm{i}+1)} m_{\mathrm{m}} \int_0^{L_{\mathrm{mi}}} x_{\mathrm{m}} \left(Y_{\mathrm{c_1}}^{(r)^{*'}} Y_{\mathrm{mi}}^{(s)} + Y_{\mathrm{c_1}}^{(s)^{*'}} Y_{\mathrm{mi}}^{(r)}\right) dx_{\mathrm{m}} \Bigg\} = \delta_{\mathrm{rs}}
\end{aligned}
\tag{4.52}
$$

where δ_{rs} is the Kronecker delta. By using Eqs. (4.50) and (4.52), the second orthogonality relation is obtained as

$$\sum_{i=1}^{2}\left(\int_0^{L_{\mathrm{ci}}} Y_{\mathrm{ci}}^{(r)''} Y_{\mathrm{ci}}^{(s)''}\,dx - S^2\int_0^{L_{\mathrm{ci}}} Y_{\mathrm{ci}}^{(r)'} Y_{\mathrm{ci}}^{(s)'}\,dx + \frac{E_{\mathrm{m}} I_{\mathrm{m}}}{E_{\mathrm{c}} I_{\mathrm{c}}}\int_0^{L_{\mathrm{mi}}} Y_{\mathrm{mi}}^{(r)''} Y_{\mathrm{mi}}^{(s)''}\,dx\right) = \delta_{\mathrm{rs}} \tag{4.53}$$

4.2.3 Forced vibration

The equation of motion for the forced vibration is given as

$$m_{\mathrm{c}}\ddot{w}_{\mathrm{ci}} + E_{\mathrm{c}} I_{\mathrm{c}} w_{\mathrm{ci}}^{IV} - T w_{\mathrm{ci}}^{''} = F(t)\delta(x - L_{\mathrm{c}}/2) \tag{4.54}$$

$$m_{\mathrm{m}}\left(\ddot{w}_{\mathrm{mi}} + (-1)^{(\mathrm{i}+1)}\ddot{w}_{\mathrm{ci}}^{*'} x_{\mathrm{m}} + w_{\mathrm{ci}}^{*}\right) + E_{\mathrm{m}} I_{\mathrm{m}} w_{\mathrm{mi}}^{IV} = 0 \tag{4.55}$$

and the excitation force is expressed as

$$F(t) = F_0 \sin(2\pi f_{\mathrm{s}} t) \tag{4.56}$$

where F_0 denotes the excitation amplitude force in N and f_{s} is the forcing frequency in Hz. Using mode superposition principle, the deflection of the beam is assumed as

$$w_{\mathrm{ci}} = \sum_{r=1}^{\infty} q_{\mathrm{r}}(t) Y_{\mathrm{ci}}^{(r)}(x) \tag{4.57}$$

$$w_{\mathrm{mi}} = \sum_{r=1}^{\infty} q_{\mathrm{r}}(t) Y_{\mathrm{mi}}^{(r)}(x) \tag{4.58}$$

The excitation frequency, also referred to as Strouhal frequency [1], is given by

$$f_{\mathrm{s}} = 0.2\frac{v}{D} \tag{4.59}$$

where v is the wind speed (varying from 1 to 7 m/s) and D is the diameter of the conductor in meters.

Substituting Eqs. (4.57) and (4.58) into Eqs. (4.54) and (4.55) yields

$$m_{\mathrm{c}}\sum_{r=1}^{\infty}\ddot{q}_{\mathrm{r}} Y_{\mathrm{ci}}^{(r)} + E_{\mathrm{c}} I_{\mathrm{c}}\sum_{r=1}^{\infty} q_{\mathrm{r}} Y_{\mathrm{ci}}^{(r)^{IV}} - T\sum_{r=1}^{\infty} q_{\mathrm{r}} Y_{\mathrm{ci}}^{(r)''} = F(t)\delta(x - a) \tag{4.60}$$

$$m_{\mathrm{m}}\sum_{r=1}^{\infty}\ddot{q}_{\mathrm{r}}\left(Y_{\mathrm{mi}}^{(r)} + (-1)^{(\mathrm{i}+1)} Y_{\mathrm{ci}}^{(r)^{*'}} x_{\mathrm{m}} + Y_{\mathrm{ci}}^{(r)^{*}}\right) + E_{\mathrm{m}} I_{\mathrm{m}}\sum_{r=1}^{\infty} q_{\mathrm{r}} Y_{\mathrm{ci}}^{(r)^{IV}} = 0 \tag{4.61}$$

Multiply Eqs.(4.60) and (4.61) by $Y_{\mathrm{ci}}^{(s)}$ and $Y_{\mathrm{mi}}^{(s)}$, repsectively. Integrating the resulting former equation from 0 to L_{ci} and the latter from 0 to L_{mi}, adding the two resulting equations, and applying boundary and continuity conditions yield

$$[M_{\mathrm{rs}}]\{\ddot{q}_{\mathrm{r}}\}+[K_{\mathrm{rs}}]\{q_{\mathrm{r}}\}=[F_{\mathrm{r}}] \tag{4.62}$$

where

$$\begin{aligned}
M_{\mathrm{rs}}=\sum_{i=1}^{2}\Bigg\{ & m_{\mathrm{c}}\int_0^{L_{\mathrm{ci}}} Y_{\mathrm{ci}}^{(r)}Y_{\mathrm{ci}}^{(s)}dx+m_{\mathrm{m}}\int_0^{L_{\mathrm{mi}}} Y_{\mathrm{mi}}^{(r)}Y_{\mathrm{mi}}^{(s)}dx_{\mathrm{m}}+Y_{\mathrm{c1}}^{(r)^*}Y_{\mathrm{c1}}^{(s)^*}\left(m_{\mathrm{i}}+m_{\mathrm{m}}L_{\mathrm{mi}}\right)\\
&+Y_{\mathrm{c1}}^{(r)^{*\prime}}Y_{\mathrm{c1}}^{(s)^{*\prime}}\left[m_{\mathrm{i}}\left(L_{\mathrm{mi}}^2+h^2\right)+I_{\mathrm{i}}+h^2m_{\mathrm{m}}L_{\mathrm{mi}}+\frac{1}{3}L_{\mathrm{mi}}^3\right]+Y_{\mathrm{mi}}^{(r)^*}Y_{\mathrm{mi}}^{(s)^*}m_{\mathrm{mi}}\\
&+Y_{\mathrm{mi}}^{(r)^{*\prime}}Y_{\mathrm{mi}}^{(s)^{*\prime}}I_{\mathrm{i}}+(-1)^{(\mathrm{i}+1)}m_{\mathrm{i}}L_{\mathrm{mi}}\left(Y_{\mathrm{c1}}^{(r)^{*\prime}}Y_{\mathrm{c1}}^{(s)^*}+Y_{\mathrm{c1}}^{(r)^*}Y_{\mathrm{c1}}^{(s)^{*\prime}}\right)+m_{\mathrm{mi}}\left(Y_{\mathrm{c1}}^{(r)^*}Y_{\mathrm{mi}}^{(s)^*}+Y_{\mathrm{c1}}^{(s)^*}Y_{\mathrm{mi}}^{(r)^*}\right)\\
&+m_{\mathrm{m}}\int_0^{L_{\mathrm{mi}}}\left(Y_{\mathrm{c1}}^{(r)^*}Y_{\mathrm{mi}}^{(s)^*}+Y_{\mathrm{c1}}^{(s)^*}Y_{\mathrm{mi}}^{(r)^*}\right)dx_{\mathrm{m}}+(-1)^{(\mathrm{i}+1)}\frac{1}{2}m_{\mathrm{m}}L_{\mathrm{mi}}^2\left(Y_{\mathrm{c1}}^{(r)^*}Y_{\mathrm{c1}}^{(s)^{*\prime}}+Y_{\mathrm{c1}}^{(s)^*}Y_{\mathrm{c1}}^{(r)^{*\prime}}\right)\\
&+(-1)^{(\mathrm{i}+1)}m_{\mathrm{i}}L_{\mathrm{mi}}\left(Y_{\mathrm{c1}}^{(r)^{*\prime}}Y_{\mathrm{mi}}^{(s)^*}+Y_{\mathrm{c1}}^{(s)^{*\prime}}Y_{\mathrm{mi}}^{(r)^*}\right)+(-1)^{(\mathrm{i}+1)}I_{\mathrm{i}}\left(Y_{\mathrm{c1}}^{(r)^{*\prime}}Y_{\mathrm{mi}}^{(s)^{*\prime}}+Y_{\mathrm{c1}}^{(s)^{*\prime}}Y_{\mathrm{mi}}^{(r)^{*\prime}}\right)\\
&+(-1)^{(\mathrm{i}+1)}m_{\mathrm{m}}\int_0^{L_{\mathrm{mi}}}\left(Y_{\mathrm{c1}}^{(r)^{*\prime}}Y_{\mathrm{mi}}^{(s)}+Y_{\mathrm{c1}}^{(s)^{*\prime}}Y_{\mathrm{mi}}^{(r)}\right)dx_{\mathrm{m}}\Bigg\}
\end{aligned} \tag{4.63}$$

$$K_{\mathrm{rs}}=\sum_{i=1}^{2}\left(E_{\mathrm{c}}I_{\mathrm{c}}\int_0^{L_{\mathrm{ci}}}Y_{\mathrm{ci}}^{(r)''}Y_{\mathrm{ci}}^{(s)''}dx-T\int_0^{L_{\mathrm{ci}}}Y_{\mathrm{ci}}^{(r)'}Y_{\mathrm{ci}}^{(s)'}dx+E_{\mathrm{m}}I_{\mathrm{m}}\int_0^{L_{\mathrm{mi}}}Y_{\mathrm{mi}}^{(r)''}Y_{\mathrm{mi}}^{(s)''}dx\right) \tag{4.64}$$

$$F_{\mathrm{r}}=F(t)Y_{\mathrm{ci}}(x=\frac{L_{\mathrm{c}}}{2}) \tag{4.65}$$

Using orthogonality relation Eqs.(4.52) and (4.53) yield

$$
\begin{aligned}
M_{\mathrm{rr}} = \sum_{i=1}^{2} \Bigg\{ & m_{\mathrm{c}} \int_{0}^{L_{\mathrm{ci}}} Y_{\mathrm{ci}}^{(r)^2} dx + m_{\mathrm{m}} \int_{0}^{L_{\mathrm{mi}}} Y_{\mathrm{mi}}^{(r)^2} dx_{\mathrm{m}} + Y_{\mathrm{c1}}^{(r)^{2*}} \left(m_{\mathrm{i}} + m_{\mathrm{m}} L_{\mathrm{mi}}\right) \\
& + Y_{\mathrm{c1}}^{(r)^{2*'}} \left[m_{\mathrm{i}} \left(L_{\mathrm{mi}}^2 + h^2\right) + I_{\mathrm{i}} + h^2 m_{\mathrm{m}} L_{\mathrm{mi}} + \frac{1}{3} L_{\mathrm{mi}}^3 \right] + Y_{\mathrm{mi}}^{(r)^{2*}} m_{\mathrm{mi}} + Y_{\mathrm{mi}}^{(r)^{2*'}} I_{\mathrm{i}} \\
& + (-1)^{(\mathrm{i}+1)} 2 m_{\mathrm{i}} L_{\mathrm{mi}} Y_{\mathrm{c1}}^{(r)^{*'}} Y_{\mathrm{c1}}^{(r)^{*}} + 2 m_{\mathrm{mi}} Y_{\mathrm{c1}}^{(r)^{*}} Y_{\mathrm{mi}}^{(r)^{*}} + 2 m_{\mathrm{m}} \int_{0}^{L_{\mathrm{mi}}} Y_{\mathrm{c1}}^{(r)^{*}} Y_{\mathrm{mi}}^{(r)} dx_{\mathrm{m}} \\
& + (-1)^{(\mathrm{i}+1)} m_{\mathrm{m}} L_{\mathrm{mi}}^2 Y_{\mathrm{c1}}^{(r)^{*}} Y_{\mathrm{c1}}^{(r)^{*'}} + (-1)^{(\mathrm{i}+1)} 2 m_{\mathrm{i}} L_{\mathrm{mi}} Y_{\mathrm{c1}}^{(r)^{*'}} Y_{\mathrm{mi}}^{(r)^{*}} \\
& + (-1)^{(\mathrm{i}+1)} 2 I_{\mathrm{i}} Y_{\mathrm{c1}}^{(r)^{*'}} Y_{\mathrm{mi}}^{(r)^{*'}} + (-1)^{(\mathrm{i}+1)} 2 m_{\mathrm{m}} \int_{0}^{L_{\mathrm{mi}}} Y_{\mathrm{c1}}^{(r)^{*'}} Y_{\mathrm{mi}}^{(r)} dx_{\mathrm{m}} \Bigg\}
\end{aligned}
\tag{4.66}
$$

$$
K_{\mathrm{rr}} = \sum_{i=1}^{2} \left\{ \int_{0}^{L_{\mathrm{ci}}} \left[E_{\mathrm{c}} I_{\mathrm{c}} Y_{\mathrm{ci}}^{(r)^{2''}} - T Y_{\mathrm{ci}}^{(r)^{2'}} \right] dx + E_{\mathrm{m}} I_{\mathrm{m}} \int_{0}^{L_{\mathrm{mi}}} Y_{\mathrm{mi}}^{(r)^{2''}} dx \right\} \tag{4.67}
$$

Adding the conductor damping ratio (ζ) Eq.(4.62) becomes

$$
\{\ddot{q}_{\mathrm{r}}\} + [\omega_{\mathrm{r}}]^2 \{q_{\mathrm{r}}\} + 2\zeta [\omega_{\mathrm{r}}] \{\dot{q}_{\mathrm{r}}\} = [F_{\mathrm{r}}] \tag{4.68}
$$

where

$$
[\omega_{\mathrm{r}}]^2 = [K_{\mathrm{rr}}] [M_{\mathrm{rr}}]^{-1} \tag{4.69}
$$

4.3 Discussion

The numerical simulation is based on the tested conductor and Stockbridge damper. The material and geometric properties are listed in Table 2.1. The length of the conductor $L_{\mathrm{c}} = 27.25$ m, with flexural rigidity $E_{\mathrm{c}} I_{\mathrm{c}} = 1602$ Nm^2, and and linear mass density $m_{\mathrm{c}} = 1.628$ kg/m. This numerical analysis comprises two parts. The first part deals with the free vibration analysis in which the natural frequencies and mode shapes of the system are determined. In the second, the response of the system is examined and an optimum damping arrangement of overhead transmission lines is presented.

Table 4.1: Validation of natural frequencies (Hz).

Mode	T = 27.84 kN			T = 34.8 kN		
	Exp.	Anal.	Ref. [2]	Exp.	Anal.	Ref. [2]
1	-	2.3953	2.3978	-	2.6780	2.6810
2	-	4.4008	4.4157	-	4.5402	4.5482
3	-	4.9556	4.9794	-	5.4390	5.4587
4	-	7.2560	7.2961	-	8.0807	8.1245
5	-	9.3722	9.4257	-	9.6785	9.7360
6	-	9.9441	10.0120	-	10.8620	10.9407
7	12.0956	12.1634	12.2593	13.0749	13.5217	13.6277
8	14.3910	14.5642	14.6818	15.5104	16.1901	16.3273
9	16.5942	16.9498	17.1010	17.5942	18.8053	18.9801
10	19.1878	19.2874	19.4680	20.8396	21.2930	21.4932
11	21.1717	21.5661	21.7955	22.7073	23.6093	23.8500
12	23.6302	23.8280	24.0862	24.5587	25.9045	26.1695
13	25.3417	26.1201	26.4206	27.0885	28.2907	28.6355
14	27.7020	28.3588	28.7044	27.7641	30.5914	30.9642
15	29.3096	30.3524	30.7484	31.4490	32.7797	33.1814
16	31.4913	32.4137	32.8581	34.0577	35.2503	35.8622
17	33.8856	34.8828	35.3717	36.5584	38.0422	38.8023
18	36.6252	37.5991	38.1732	40.0444	41.0131	41.8586
19	39.3756	40.4481	41.0821	42.6807	44.0936	45.0250
20	42.6673	43.3869	44.1125	45.7943	47.2564	48.2937

4.3.1 Free vibration analysis

The analytical natural frequencies are determined by numerically solving for the roots of the frequency equation (Eq. (4.37)) using the bisection method in MATLAB. The first 20 natural frequencies are displayed in Table 4.1 for the two tensions (27.84 kN and 34.8 kN) employed in the experiments. The Stockbridge damper is attached at a distance L_{c_1} = 0.94 m and L_{c_1} = 0.88 m for T = 27.84 kN and T = 34.8 kN, respectively.

The first six experimental modes are not shown because the shaker used to excite the conductor is only applicable for frequencies higher than 10 Hz. A comparison of the analytical and experimental data shows very good agreement. Table 4.1 also shows the results of the finite element method from Ref. [2]. These are also in good agreement with experimentally obtained resonant frequencies, but with a 2% margin of error which is slightly higher than those of the analytical method.

The discrepancies between the experimental and analytical results could be partly attributed to the difficulty in replicating the boundary conditions during the experiments. However, it suffices to mention that not only are the analytical results more accurate than those of the finite element, the analytical procedure is less computationally intensive and has faster execution time.

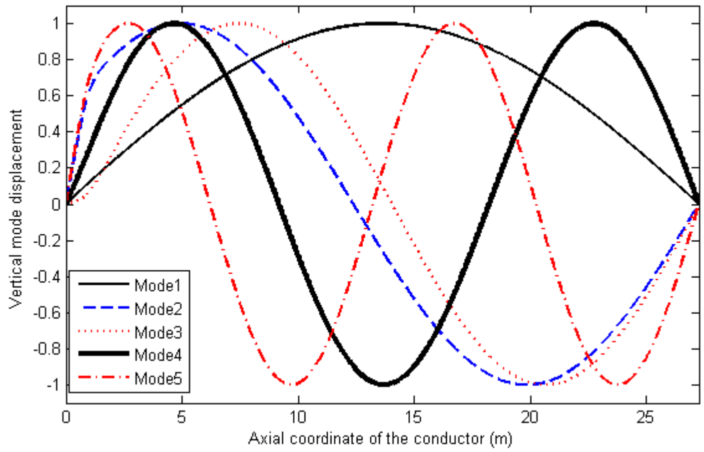

Figure 4.3: Conductor mode shapes for T = 27.84 kN.

Figs. 4.3 and 4.4 are depictions of the first five mode shapes of the conductor for T = 27.84 kN and T = 34.8 kN, respectively. Similarly, Figs. 4.5 and 4.6 depict the first five mode shapes of the damper for T = 27.84 kN and T = 34.8 kN, respectively. Figs. 4.3 and 4.4 show that the mode shapes of this system are very similar to those of a pinned-pinned beam, but the n^{th} mode of the former corresponds to the $(n-1)^{th}$ mode of the latter.

With respect to Figs. 4.5 and 4.6, the first mode of the Stockbridge damper remains relatively unchanged. This implies that the systems first mode has very little participation from the damper. The remaining four modes behave more like a cantilevered beam. In both Figs. 4.5 and 4.6, the second mode is similar to the third except that the former deflected upward and the latter downward. Note that only the right segment of the messenger (L_{m_1}) is excited by the second and third modes. This implies that the second and third modes of the system must be closer to that of the right-side segment of the messenger.

In light of the good agreement between the analytical and experimental results, the model is used to parametrically investigate the influence of the damper characteristics and location on the system natural frequencies. Unless otherwise specified, the set of material properties are as tabulated in Table 2.1 and the damper is attached at a distance L_{c_1} = 0.94 m. The conductor tension T = 27.84 kN is employed in the remainder of the numerical analysis.

At the first stage of the parametric studies, the effect of the damper counterweights on the natural frequency is examined. The mass of each counterweight is varied from 0.5

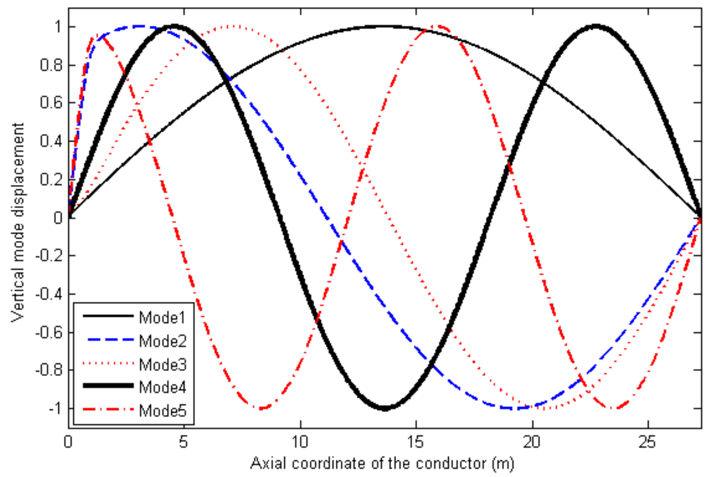

Figure 4.4: Conductor mode shapes for $T = 34.8$ kN.

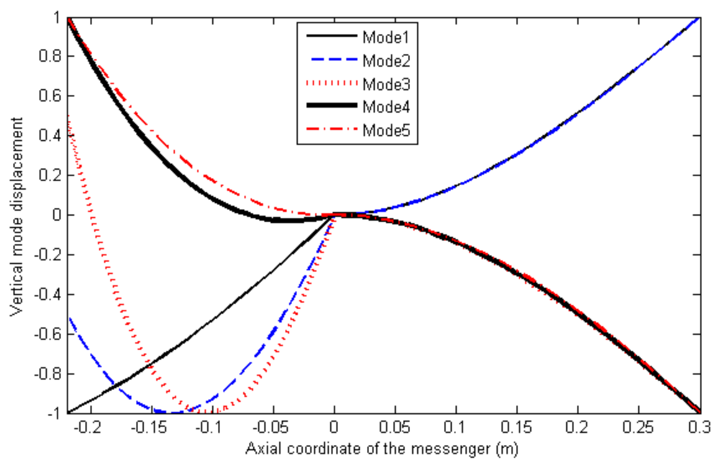

Figure 4.5: Messenger mode shapes for $T = 27.84$ kN.

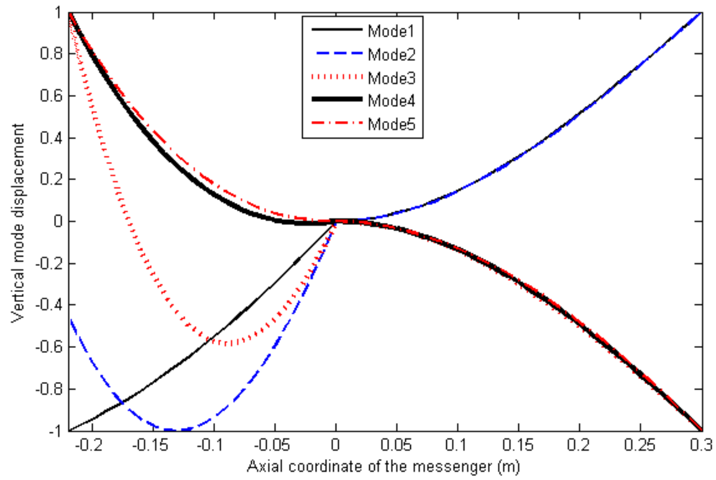

Figure 4.6: Messenger mode shapes for $T = 34.8$ kN.

to 4.5 kg. The results are tabulated in Table 4.2. As expected, the natural frequencies generally increase with decreasing total mass. However, the fundamental frequency remains unchanged, which indicates that the mass of the counterweight has minimal or no effect on the first mode.

The length of the messenger on either side is varied from 0.1 to 2 m in order to examine the role of the messenger on the system natural frequencies. The obtained frequencies are tabulated in Table 4.3. It is observed that the natural frequencies generally decrease with increasing total length of the messenger as expected. This decrease in the natural frequency is significant even for the fundamental mode.

The system natural frequencies for varying messenger flexural rigidity are tabulated in Table 4.4. The results show that the system natural frequencies generally increase with increasing flexural rigidity of the messenger. The role of the distance separating the conductor and the messenger (i.e., length of the rigid link, h) is inferred from the results tabulated in Table 4.5. It is observed that the natural frequencies decrease with increasing rigid link length. This decrease in the natural frequencies is less significant for the fundamental mode. Hence, the first mode is again dominated by the conductor characteristics. Table 4.6 shows the influence of the location of the Stockbridge damper on the system natural frequencies. The location of the damper affect all five modes, but with no obvious trend.

Table 4.2: Effect of counterweight masses on natural frequencies (Hz).

m_2 (kg)	Mode	m_1 (kg)				
		0.5	1.5	2.5	3.5	4.5
0.5	1	2.40020	2.39890	2.39730	2.39550	2.3932
	2	4.79960	4.77770	4.69650	4.36200	3.9500
	3	7.1849	6.3439	5.2991	4.9421	4.8820
	4	9.0107	7.3384	7.2819	7.2706	7.2658
	5	9.7874	9.6910	9.6842	9.6817	9.6804
1.5	1	2.3998	2.3985	2.3969	2.3950	2.3927
	2	4.7955	4.7730	4.6905	4.3573	3.9473
	3	7.1608	6.3327	5.2977	4.9415	4.8803
	4	8.9226	7.3285	7.2665	7.2540	7.2487
	5	9.4923	9.3299	9.3221	9.3194	9.3180
2.5	1	2.3994	2.3981	2.3965	2.3946	2.3923
	2	4.7900	4.7667	4.6823	4.3512	3.9440
	3	7.0752	6.3089	5.2958	4.9406	4.8778
	4	7.9269	7.2867	7.2046	7.1883	7.1814
	5	9.0748	7.9465	7.9421	7.9410	7.9405
3.5	1	2.3989	2.3976	2.3960	2.3941	2.3917
	2	4.7818	4.7574	4.6708	4.3432	3.9399
	3	6.6605	6.2365	5.2925	4.9394	4.8742
	4	7.3770	7.4215	6.7693	6.7496	6.7420
	5	9.0535	9.7449	7.4037	7.4005	7.3991
4.5	1	2.3984	2.3971	2.3955	2.3936	2.3912
	2	4.7688	4.7428	4.6534	4.3323	3.9347
	3	6.0751	5.9722	5.2862	4.9374	4.8684
	4	7.2875	6.5338	6.1599	6.1329	6.1247
	5	9.0472	7.3791	7.3444	7.3377	7.3348

Table 4.3: Effect of the messenger length on natural frequencies (Hz).

L_{m_2} (m)	Mode	L_{m_1} (m)				
		0.1	0.5	1.0	1.5	2.0
0.1	1	2.3974	2.2127	0.8142	0.4441	0.2879
	2	4.7748	2.4302	2.4014	2.4006	2.4003
	3	7.0904	4.8114	4.8021	4.8000	4.7963
	4	9.2496	7.2121	7.2000	7.1905	5.9484
	5	11.2051	9.6054	9.5864	8.7283	7.2106
0.5	1	2.3978	2.2131	0.8142	0.4441	0.2879
	2	3.3700	2.4303	2.4017	2.4010	2.4006
	3	4.7838	3.3705	3.3705	3.3705	3.3705
	4	7.1251	4.8181	4.8093	4.8073	4.8037
	5	9.3573	7.2330	7.2220	7.2132	5.9493
1	1	1.2277	1.2277	0.8142	0.4441	0.2879
	2	2.3982	2.2132	1.2278	1.2277	1.2277
	3	4.7821	2.4305	2.4021	2.4014	2.4010
	4	7.1236	4.8170	4.8080	4.8060	4.8025
	5	9.3550	7.2323	7.2212	7.2124	5.9494
1.5	1	0.6669	0.6669	0.6669	0.4441	0.2879
	2	2.3982	2.2133	0.8142	0.6669	0.6669
	3	4.7821	2.4305	2.4022	2.4014	2.4010
	4	7.1225	4.8169	4.8080	4.8060	4.8025
	5	9.1100	7.2316	7.2206	7.2118	5.9494
2	1	0.4303	0.4303	0.4303	0.4302	0.2879
	2	2.3982	2.2133	0.8142	0.4441	0.4303
	3	4.7819	2.4305	2.4022	2.4014	2.4010
	4	6.1271	4.8168	4.8079	4.8059	4.8023
	5	7.1264	6.1282	6.1282	6.1282	5.9493

Table 4.4: Effect of the messenger flexural rigidity on natural frequencies (Hz).

Mode	$E_m I_m$ (N/m^2)				
	0.1	1.0	10.0	100.0	1000.0
1	0.2879	0.8401	2.3789	2.3960	2.3964
2	0.5584	1.7632	2.6331	4.7469	4.7648
3	1.4704	2.4011	4.8047	6.6457	7.0474
4	2.1441	4.5985	5.5119	7.7690	9.1409
5	2.4025	4.8340	7.2300	9.8956	11.1076
6	4.8084	6.6791	9.6239	12.2451	13.2615
7	7.2255	7.2749	11.9507	14.4064	15.6416
8	9.6584	9.6814	13.7546	15.7283	18.1520
9	12.1122	12.1347	15.0584	17.5826	20.7434
10	14.5919	14.6161	17.1461	19.9560	23.3944
11	17.1023	17.1291	19.1027	22.4036	26.0685
12	19.6471	19.6788	20.7019	24.8682	27.9504
13	22.2253	22.2699	22.8631	27.3596	29.1293
14	24.6928	24.9075	25.3697	29.9151	31.8609
15	25.2733	27.5963	28.0008	32.5680	34.7620
16	27.6107	30.3412	30.7104	35.3305	37.7451
17	30.3395	33.1465	33.4880	38.1991	40.8034
18	33.1390	36.0166	36.3326	41.1655	43.9358
19	36.0042	38.9553	39.2457	44.2177	47.1413
20	38.9355	41.9662	42.2303	47.3172	50.4171

Table 4.5: Effect of clamp height on natural frequencies (Hz).

Mode	h (m)				
	0.01	0.5	1.0	1.5	2.0
1	2.3950	2.3940	2.3907	2.3840	2.3713
2	4.3574	4.3452	4.2975	4.1569	3.7714
3	4.9415	4.9409	4.9385	4.9307	4.8745
4	7.2541	7.2371	7.0962	5.9075	5.0666
5	9.3194	9.3167	8.5572	7.4561	7.3783
6	9.9127	9.8458	9.3371	9.3269	9.3257
7	12.1632	12.0116	10.3493	10.1209	10.0857
8	14.5646	14.2654	12.5256	12.4019	12.3754
9	16.9490	16.4393	14.8943	14.8146	14.7947
10	19.2828	18.5509	17.2439	17.1882	17.1731
11	21.5550	20.3939	19.4821	19.4509	19.4421
12	23.8115	21.7886	21.6128	21.6056	21.6034
13	26.1005	23.8115	23.8115	23.8115	23.8115
14	28.3314	26.1456	26.1265	26.1246	26.1240
15	30.3150	28.3625	28.3521	28.3509	28.3505
16	32.3899	30.3337	30.3287	30.3281	30.3278
17	34.8730	32.5772	32.5357	32.5300	32.5281
18	37.5963	35.1854	35.1246	35.1158	35.1128
19	40.4486	37.9646	37.8995	37.8898	37.8866
20	43.3881	40.8243	40.7631	40.7538	40.7507

Table 4.6: Effect of damper location on natural frequencies (Hz).

Mode	L_{c_1}				
	$L_c/100$	$L_c/10$	$L_c/6$	$L_c/4$	$L_c/2$
1	2.3999	2.3614	2.3049	2.2288	2.1201
2	4.5444	4.0203	3.9004	3.9544	4.7092
3	4.8621	5.1583	5.3589	5.4976	4.8423
4	7.2383	7.1893	7.0885	7.0926	7.0949
5	9.6696	8.8023	9.0209	9.6194	9.6104
6	12.1225	10.3922	10.7470	12.2225	9.8972
7	14.5983	14.5833	12.2794	14.5632	12.4048
8	17.0988	16.9846	14.6115	17.0170	14.6111
9	19.6190	19.5491	17.0247	19.6732	16.8610
10	22.1239	22.2159	19.2416	21.7401	19.6731
11	24.3187	24.8734	21.6055	23.9078	21.5417
12	25.6735	25.8659	24.3172	26.7988	24.8785
13	27.8490	27.8460	27.0319	27.9871	25.7063
14	30.4769	30.5062	27.7439	30.3646	28.3762
15	33.1860	32.6745	30.3640	32.9017	30.3669
16	35.7006	34.7148	33.1236	34.7440	32.4379
17	37.1094	37.4496	34.7936	38.0303	36.0100
18	39.3438	40.4795	37.3504	41.5599	37.0541
19	42.2444	43.6002	40.5902	42.1458	41.4734
20	45.2944	46.6673	42.2288	45.5969	42.0975

4.3.2 Forced vibration analysis

In this numerical analysis, the same material and geometric properties of the tested conductor and damper are employed and the conductor tension is assumed to be 20% RTS (27840 N). The time response of the bare conductor with and without self-damping is depicted in Fig. 4.7. The damping coefficient of the conductor is obtained by curve-fitting the experimental data. It is observed that the vibration amplitude of the conductor without self-damping can be up to eight times higher than that with conductor self-damping. This implies that ignoring conductor self-damping can lead to erroneous prediction of the response of the conductor. Hence the damping coefficient of the conductor is included in subsequent numerical simulations.

In Figs. 4.8 and 4.9, the validity of the present analytical model is examined using the experimental results. The former figure is the frequency response curve of the bare conductor while the latter depicts the frequency response curve of the conductor with a Stockbridge damper located at $L_{c_1} = 0.94$ m. Both figures show good agreement between the analytical and experimental results. The present analytical results are also compared to the finite element results and the energy balance method. The results indicate that the present analytical results agree better with the experiments than those of the finite

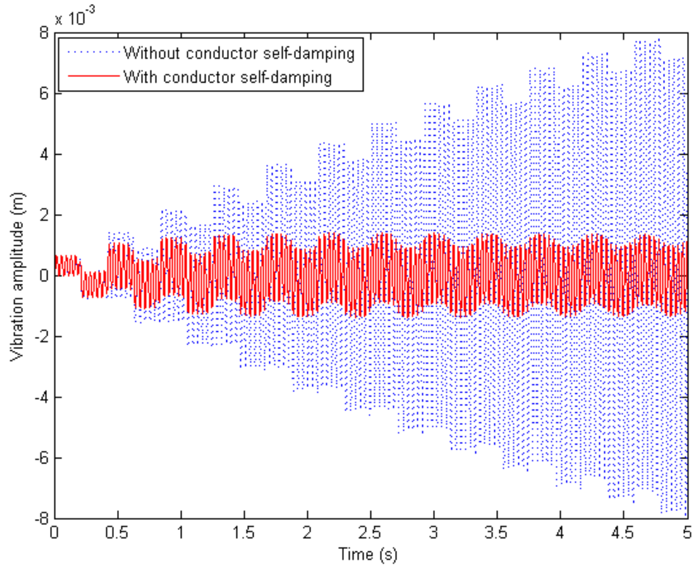

Figure 4.7: Vibration response of the conductor with and without self-damping for F_0 = 22.5 N, f = 26.5 hz, $\zeta = 0.006$.

element and energy balance method.

As mentioned in the literature review, it is observed from Fig. 4.8 that the energy balance method overestimates the response of the bare conductor while Fig. 4.9 indicates that the energy balance underestimates the response of the loaded conductor. The results in Figs. 4.8 and 4.9 also show that the ratio of vibration amplitude over the excitation force significantly decreases with increasing frequency. However, the vibration response of the conductor with attached Stockbridge damper is much lower than that of the bare conductor. For an excitation frequency of f = 26.5 Hz, Fig. 4.10 shows the time response curve of the conductor for various damper location. The vibration amplitude is significantly reduced by attaching a Stockbridge damper at the mid-span.

4.4 Summary

The conductor was modeled as a beam with a tensile load, but the Stockbridge damper was modeled as an in-span beam with tip-mass at each end. Hamilton's principle was employed to derive the governing equations of motion and boundary conditions. Explicit expressions were presented for the orthogonality conditions, mode shapes, and characteristics equation. Natural frequencies of the conductor with and without damper were obtained and the results were validated using experimental results; very good agreement

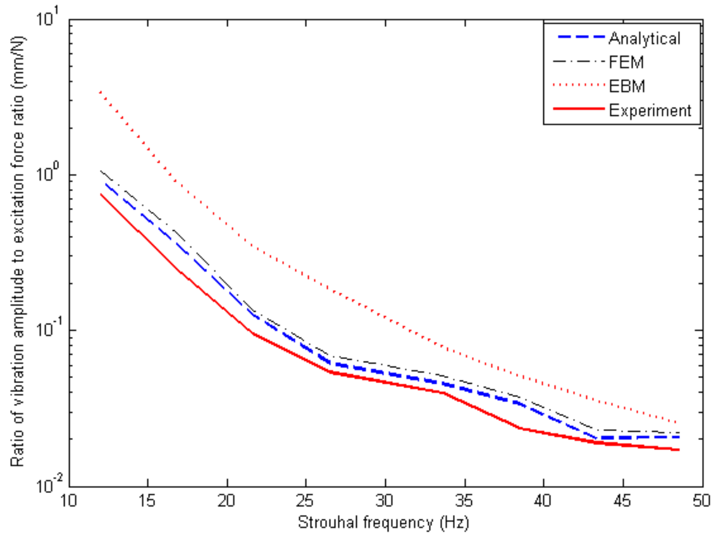

Figure 4.8: Validation for the bare conductor.

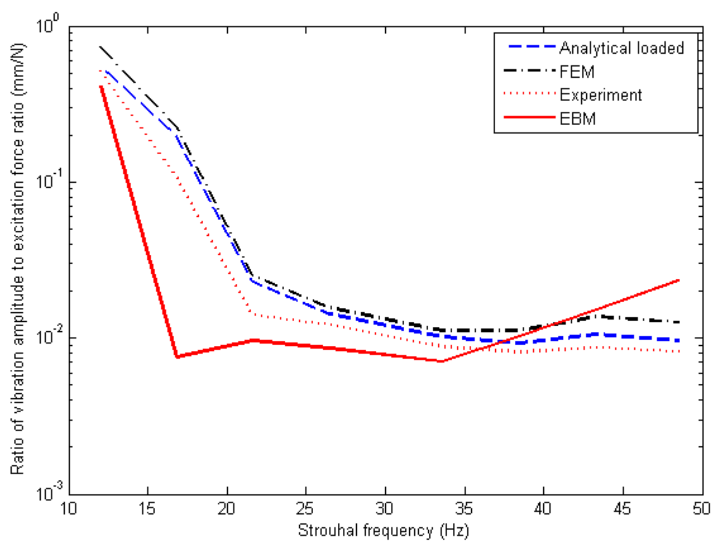

Figure 4.9: Validation for the loaded conductor.

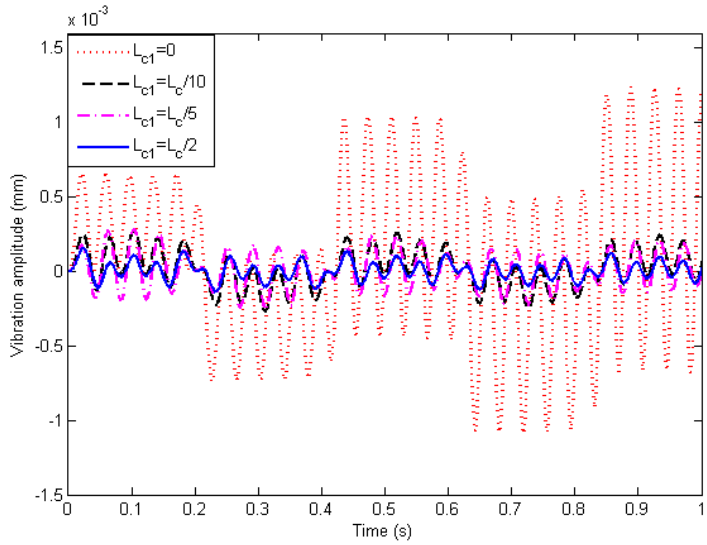

Figure 4.10: Efffect of damper location for $F_0 = 22.5$ N, $f = 26.5$ hz, $\zeta = 0.006$.

was observed with a maximum percentage error of 4%. The mass of the counterweight, flexural rigidity of the messenger, clamp height, and location of the damper were all found to be factors that can impact the natural frequency of the conductor-damper system.

The vibration response of the conductor with and without dampers was determined using modal analysis method. The results were also validated experimentally. It was demonstrated that the present method is more accurate than the energy balance method for predicting the vibration response of a single conductor with dampers. The results of the numerical examples indicated that the location of the damper is a major factor in controlling the vibration response of the conductor. This important role motivates the determination of the optimal damper location which is investigated in the following chapter.

Chapter 5

Design Optimization of Damper Location

5.1 Introduction

The model in the preceding chapter is employed to conduct the damper location optimization since it is more thorough and accurate than the model presented in chapter 3. An explicit expression of the loop length is presented. Based on a heuristic process, the first optimization is conducted by determining the minimum mid-span vibration displacement while varying the location of the damper throughout the loop length. This heuristic algorithm is then validated using the Matlab routine *fmincon*. The orientation of the counterweights is investigated to obtain the best performance of the damper. A typical transmission line span length is then utilized to examine the symmetric and asymmetric damping arrangement. This damper location optimization is limited to two dampers per span which is usually the case for a suspension-suspension span of up to 500 m span length.

5.2 Damper location optimization

For a simply supported beam, the maximum vibration amplitude is expected to occur at mid-span provided that the excitation frequency is closer to an odd mode. As such, the optimal location is expected to be the mid-span. However, field investigations have shown that a damper located at mid-span or further from the suspension clamp has increased tendency to suffer early fatigue failure due to galloping. Therefore, it has been recommended to position the damper closer to suspension clamps between 70 to 80% of the loop length corresponding to the highest wind speed (7 m/s) [1]. This recommendation also facilitates the installation of the dampers by construction workers because the damper location is within a few meters from towers.

5.2.1 Heuristic algorithm

An intent of this work is to revisit the recommendation provided in [1] for determining the optimal damper location by considering not only high wind speed but also medium (4 m/s) and low wind speed (2 m/s). This is achieved by finding the minimum value of the conductor response while varying the location of one damper throughout the loop length corresponding to wind speeds of 2, 4, and 7 m/s.

The expression of the loop length is obtained by equating the natural frequency of the bare conductor to that of the Strouhal frequency (excitation frequency) and solving for $\frac{L_\mathrm{c}}{n}$. The derivation is shown below.

The natural frequency of the bare conductor was obtained in Ref. [2] and is given as

$$f_\mathrm{n} = \frac{n}{2L_\mathrm{c}}\sqrt{\frac{T}{m_\mathrm{c}} + \left(\frac{n\pi}{L_\mathrm{c}}\right)^2 \frac{E_\mathrm{c}I_\mathrm{c}}{m_\mathrm{c}}} \tag{5.1}$$

where n is the mode number. And the excitation frequency is given by

$$f_\mathrm{s} = 0.2\frac{v}{D} \tag{5.2}$$

Equating Eq. (5.1) to Eq. (5.2) and solving for $\frac{L_\mathrm{c}}{n}$, which is the loop length and denoted by λ yield

$$\lambda = \frac{1}{2f_\mathrm{s}}\sqrt{\frac{T}{m_\mathrm{c}} + \left(\frac{\pi}{\lambda}\right)^2 \frac{E_\mathrm{c}I_\mathrm{c}}{m_\mathrm{c}}} \tag{5.3}$$

Squaring both sides of Eq. (5.3) and isolating λ yields

$$\lambda^4 - \frac{T}{4m_\mathrm{c}f_\mathrm{s}^2}\lambda^2 - \pi^2\frac{E_\mathrm{c}I_\mathrm{c}}{4m_\mathrm{c}f_\mathrm{s}^2 = 0} \tag{5.4}$$

After some algebraic manipulation, the loop length can be expressed as

$$\lambda = \sqrt{\frac{1}{2}\left(\frac{T}{4m_\mathrm{c}f_\mathrm{s}^2} + \sqrt{\left(\frac{T}{4m_\mathrm{c}f_\mathrm{s}^2}\right)^2 + \pi^2\frac{E_\mathrm{c}I_\mathrm{c}}{f_\mathrm{s}^2}}\right)} \tag{5.5}$$

The numerical simulation in this subsection is also based on the tested conductor and

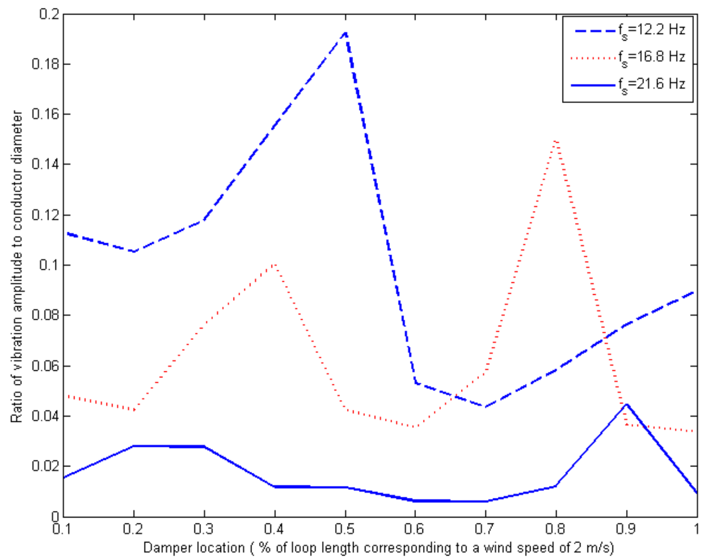

Figure 5.1: Optimal damper location for lower frequencies excitation

damper parameters. The tension is assumed to be 28.024 kN and the applied force is F=20 N. The calculated loop length corresponding to the lowest, medium, and highest wind speed are determined to be 4.6, 2.3, and 1.32 m, respectively. The optimization of the damper location corresponding to the low wind speed is depicted in Fig. 5.1. The results indicate that the optimal damper location for lower frequencies falls between 60 to 70% of the loop length corresponding to a wind speed of 2 m/s.

In Fig. 5.2 the optimization is based on medium excitation frequencies. The results show that the vibration amplitude of the conductor is minimum when the damper is positioned between 80 to 90% of the loop length corresponding to a wind speed of 4 m/s. Fig. 5.3 shows the optimization of the damper location based on high frequencies. The results indicate that the optimal location should lie between 85 to 95% corresponding to a wind speed of 7 m/s.

5.2.2 Matlab built-in function

The optimization of the damper location herein is based on the Matlab built-in routine, *fmincon*. This is a constrained optimization routine. The approach is to determine the location of the damper corresponding to the minimum mid-span vibration displacement (Eq. (4.57)) throughout the whole range of excitation frequency. The optimality criterion

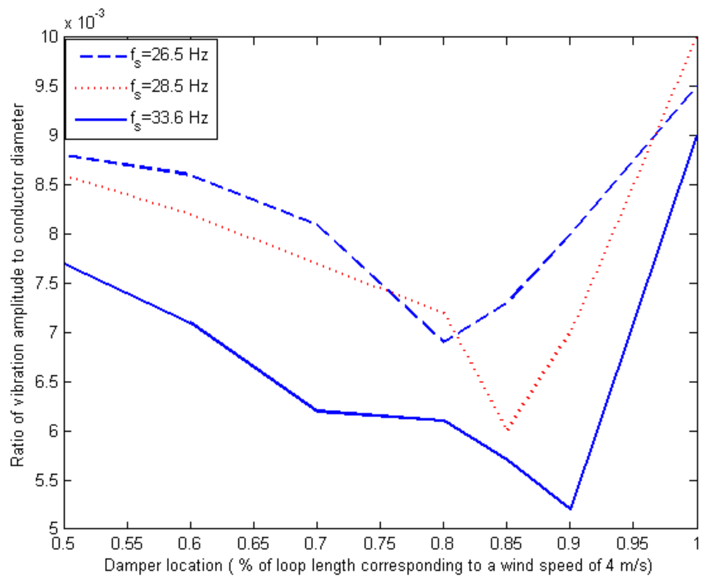

Figure 5.2: Optimal damper location for medium frequencies excitation

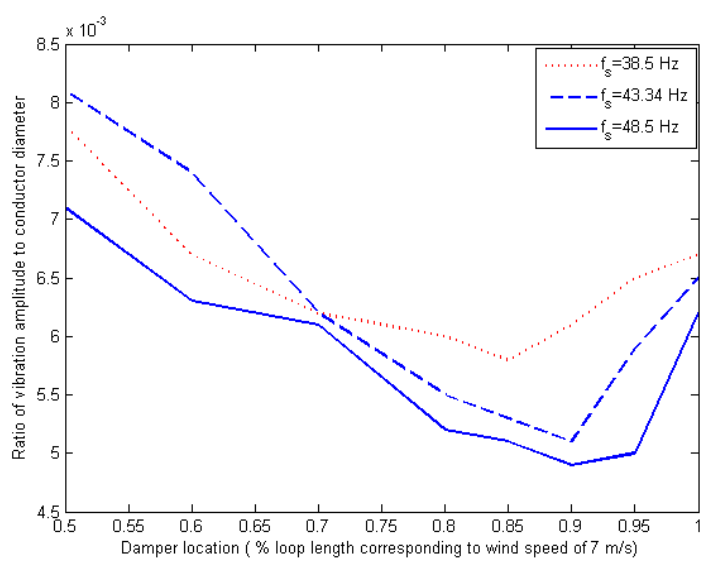

Figure 5.3: Optimal damper location for higher frequencies excitation

is defined as

$$\text{Minimize}\left(w_{\text{ci}} = \sum_{r=1}^{\infty} q_{\text{r}}(t) Y_{\text{ci}}^{(r)}(L_{\text{c}}/2)\right) \tag{5.6}$$

subject to the constraints

$$\begin{aligned} 0 &\leq L_{\text{c1}} \leq \lambda_{\text{low}} \\ 0 &\leq L_{\text{c2}} \leq (L_{\text{c}} - \lambda_{\text{low}}) \end{aligned} \tag{5.7}$$

where λ_{low} is the loop length corresponding to low wind speeds. The above contraints are use to facilitate the easy installation of the damper. Given any initial guess of L_{c1} and L_{c2}, the routine *fmincon* finds the optimal damper location in such way that the objective function in Eq. (5.6), subject to constraints given in Eq. (5.7) is minimized. The option of using the gradient or Hessian is not provided hence by default Matlab uses the trust-region-reflective method, a finite difference approximation method, to solve the problem.

Because the purpose of this subsection is to verify the proposed optimization algorithm, the numerical example is based on the same parameters (i.e., tested conductor with span length of 27.25 m). The initial guess for L_{c1} and L_{c2} are taken to be 1.5 and 1 m from each end, respectively. The optimization is conducted over the whole range of the vibration frequency (7 to 50 Hz). After several iterations, the *fmincon* command returns the optimal damper locations, $L_{\text{c1}} = 2.57$ m and $L_{\text{c2}} = 1.2$ m from each end.

The optimization results obtained using the *fmincon* command indicate that L_{c1} is at 55.8% of the loop length, corresponding to a wind speed of 2 m/s, and that L_{c2} is at 90.9% of the loop length corresponding to wind speed of 7 m/s. Comparing these results to those obtained using the heuristic algorithm, it is observed that L_{c2} falls within the anticipated range of optimal damper location while L_{c1} does not fall within the anticipated range of optimal damper location for low vibration frequency. As such, based on this numerical example the optimal damper location range for low vibration frequencies should be extended to fall between 50 to 70% of the loop length corresponding to a wind speed of 2 m/s.

A further comparison between the proposed algorithm and *fmincon* command is demonstrated in the numerical simulations for a typical transmission line span length.

5.2.3 Orientation of the counterweight

To further investigate the optimal performance of the damper, the orientation of the damper counterweights is examined to determine the difference of the damper perfor-

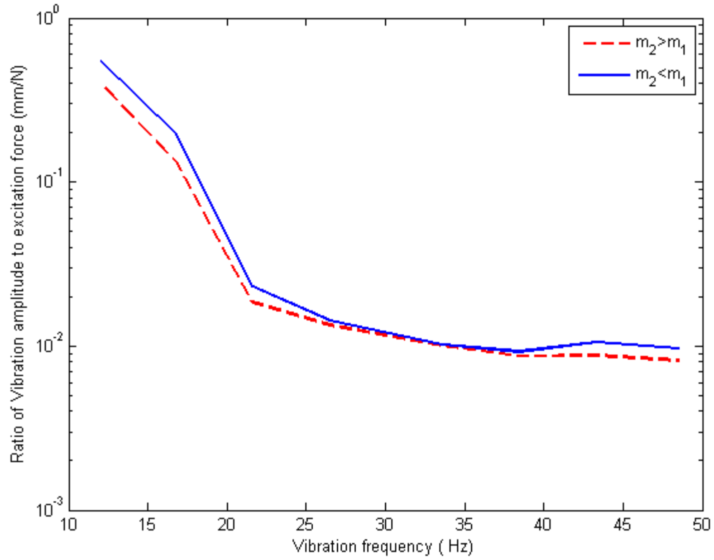

Figure 5.4: Difference in the damper performance based on the orientation of the counterweight

mance when the bigger mass is oriented toward the suspension clamp (span-ends) and when it is oriented toward the span center. The results are plotted in Fig. 5.4 and indicate that facing the bigger mass toward the suspension clamp improves the effectiveness of the Stockbridge damper while facing the bigger mass toward the mid-span decreases the effectiveness of the Stockbridge damper.

5.3 Numerical analysis for a typical transmission line

A span length of $L_c = 366$ m is selected for the next numerical simulation. This selection ensures that the ratio of the conductor sag to span length is typical of existing transmission lines (i.e., 0.03). The equivalent wind force $F_0 = 370.9$ N. It should be noted that the severity of aeolian vibration is often measured by the bending strain ($\epsilon = \pi DYf\sqrt{(}m/T))$, which is used to examine the tendency of the conductor to experience fatigue failure.

5.3.1 Conductor with one damper

Fig. 5.5 shows the nondimensional response of the conductor (with respect to conductor diameter) with and without damper for various forcing frequencies. This figure indicates that the conductor response reduces when the Stockbridge damper is attached. The

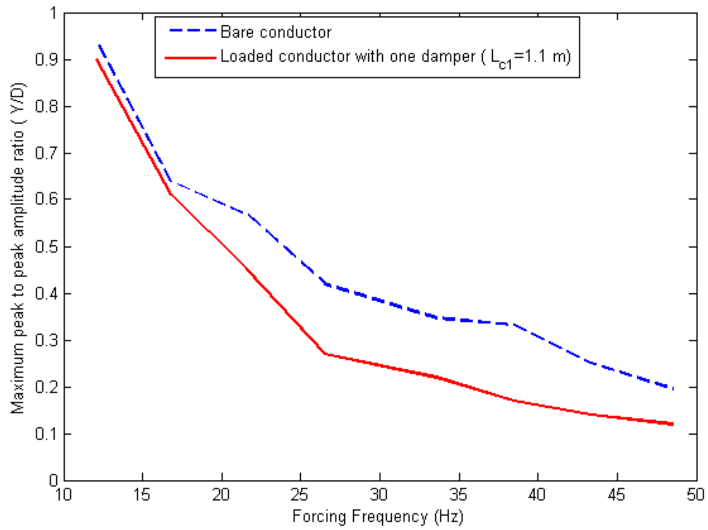

Figure 5.5: Vibration response of a typical span length of transmission line with and without a damper

bending strain is plotted against the forcing frequency in Fig. 5.6 for a conductor with and without a damper. Guided by suggested safe bending strain of 200 $\mu\frac{m}{m}$ in the literature [24], it is evident that the calculated bending strain for a bare conductor and that of a conductor with one damper exceed the strain limit.

It is observed that a minimum of two dampers are placed close to each end-span to control the vibration in a typical transmission line with long span length. This can be achieved by either symmetric or asymmetric damping arrangement. In the next numerical analysis both damping arrangements are examined and then a comparison of the two is conducted.

5.3.2 Symmetric arrangement

In the symmetric damping arrangement, the numerical simulation is established using five scenarios. The first two scenarios are based on the recommendation of [1] and the last three scenarios are based on the present optimal damper location heuristic. In the first and second scenario each damper is placed respectively at 70 and 80% of the loop length, corresponding to highest wind speed. The results are illustrated in Fig. 5.7. A better damper performance is observed when the damper is placed at 80% of the loop length which corresponds to highest wind speed.

The last three scenarios are depicted in Fig. 5.8. The third scenario is to place each

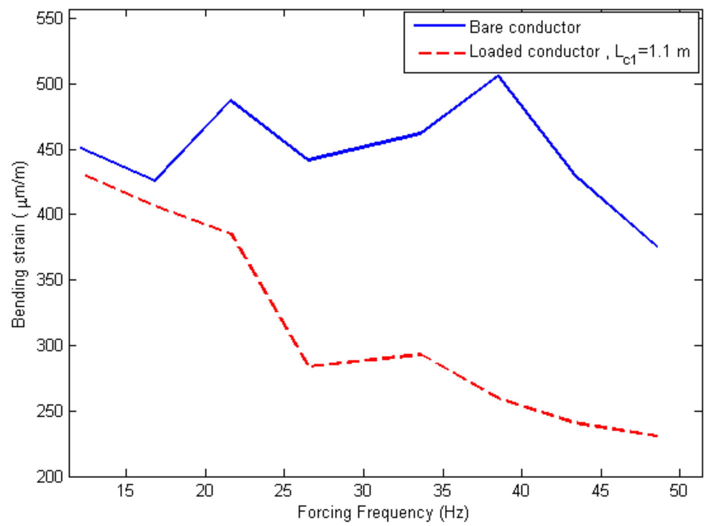

Figure 5.6: Bending strain of a typical span length of transmission line with and without dampers

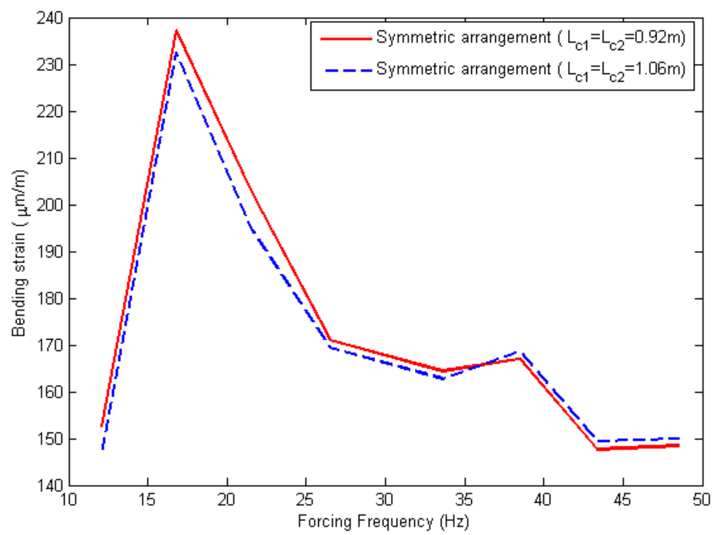

Figure 5.7: Bending strain in symmetrically located dampers using [1] recommendation

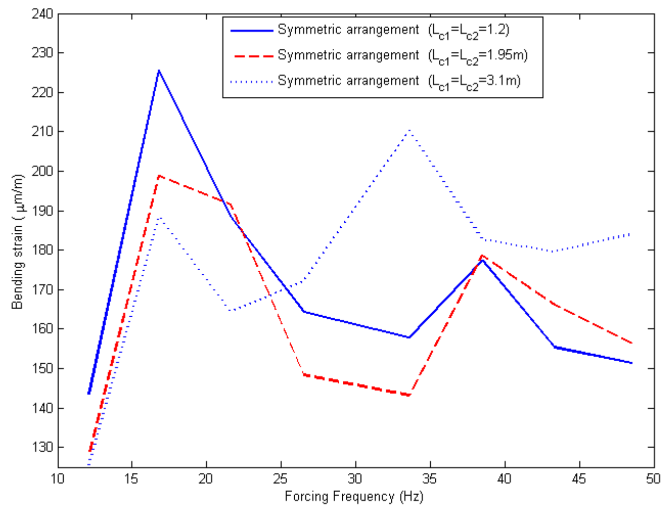

Figure 5.8: Damper performance based on symmetric arrangement from the heuristics algorithm

damper at 90% of the loop length measured from the suspension clamp, corresponding to high wind speed. In the fourth scenario each damper is placed at 85% of the loop length measured from the suspension clamp corresponding to medium wind speed. In the fifth scenario each damper is placed at 67% of the loop length measured from the suspension clamps which corresponds to low wind speed.

As expected, Fig. 5.8 indicates that each scenario fares best in the range of frequencies corresponding to its optimal location. For example the third scenario is found to be the best to control high frequencies, the fourth scenario is the best for controlling medium vibration frequencies, and the fifth scenario is the best for damping low vibration frequencies.

To further investigate the optimal damper location, each of three scenarios of the heuristic method (i.e., third, fourth, and fifth scenario) are compared to the best scenario of Ref.[1] (i.e., the second scenario). The results are depicted in Figs. 5.9 to 5.11. The same conclusions observed from Fig. 5.8 can be deduced in that each scenario performs better in the frequency range corresponding to its optimal location. Of the five scenarios, the second and third scenarios are in general the best. This is an indication that the best location of the damper for a symmetric damping arrangement should involve placing the damper between 80 to 90% of the loop length which corresponds to the high wind speed.

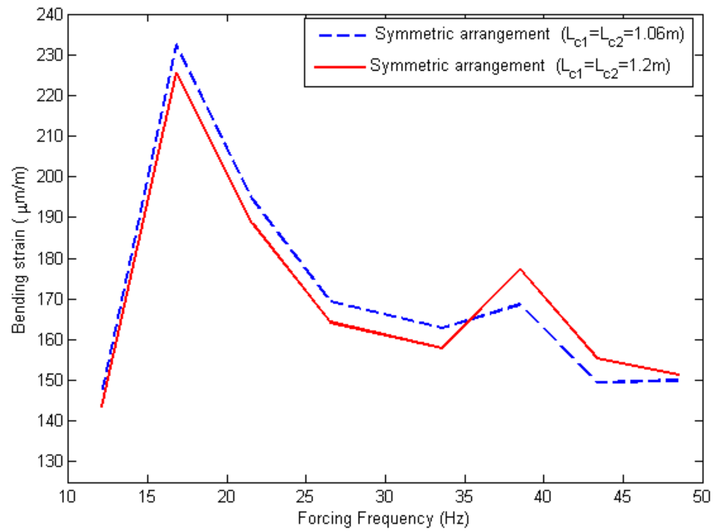

Figure 5.9: Second scenario (damper location at 80% loop length corresponding to high frequencies) vs. third scenario (damper location at 90% loop length corresponding to high frequencies)

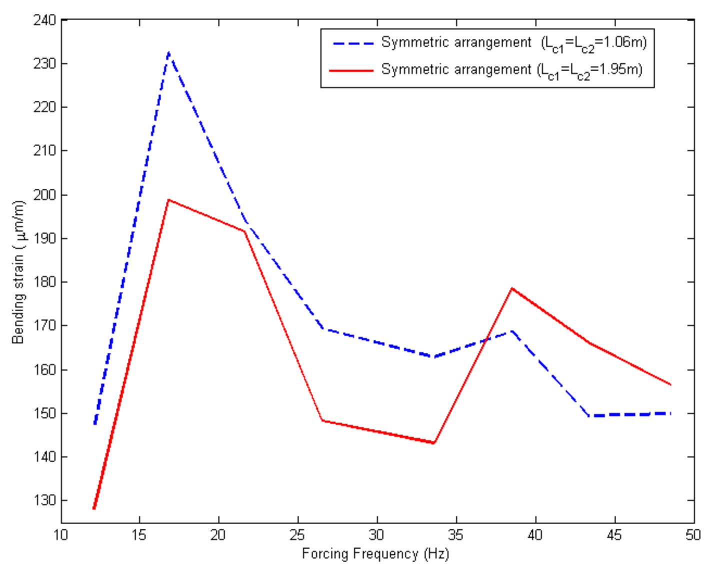

Figure 5.10: Second scenario (damper location at 80% loop length corresponding to high frequencies) vs. fourth scenario (damper location at 85% loop length corresponding to medium frequencies)

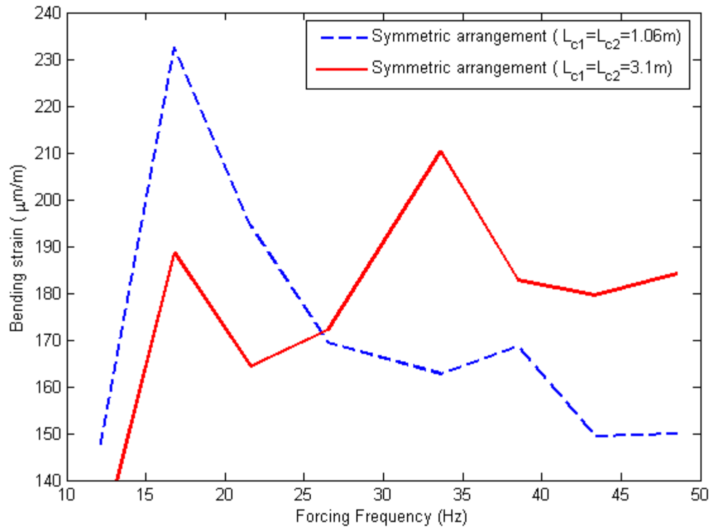

Figure 5.11: Second scenario (damper location at 80% loop length corresponding to high frequencies) vs. fifth scenario (damper location at 67% loop length corresponding to low frequencies)

5.3.3 Asymmetric arrangement

The asymmetrical arrangement is based on three scenarios. The first scenario is to place one damper at 67% of the loop length corresponding to the low wind speed and placing another damper at 90% of the loop length corresponding to the high wind speed. The second scenario is to place one damper at 85% of the loop length corresponding to the medium wind speed and place another at 90% of the loop length corresponding to the high wind speed. The third scenario is to place one damper at 85% of the loop length corresponding to the medium wind speed and another damper at 67% of the loop length corresponding to the lowest wind speed. The results are depicted in Fig. 5.12. Of the three scenarios, the first scenario is found to be the best.

5.3.4 Symmetric vs. asymmetric arrangement

In this numerical analysis, a comparison between the symmetric and asymmetric damping arrangement is examined. The results are illustrated in Fig. 5.13. These results clearly indicate that all three scenarios of the asymmetric damping arrangement perform better than the best scenario of the symmetric damping arrangement. The symmetric arrangement shows very good control for high frequencies, but poor control for low frequencies. All three asymmetric damping arrangement scenarios show very good control

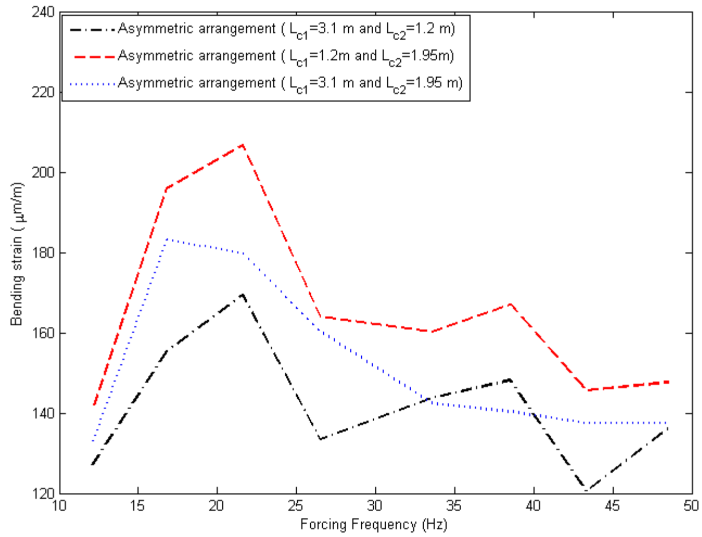

Figure 5.12: Damper performance based on an asymmetric arrangement

for both low and high excitation frequencies. Hence the asymmetric damping arrangement is recommended for the control of aeolian vibration. Therefore, an optimal damping arrangement would involve one damper located between 50 to 70% of the loop length corresponding to the low wind speed and another damper located between 85 to 95% of the loop length corresponding to the high wind speed.

5.3.5 Heuristic algorithm vs. Matlab built-in routine

The Matlab built-in routine *fmincon* is compared to the heuristic algorithm for the typical transmission line span length (i.e., 366 m) . The optimal damper location for the heuristic algorithm is obtained to be 3.1 m and 1.2 m from each end. The results obtained using the *fmincon* routine indicate that the optimal damper location is 2.7 m and 1.15 m from each end. It is noted that the results of the *fmincon* routine translate to 58.6% of the loop length corresponding to 2 m/s wind speed and 87.1% of the loop length corresponding to 7 m/s wind speed, respectively. This result is an indication that the proposed algorithm agrees with the *fmincon* command.

A further illustration of this corroboration is demonstrated in Fig. 5.14 which shows a negligible difference between the two methods. As such, it can be concluded that the proposed heuristic algorithm is valid for the purpose of optimizing the damper location.

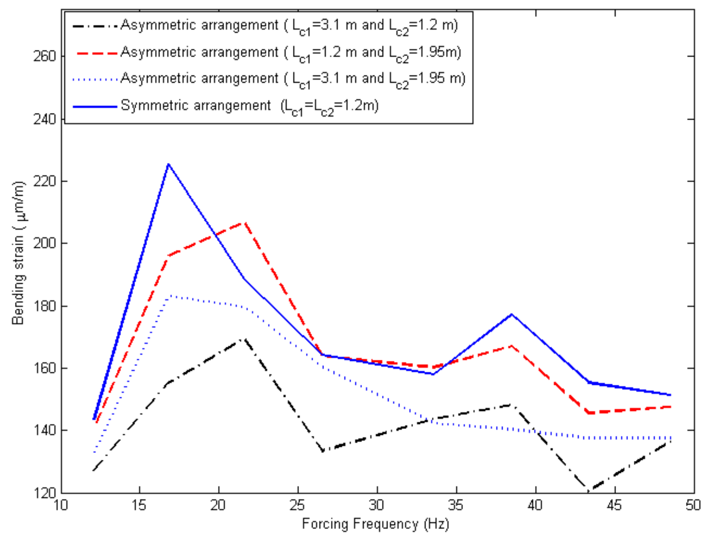

Figure 5.13: Symmetric vs. asymmetric arrangement

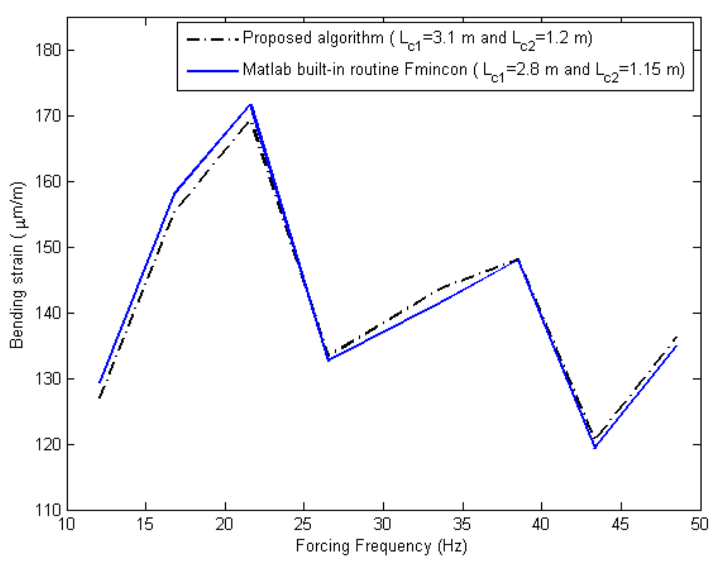

Figure 5.14: Proposed heuristic algorithm vs. Matlab optimization using *fmincon* routine

5.4 Summary

The state-of-the art of damper placement is based on a rule of thumb. This was revisited in this chapter by not only using highest wind speed but also by including the low and medium wind speeds. An explicit expression of the loop length was presented. A heuristic process was first used to determine the optimal damper location. The results were compared to those obtained using a Matlab optimization routine and very good agreement was observed.

Asymmetric and symmetric damping arrangements were examined. The results showed that asymmetric arrangement was better for controlling conductor vibration. It was demonstrated that the optimal location of the damper involved placing one damper between 50 to 70 % of the loop length corresponding to low wind speed (2 m/s) and another damper 85 to 95% of the loop length corresponding to high wind speed (7 m/s). It was also observed that orientating the bigger counterweight toward the suspension clamp (i.e., toward the tower) improves the effectiveness of the Stockbridge damper.

Chapter 6

Conclusion and Future Work

6.1 Summary

Overhead transmission line vibration is one of the major causes of power outages. A method to control these vibrations is to attach Stockbridge dampers on the conductor. The performance of the damper is significantly dependent on its characteristics and location. Hence it is necessary to develop mathematical models that can be used to predict the conductor dynamics and determine optimal location of dampers.

The energy balance principle (EBP) and the impedance methods are the two common methods used to study transmission line vibrations. Both methods are easy concepts to implement with little computation. However, they do not account for some critical parameters such as the flexural rigidity of the conductor and messenger, and the mass of the damper. Another major drawback of these two approaches is the limitation to only one-way coupling between the conductor and damper. Specifically, the dynamics of the damper influenced that of the conductor but not the converse.

These shortcomings were addressed in the present dissertation using two analytical models. In the first analytical model, the conductor was modeled as an Euler-Bernoulli beam subjected to an axial load and the Stockbridge damper was reduced to an equivalent discrete mass-spring-mass and viscous damping system. The viscous damping of the Stockbridge damper was determined experimentally. The validity of the formulation was demonstrated via comparisons with experimental results and finite element numerical method results. The proposed simple model was effective for predicting the conductor response and natural frequencies of the system (i.e., combined conductor and damper), but a poor predictor of the response of the counterweights.

The numerical simulations showed significant dependency of the natural frequencies on damper location and total mass. This was more pronounced when the damper was in the proximity of antinodes. With regard to the forced vibration, increasing the forcing frequency significantly reduced the vibration amplitude of the conductor. The use of two dampers was significantly superior to using a damper.

The second analytical model was based on double-beam concept. The main beam was subjected to an axial load and was representative of the conductor. The Stockbridge damper was modeled by an in-span beam with tip mass at each end. Explicit expression for the damping coefficient of the conductor was obtained through experiments in conjunction with the linear regression analysis. This model was validated using experimental data. Expressions were presented for the frequency equation, mode shapes, and orthogonality relations. Numerical examples on the free vibration analysis indicated that the mass of the counterweights, length of the rigid link, length of the messenger, and flexural rigidity had more effect on higher modes. The first mode was dominated by the conductor characteristics. The roles of the location of the Stockbridge damper on the system natural frequencies were inconclusive.

Parametric studies on the forced vibration analysis indicated that the response of the bare conductor decreases significantly with increasing frequency. However for a loaded conductor, the response can increase or decrease depending on the location of the dampers. It was also observed that the attachment of the Stockbridge damper significantly reduces the vibration response of the conductor. The degree of reduction was significantly dependent on the location and number of Stockbridge dampers.

Optimization was conducted to determine the optimal damping arrangement. It was demonstrated that optimal damping is achieved when two dampers are placed asymmetrically from the suspension clamps. That is, one damper should be placed at a distance between 50 to 70% of the loop length corresponding to the lowest wind speed (2 m/s) and another damper 85 to 95% of the loop length corresponding to the highest wind speed (7 m/s) and that the orientation of the bigger counterweight should be toward the span ends.

6.2 Contributions

The contributions of this thesis can be summarized in five major categories: modeling, equivalent mass-spring-damper system, conductor self-damping coefficient, asymmetric damping arrangement, orientation of the counterweight.

6.2.1 Modeling

Two novel mathematical models are presented for the vibration of a single conductor with Stockbridge dampers. Unlike the models in the literature, the proposed models accounted for the two-way coupling between the conductor and damper as well as crucial parameters such as the flexural rigidity of both the conductor and the damper, and mass of the damper. Expressions were presented for mode shapes, frequency equations, and generalized orthogonality relations. These expressions are of importance not only in the analysis of transmission lines vibration, but also in other fields of mechanical and structural engineering.

6.2.2 Equivalent mass-spring-damper

It was demonstrated that the Stockbridge damper can be reduced to an equivalent discrete spring-mass and viscous damping coefficient. This simplified representation of the Stockbridge was found to be good for a quick prediction of the response of the conductor. This finding can be very useful to a transmission design engineer in the analysis of transmission lines vibration.

6.2.3 Self-damping coefficient

Expressions for the self-damping power of the conductor abound in the literature because it is required in the energy balance principle. Other methods of analyzing vibration require the damping coefficient. As such, the determination of an explicit expression of the self-damping coefficient of the conductor is very crucial in the analysis of transmission line vibrations using analytical or the finite element method.

6.2.4 Asymmetric damping arrangement

The recommendation in the literature for best damping arrangement for suspension-spans is to symmetrically locate two dampers between 70 to 80% of the loop length corresponding to the highest wind speed. This approach is very efficient in the control of high frequencies excitation and the dampers are easy to install as the distance is usually within a meter from the tower. But it underperforms at low vibration frequencies. It was demonstrated in this thesis that the asymmetric damping arrangement is better at controlling both high and low vibration frequencies. Three scenarios of asymmetric damping arrangements were examined. The best was to install one damper between 50 to

70% of the loop length (corresponding to a wind speed of 2 m/s) and the other between 85 to 95% of the loop length (corresponding to a wind speed of 7 m/s).

6.2.5 Orientation of the counterweight

The proposed model (i.e., double-beam system) predicts the difference in the performance of the damper when the heavier counterweight is oriented toward the mid-span or span-end. Hitherto the decision for the orientation of the counterweights was arbitrary. In this work, it was shown that the orientation of the heavier counterweight toward the span-ends resulted in a better damping performance than an orientation toward the mid-span.

6.3 Future work

6.3.1 Stockbridge damper nonlinearity

It was assumed in this thesis that the Stockbridge damper experienced small vibration displacement and contact modeling was ignored. Hence the nonlinearity was not modeled. In reality, however, the Stockbridge damper may experience finite amplitude vibrations and relative motion between components. Therefore, it may be desirable to consider the geometric nonlinearity due to stretching of the messenger wire and internal contacts between the messenger and the counterweight.

6.3.2 Wind tunnel experiment

The wind force used in this work is approximated from the amount of power needed by the shaker to excite the conductor. A more accurate model would involve a wind tunnel experiment to determine an explicit expression for the wind force that will depend on the vibration frequency and the amplitude of the conductor.

6.3.3 Armor Rods

Armor rods is another type of damping device used to control aeolian vibration. Some power utilities employ a combination of both armor rods and Stockbridge damper to protect overhead transmission lines. However, the prediction of the performance of armor rods is currently based on experimental data. There is no analytical model of transmission line carrying armor rods. The current work did not consider armor rods. An extension of this work to include armor rods is worthy of consideration.

6.3.4 Dead-end spans

The present analytical model is only applicable to suspension-suspension spans. Dead-end towers are utilised when transmission lines change direction. These towers use horizontal insulators and can resist unbalance load due to conductor tension and weight. The span between dead-end towers is called dead-end spans. Hitherto there is no analytical model for dead-end span. The vibration protection for dead-end span is achieved by adding extra dampers. One major extension of this work will be to develop an analytical model for dead-end spans by including the coupling between insulators and conductor.

6.3.5 Bundle Conductor

High voltage transmission lines (greater than 230 kV) are usually transmitted through bundle conductors and spacer damper are employed to protect the lines from vibrations. The placement of the spacer dampers on the conductor is however based on rule of thumb. Therefore, it will be worthwhile to develop analytical models to predict the response of bundle conductors to determine optimal locations for the spacer dampers.

6.3.6 Galloping

Ice accretion on transmission lines in combination with heavy wind causes conductor galloping. Rigid and flexible interphase spacers have been used to control galloping. The established models on conductor galloping are mostly based on empirical data. There is no analytical model that takes into account the coupling between the conductor and interphase spacers. A development of such a model will be helpful for a more precise control of conductor galloping.

Bibliography

[1] EPRI. Transmission Line Reference Book, Wind Induced Conductor Motion, Palo Alto, California: Electrical Power Research institute, 2006.

[2] O. Barry. Finite Element Modeling of a Single Conductor with a Stockbridge Damper under Aeolian vibration, MASc Thesis, Ryerson University, Toronto, ON, 2010.

[3] D. Dempse and H. White. Winds Wreak Havoc on Lines, *Transmission and Distribution World*, 48(6), pp. 32-37, 1996.

[4] Helix. Montreal, Quebec, Canada, 2008.

[5] M.S. Dhotard, N. Ganesan and B.V.A. Rao. Transmission Line Vibration, Department of Applied Mechanics, India Institute of Technology, *Journal of Sound and Vibration*, 60(2), pp. 217-237, 1978.

[6] R. Claren and G. Diana. Mathematical Analysis of Transmission Line Vibration, Institute of Electrical and Electronics Engineers, *Transactions on Power Apparatus and Systems*, 60(2), pp. 1741-1771, 1969.

[7] Hydro One Inc. 2008. Toronto, Ontario.

[8] A. Leblond and C. Hardy. Assessment of Safe Design Tension with Regard to Aeolian Vibrations Of Single Overhead Conductors, *IEEE Transaction Power Delivery* 34C-TPC-14, 2000.

[9] D. Havard. Assessment of the Cowal JCT x Longwood TS for Vibration Control, Toronto, Ontario, 2008.

[10] D. Havard. Conductor Fatigue and Damper Damage on the Sarnia-Scott TS x Lucasville JCT, Toronto, Ontario, 2005.

[11] P. McCarthy and M. Melsness. Severe Weather Elements Associated With September 5, 1996 Hydro Tower Failures Near Grosse Isle, Manitoba, Canada, Manitoba Environment Service Center, *Environment Canada*, 48(6), pp. 21, 1996.

[12] CIGRE Meeting. Conductor Motion, Toronto, Ontario, 2009.

[13] N. Barbieri, O. Honorato de Souza and R. Barbieri. Dynamical Analysis of Transmission Lines Cables, Part1-Linear Theory, *Mechanical System and Signal Processing*, 18(3), pp. 659-669, 2004.

[14] C. Hardy and A. Leblond. Comparison of Conductor Self-Damping Measuremenis, CIGRE General Session, Paris.

[15] C.B. Rawlins. Wind Tunnel Measurement of The Power Imparted to a Model of a Vibrating Conductor, *Trans. IEEE Power Apparatus and Systems*, 102(4), pp. 963-971, 1983.

[16] M. Kraus and P. Hagedorn. Aeolian Vibration: Wind Energy Input Evaluated From Measurements on an Energized Transmission Lines, *IEEE transaction*, 6(3), pp. 1264-1270, 1991.

[17] D.U. Noiseux. Similarity Laws of The Internal Damping of Stranded cables in Transverse Vibrations, *IEEE T.D. Conference and Exposition*, Dallas, U.S.A., September, 1991.

[18] T. Seppa. Self-Damping Measurements And Energy Balance of ASCR Drake, *IEEE Winter Power Meeting*, Paper No.71 CP-161 PWR, New York, 1971.

[19] L. Mocks and J. Schmidt. Survey on Measurements of Mechanical Self-Damping of ACSR Conductor, CIGRE SC 2-89 (WG 11) TF1-2, 1989.

[20] H. Frahm. Device for Damping Vibrations of Bodies Patent No. 989,958, USA patent office, 1911.

[21] G.E. Braga, R. Nakamura and T.A Furtado. Aeolian Vibration of Overhead Transmission Line Cables: Endurance Limits, *IEEE Transmission and Distribution Conference*: Latin America, 2004.

[22] W.B. Buchanan and G.B. Tebo. Torsional Damper for Line Conductor Patent No. 2,215541, USA patent office, 1940.

[23] G. Stockbridge. Vibration Damper Patent No.1675391, USA Patent Office, 1925.

[24] M.L. Lu and J.K. Chan. An Efficient Algorithm for Aeolian Vibration of Single Conductor with Multiple Dampers, *Institute of Electrical and Electronics Engineers, Transactions on Power Delivery*, 22(3), pp. 1822-1829, 2007.

[25] S. Wiendl, P. Hagedorn and D. Hochlenert. Control of a test rig for vibration measurement of overhead transmission lines, Proc. 2009 *IEEE Conference on Control and Automation*, pp. 2129-2135, 2009.

[26] H. Wagner, V. Ramamurti, R. Sastry and K. Hartman. Dynamic of Stockbridge Dampers, *Journal of Sound and Vibration*, 30, pp. 207-220, 1973.

[27] D. Feldman. Aeolian Vibration: Possible Effects of Non Linear Behaviour of Stockbridge Dampers, Electricité de France, 2000.

[28] M. Markiewicz. Optimum Dynamic Characteristic of Stockbridge Dampers for Dead-End Spans, *Journal of Sound and Vibration*, 188(2), pp. 243-256, 1994.

[29] H.J. Krispin. Optimization of the Efficiency of Aeolian Vibration Dampers, *IEEE Power Africa Conference and Exposition Johannesburg*, South Africa, 2007.

[30] J. Vecchiarelli. Aeolian vibration of a conductor with a Stockbridge Type Damper, Ph.D. Thesis, University of Toronto, 1997.

[31] J. Vecchiarelli, I.G. Curries, and D.G. Havard. Computational Analysis of Aeolian Conductor Vibration with a Stockbridge-type Damper, *Journal of Fluid and Structures*, 14, pp. 489-509, 2000.

[32] O. Nigol and H.J. Houston. Aeolian Vibration of Single Conductor and Its Control, *IEEE Transactions on Power Apparatus and Systems*, 104(11), pp. 3245-3254, 1985.

[33] B. Shafer. Dynamic Modeling of Wind Induced Vibration of Over Head Lines, *Int. Non Linear Mechanics*, 19(5), pp. 455-467, 1984.

[34] G. Diana, M. Falco, A. Cigada and A. Manenti. On The Measurement of Over Head Transmission Lines Conductor Self-Damping, *IEEE Transactions on Power Apparatus and Systems*, 15(1), pp. 285-292, 2000.

[35] R. Bishop and A. Hassan. The Lift And Drag Forces On a Circular Cylinder Oscillating In a Flowing Fluid, Proceedings of Royal Society, London, Series A, 277(3), pp. 51-75, 1964.

[36] P.W. Bearman and I.G. Curie. Pressure-Fluctuation Measurements On An Oscillating Circular Cylinder, *Journal of Fluid Mechanics,* 91(4), pp. 661-677, 1979.

[37] O. Griffin and G. Koopmann. The vortex-excited lifts and reaction forces on resonantly vibrating cylinders, *Journal of Sound and Vibration*, 54(3), pp. 435-448, 1977.

[38] A. Oliveira and D.G. Preire. Dynamical Modeling and Analysis of Aeolian Vibration of Single Conductors, *IEEE Transaction Power Delivery*, 9(3), pp. 1685-1693, 1994.

[39] H. Verma and P. Hagerdorn. Wind Induced Vibration of Long Electrical Overhead Transmission Line Spans: A Modified Approach, *Journal of Wind and Structures*, 8(2), pp. 89-106, 2005.

[40] J.S. Tompkins, L.L. Merill and B.L. Jones. Quantitative Relationships in Conductor Vibration Using Rigid Models, *AIEE Transactions*, October 1956.

[41] C.B. Rawlins. Recent Developments in Conductor Vibration, Alcoa Technical Paper No. 13, 1958.

[42] O. Barry, D.C.D. Oguamanam and D.C. Lin. Free Vibration Analysis of a Single Conductor with a Stockbridge Damper, Proceedings of the 23rd CANCAM, June 5-9, Vancouver, British Columbia, Canada, 2011.

[43] O. Barry, D.C.D. Oguamanam and D.C. Lin. Aeolian vibration of a single conductor with a Stockbridge damper, *IMechE: Part C, Journal of Mechanical Engineering Science*, 227(5), pp. 935-945, 2013.

[44] O. Barry, J.W. Zu, and D.C.D Oguamanam. Forced Vibration Analysis of Transmission Lines: A Finite Element Approach, Proceedings of the 2012 CSME Conference, June 4-6, Winnipeg, Manitoba, Canada, 2012.

[45] IEEE Guide on the Measurement of the Performance of Aeolian Vibration Dampers for SingleConductors, IEEE Std. 664:1993.

[46] IEC Guide on the Requirements and tests for Stockbridge type aeolian vibration dampers, IEC Std. 61897:1998.

[47] D.G. Havard. Weakness in the Forced Response Method for Testing Vibration Dampers, *Institute of Electrical and Electronics Engineers*, Sanfransisco, 664, 1994.

[48] G. Diana, A. Cigada, M. Bellloli and M. Vanali. Stokbridge Type-Damper Effectiveness Evaluation: Part 1- Comparison Between Tests on Span and on the Shaker, *IEEE trans. Power Delivery*, 18, pp. 1462-1469, 2003.

[49] J.P. Bandstra. Comparison of Equivalent Viscous Damping and Nonlinear Damping in Discrete and Continuous System, *Journal of vibration, Acoustics, Stress, and Reliability in Design*, 105, pp. 382-392, 1983.

[50] P.A. Hassanpour, W.L. Cleghorn and E. Esmailzadeh. Exact Solution of the Oscillatory Behavior Under Axial Force of a Beam with Concentrated Mass Within its Interval, *Journal of Vibration and Control*, 13(12), pp. 1723-1739, 2007.

[51] Y. Chen. On the Vibration of a Beam or rods Carrying a Concentrated Mass, *Journal of Applied Mechanics*, 30(2), pp. 310-311, 1963.

[52] S. Naguleswaran. Transverse Vibration of an Euler-Bernouilli Uniform Beam Carrying two Particles In-span, *Journal of Mechanical Sciences*, 43, pp. 2737-2752, 2001.

[53] J.S Wu and T.L Lin. Free Vibration Analysis of a Uniform Cantilever Beam with Point Masses by an Analytical-and-Numerical-Combined Method, *Journal of Sound and Vibration*, 136, pp. 201-213, 1990.

[54] M. Gurgoze. On the Alternative Formulation of the Frequency Equation of Euler-Bernoulli Beam to which Several Spring-Mass Systems are attached In-Span, *Journal of Sound and Vibration*, 217(3), pp. 585-595, 1998.

[55] P.D. Cha. Natural Frequencies of a Linear Elastica Carrying any Number of Sprung Masses, *Journal of Sound and Vibration*, 247(1), pp. 185-194, 2001.

[56] H.Y. Lin and Y.C. Tsai. Free Vibration Analysis of a Uniform Multi-span Beam Carrying Multiple Mass Spring-mass Systems, *Journal of Sound and Vibration*, 302, pp. 442-456, 2007.

[57] O. Barry, J.W. Zu and D.C.D Oguamanam. Free Vibration Analysis of a Beam under Axial Load Carrying a Mass-Spring-Mass System, *Proceedings of the ASME 2012 International Design Engineering Technical Conferences and Computers and Information in Engineering Conference*, June 12-15, Chicago, Illinois, USA, 2012.

[58] O. Barry, J.W. Zu and D.C.D Oguamanam. Vibration Analysis of Stockbridge Dampers: Experimental Verification, *Proceedings of the 24th CANCAM Conference*, August 2-6, Saskatoon, Sk, Canada, 2013.

[59] M.N. Hamdan, and B.A Jubran. Free and Forced Vibrations of a Restrained Cantilever beam Carrying a Concentrated Mass, *Journal of Engineering Science*, 3, pp. 71-83, 1991.

[60] F.S. Samani and F. Pellicano. Vibration Reduction on Beams Subjected to a Moving Loads Using Linear and Nonlinear Dynamic Abosrbers, *Journal of Sound and Vibration*, 325, pp. 742-754, 2009.

[61] J.S. Wu and D.W. Chen. Dynamic Analysis of a Uniform CantileverBeam Carrying a Number of Elastically Mounted Point Masses with Dampers, *Journal of Sound and Vibration*, 229(3), pp. 549-578, 2000.

[62] J.S. Wu and C.G. Huang. Free and Forced Vibrations of a Timoshenko Beam with any Number of Translational and Rotational Springs and Lumped Masses, *Communications in Numerical Methods in Engineering*, 11, pp. 743-756, 1995.

[63] T.P. Chang and C.Y. Chang. Vibration Analysis of Beams with a two Degree-of-freedom Spring-mass System, *Journal of Solids Structures*, 35(5), pp. 383-401, 1998.

[64] K.H. Low. Comments on Vibrations of a Beam-mass System under Different Boundary Conditions (with authors' reply), *Journal of Sound and Vibration*, 207, pp. 284-287, 1997.

[65] C.L. Kirk and S.M. Wiedemann. Natural Frequencies and Mode Shapes of a Free-free Beam with Large end Masses, *Journal of Sound and Vibration*, 254, pp. 939-949, 2002.

[66] P.A. Hassanpour, E. Esmailzadeh and W.L. Cleghorn. Generalized Orthogonality Condition for Beams with Intermediate Lumped Masses Subjected to Axial Force, *Journal of Vibration and Control*, 16(5), pp. 665-683, 2010.

[67] P.A. Hassanpour. Design and Analysis of Micro-Electromechanical Resonant Structures, Ph.D. Thesis, University of Toronto, 2008.

[68] L. Ercoli and P.A.A. Laura. Analytical and Experimental Investigation on Continuous Beams Carrying Elastically Mounted Masses, *Journal of Sound and Vibration*, 114, pp. 519-533, 1987.

[69] W.H. Liu and C.C. Huang. Free Vibration of Restrained Beam Carrying Concentrated Masses, *Journal of Sound and Vibration*, 123, pp. 31-42, 1988.

[70] J.S. Wu and T.L. Lin. Free Vibration Analysis of a Uniform Cantilever Beam with Point Masses by an Analytical-and-Numerical-Combined Method, *Journal of Sound and Vibration*, 136, pp. 201-213, 1990.

[71] M. Gurgoze. On the Eigenfrequencies of a Cantilever Beam with Attached Tip Mass and Spring-Mass System, *Journal of Sound and Vibration* 190, pp. 149-162, 1996.

[72] A. Bokaian. Natural Frequencies of Beams Under Tensile Axial Loads, *Journal of Sound and Vibration*, 142(3), pp. 481-489, 1990.

[73] S. Woinowsky-Krieger. The Effect of an Axial Force on the Vibration of Hinged bars, *Transaction of the American Society of Mechanical Engineers, Journal of Applied Mechanics*, 17, pp. 35-36, 1950.

[74] W. Kwon and H. Bang. *The Finite Element Method Using MATLAB,* Boca Raton, FL: CRC Press, 1997.

[75] A.Y. Shehata, A.A. ElDamatty and E. Savory. Finite element modeling of transmission line under downburst wind loading, *Finite element Analysis and Design*, 42(1), pp. 71-89, 2005.

[76] O. Barry, D.C.D. Oguamanam and J.W. Zu. On the Dynamic Analysis of a Beam Carrying Multiple Mass-Spring-Mass-Damper System, *Shock and Vibration* 2014, Article ID 485630, 2014.

[77] O. Barry, D.C.D. Oguamanam and J.W. Zu. Nonlinear Vibration of an Axially loaded Beam Carrying Multiple Mass-Spring-Damper System, *Jouranl of Nonlinear Dynamics*, Accepted for Publication, 2014.

[78] D.J. Inman. *Engineering Vibration,* 2nd Ed. Prentice-Hall, N.J., 2001.

[79] H. Yamaguchi. Vibration of a Beam with an Absorber Consisting of a Viscoelastic Beam and a Spring-Viscous Damper, *Journal of Sound and Vibration*, 103(3), pp. 417-425, 1984.

[80] H.V. Vu, A.M. Ordonez and B.H. Karnopp. Vibration of a Double-Beam System, *Journal of Sound and Vibration*, 229(4), pp. 807-882, 2000.

[81] Z. Oniszczuk. Free Transverse Vibration of Elastically Connected Simply Supported Double-Beam Complex System, *Journal of Sound and Vibration*, 232, pp. 387-403, 2000.

[82] Z. Oniszczuk. Forced Vibration of a Elastically Connected Complex Simply Supported Double-Beam System, *Journal of Sound and Vibration*, 264, pp. 273-286, 2003.

[83] M. Abu-Hilal. Dynamic Response of a Double Euler-Bernoulli Beam due to a Moving Constant Load, *Journal of Sound and Vibration*, 297, pp. 477-491, 2006.

[84] A. Palmeri and S. Adhikari. A Galerkin-Type State-Space Approach for Transverse Vibrations of Slender Double-Beam systems with Viscoelastic Inner Layer, *Journal of Sound and Vibration*, 330, pp. 6372-6386, 2011.

[85] O. Barry, J.W. Zu and D.C.D Oguamanam. Free vibration Analysis of a Beam with an AttachedIn-span Beam withTip Mass, *Proceedings of the ASME 2013 Dynamic Systems and Control Conference*, October 21-23, Palo Alto, CA, USA, 2013.

[86] D.C.D. Oguamanam, J.S. Hansen and G.R. Heppler. Vibration of Arbitrarily Oriented Two-member Open Frames with Tip Mass, *Journal of Sound and Vibration*, 209(4), pp. 651-669, 1998.

[87] O. Barry, J.W. Zu and D.C.D. Oguamanam. Analytical and experimental investigation of overhead transmission line vibration, *Journal of Vibration and Control* DOI: 10.1177/1077546313517589, 2013.

[88] O. Barry, J.W. Zu and D.C.D. Oguamanam. Forced Vibration of Overhead Transmission Line: Analytical and Experimental Investigation, *Journal of Vibration and Acoustics*, Accepted for Publication, 2014.